Hydrodynamic Limits of Active Particle Systems with Mean-Field Interactions

from Rigorous Derivation to Kinesin-II Transport

Stan de Haas

BSc Thesis

Delft University of Technology

Program:
Applied Mathematics and Applied Physics

Supervisors:
Supervisor Applied Mathematics: Prof. dr. ir. F.H.J. Redig
Supervisor Applied Physics: Dr. T. Idema

Student number:
6051383

Date:
February 10, 2026

TU Delft

Abstract

Intracellular transport relies on the collective behavior of molecular motors, such as Kinesin-II, which must navigate crowded microtubule environments efficiently. While standard exclusion models like the Totally Asymmetric Simple Exclusion Process (TASEP) predict significant velocity reduction at high densities, Kinesin-II exhibits resilience to crowding, suggesting a mechanism of cooperative transport that remains poorly understood in both physical and mathematical theory.

This thesis addresses this gap by combining a rigorous mathematical derivation of hydrodynamic limits with a biologically motivated particle model. Mathematically, we derive the hydrodynamic limit for an active particle system where the active direction of the particles is governed by mean-field Curie-Weiss rates with parameter β for both local and global interactions. We prove that the microscopic stochastic dynamics converge to a macroscopic reaction-diffusion-advection PDE. Through linearization and Fourier-Laplace analysis, we derive analytical expressions for the velocity and diffusion coefficients, showing significant dependence on β.

Physically, we extend this framework to include exclusion and different interaction ranges σ. Our simulations reveal that exclusion introduces spatial correlation that breaks mean-field assumptions, leading to deviations from the predictions for the global transport coefficients. We show that for strong coupling $\beta > 1$, local interactions lead to the formation of clusters and altered relaxation times. Finally, we validate our model against experimental velocity-density data for Kinesin-II. We show that our mean-field exclusion model provides a statistically more accurate description compared to the standard TASEP-LK model.

Contents

1 Introduction

Active matter systems, ranging from flocking birds and schooling fish to intracellular motors and bacterial colonies, represent a fascinating frontier in modern non-equilibrium statistical physics. Unlike passive matter, which is driven solely by thermal fluctuations or external fields, active matter consists of self-propelled agents that consume energy to generate motion. A central challenge in this field is understanding how the microscopic stochastic rules governing individual particles, such as their self-propulsion, turning rates and interactions, give rise to coherent macroscopic phenomena like clustering and collective transport.

This thesis addresses this challenge at the intersection of probability theory and statistical physics. We focus on a specific class of active particles that possess an internal state and interact via a mean-field coupling [1–4]. This approach is chosen as it allows for a rigorous mathematical derivation of the hydrodynamic limit for such systems, and is applicable to solve a specific problem in intracellular transport: the collective motion of Kinesin-II molecular motors.

Intracellular transport is essential for cellular function, relying on molecular motors like kinesin to transport cargo along microtubule filaments [5, 6]. While the motion of single motors is well understood, the collective behavior of motors at high densities remains a subject of debate. Standard models, such as the Totally Asymmetric Simple Exclusion Process (TASEP), assume that motors interact solely through exclusion [7]. However,experimental data shows that these molecular motors form clusters and interact via more complex mechanisms [8, 9].

On the other hand, recent experimental data on Kinesin-II suggest that these motors are remarkably resilient to jamming, maintaining high velocities even in crowded environments [10]. This resilience hints at cooperative behavior or internal state regulation that simple exclusion models fail to capture. We expect that the motion of motors can be captured by the switching rates that depend on the collective state of their neighbors, a mechanism we model using Curie-Weiss Glauber dynamics [11]. By bridging this 'interaction gap', we aim to create a physically accurate particle model that outperforms standard TASEP-based models.

In order to use these biological models, we must understand their fundamental mathematical properties. How do we rigorously pass from the stochastic chaos of discrete particles to a deterministic continuum description?

This requires the derivation of the hydrodynamic limit. We consider a system of active and diffusive particles on a lattice whose switching rates depend on a global or local magnetization. Using techniques from the theory of interacting particle systems, such as Markov semigroups and generators, martingales and large deviation, we aim to prove that the empirical measure of the particle system converges to the solution of a partial differential equation (PDE) [2, 12, 13]. A key goal is to analytically derive the global transport coefficients, the effective velocity and effective diffusion coefficient, and understand how they are changed by cooperative interactions between particles. Additionally, we evaluate the stability of the homogeneous state and study the emergence of clustering.

For the physical part of this thesis, we aim to construct a particle-based model that explicitly incorporates biological constraints. Second, we aim to investigate how the range of interaction (controlled by the parameter σ) and the strength of the cooperation (controlled by β) influence the global transport coefficients and the formation of local structure. Finally, to validate the model we fit it over experimental density-velocity data for Kinesin-II, in order to improve the existing TASEP-LK models [10].

The remainder of this thesis is structured as follows. Section 2 provides the mathematical preliminaries, covering, for example, Martingales, the Curie-Weiss model and Brownian motion. In Section 3 we present the model that will be studied in this thesis and provide the proof of the

hydrodynamic limit, for both local and global interactions. Section 4 performs analysis on the derived PDE to obtain analytical expressions for the global transport coefficients. Next, Section 5 establishes the biological framework. Unlike a general introduction, this section specifically translates the biological properties of Kinesin-II into model constraints. In Section 6 we adapt the coarse-grained PDE model and its results to the specific biological constraints found in Section 5. Section 7 details the stochastic particle model and the Gillespie algorithm used for simulation. In Section 8 the results are presented. We validate the mathematical derivations and explore mean-field breaking phenomena. We conclude this section by fitting our model to experimental Kinesin-II data. Finally, our conclusions and directions for future research are given in Section 9.

2 Mathematical preliminaries

2.1 Markov processes

In the following section we will give some of the basic theory of continuous time Markov processes which will be needed to define active particle models. The theory presented in this section is derived from the following sources [2, 14, 15].

2.1.1 Markov property

Let $(\Omega, \mathscr{F}, \mathbb{P})$ denote a probability space. For a positive random variable $Y \in \Omega$ the following definition applies

Definition 2.1. A positive random variable Y has the *lack-of-memory property* if:

$$\mathbb{P}(Y > a + b | Y > a) = \mathbb{P}(Y > b) \text{ for } a, b \geq 0 \tag{2.1}$$

Intuitively this definition tells us Y is memoryless. Additionally, the random variable must be exponentially distributed, this follows from the following Proposition,

Proposition 2.1. *The continuous random variable Y has the lack-of-memory property if and only if Y is exponentially distributed.*

Proof. Here, only the converse is given. See *Griffiths and Welsh* [14] for the full proof. Let Y be exponentially distributed with parameter λ, then for $u, v \geq 0$,

$$\mathbb{P}(Y > u + v | Y > u) = \frac{\mathbb{P}(Y > u + v \cap Y > u)}{\mathbb{P}(Y > u)} = \frac{\mathbb{P}(Y > u + v)}{\mathbb{P}(Y > u)} = \frac{e^{-\lambda(u+v)}}{e^{-\lambda u}} = e^{-\lambda v} = \mathbb{P}(Y > v).$$

So that Y has the lack-of-memory property. □

The lack-of-memory property can be extended from a single random variable to a *stochastic process*, i.e., sequence of random variables. This property is then called the Markov property. Let $X = \{X_t, t \geq 0\}$ be a stochastic process on $(\Omega, \mathscr{F}, \mathbb{P})$. We define the *filtration* $\{\mathscr{F}_t, t \geq 0\}$ as $\mathscr{F}_t = \sigma(X_r \colon r \leq t)$. That is the σ-algebra generated by the random variables $X_r, r \leq t$. If the distribution of a future state only depends on the current state, we say the process is a Markov process. Mathematically this is expressed as follows.

Definition 2.2. A stochastic process X is called a *Markov process* if for all $f \colon \Omega \to \mathbb{R}$ bounded and measurable, and $0 < s \leq t$ the following holds,

$$\mathbb{E}[f(X_t) | \mathscr{F}_s] = \mathbb{E}[f(X_t) | X_s] \tag{2.2}$$

Furthermore, the Markov process is called *homogeneous* if for all $s > 0$ the process $\{X_{t+s}, t \geq 0\}$ starting from X_s has the same distribution as $\{X_t, t \geq 0\}$ starting from X_0 if $X_s = X_0$.

In the case of continuous Markov chains we cannot consider transition probabilities between different states in $\{X_t, t \geq 0\}$. Rather we have transition *rates* $c(x, y) \geq 0$, which can intuitively be seen as the transition probability per unit of time. For these rates we assume $c(x, y) \geq 0$ for all $x, y \in \Omega$ with total rate $c_x = \sum_{y \in \Omega} c(x, y) > 0$. From $X_t = x$ we must wait an exponential time with rate c_x before jumping to y with the probability defined by $p(x, y) := c(x, y)/c_x$. The requirement to wait an exponential time follows from the fact that it is the only distribution with the lack-of-memory property by Proposition 2.1.

2.1.2 Markov semigroup

When considering continuous time Markov processes $\{X_t, t \geq 0\}$ on the state space Ω an important concept is the Markov semigroup.

Definition 2.3. The *Markov semigroup* is a family of operators $\{S_t, t \geq 0\}$ acting on bounded functions $f\colon \Omega \to \mathbb{R}$ by the expected value of f at time t,

$$S_t f(x) = \mathbb{E}[f(X_t)|X_0 = x] \text{ for all } t \geq 0 \text{ and } x \in \Omega \tag{2.3}$$

As long as Ω is finite, the function f can be thought of as a column vector and thus S_t can be seen as a matrix with elements given by the transition probabilities, i.e., $(S_t)_{x,y} = \mathbb{E}(f(X_t)|X_0 = x) = \mathbb{P}(X_t = y|X_0 = x) = p_t(x, y)$. However, in a more general state space (i.e. $f \in C_b(\Omega)$) this interpretation does not hold. Therefore, it is better to see the semigroup S_t as an operator working on f. The semigroup has the following properties.

Proposition 2.2. *The semigroup S_t as defined by Definition 2.3 satisfies the following properties,*

(S_1) $S_0 f = f$,

(S_2) $S_{t+s} f = S_t(S_s f)$,

(S_3) $\lim_{t \downarrow 0} ||S_t f - f||_\infty = 0$,

(S_4) $S_t \mathbb{1} = \mathbb{1}$,

(S_5) *if* $f \geq 0$ *then* $S_t f \geq 0$,

(S_6) $||S_t f||_\infty \leq ||f||_\infty$

(S_2) *is called the semigroup property.* (S_3) *is called strong continuity, which states the semigroup is right-continuous at 0 with respect to the norm* $||f||_\infty = sup_{x \in \Omega}|f(x)|$. ($S_6$) *says that* S_t *is a contraction.*

By definition there exists a Markov semigroup $S_t, t \geq 0$ for every Markov process $X_t, t \geq 0$. However, this relation is also true in the other direction and is even one-to-one [1].

2.1.3 Markov generator

The semigroup property is analogous to the familiar laws of exponents: $e^{\lambda(t+s)} = e^{\lambda t} e^{\lambda s}$. This motivates the existence of a matrix L such that $S_t = e^{tL}$ on a finite state space. Here, the exponential is defined by its Taylor series,

$$e^{tL} = \sum_{n=0}^{\infty} \frac{t^n}{n!} L^n \tag{2.4}$$

This relation defines L via,

$$Lf := \frac{d}{dt} S_t f|_{t=0} = \lim_{t \to 0} \frac{S_t f - f}{t} \tag{2.5}$$

However, for a non-finite state spaces Ω the set for which $S_t = e^{tL}$ holds is restricted. That is, on an infinite state space certain operators, such as differential operators, are typically unbounded. This means the Taylor series may fail to converge. The Markov generator L should therefore not be seen as a matrix, but as an operator defined by Equation (2.5), and is known as the *infinitesimal or Markov generator* for a Markov process with semigroup $\{S_t, t \geq 0\}$. It shows the behavior for an infinitesimal time interval, well-defined on the domain,

$$D(L) := \left\{ f : \lim_{t \to 0} \frac{S_t f - f}{t} \text{ exists} \right\} \tag{2.6}$$

There exists an one-to-one correspondence between the Markov generator and Markov semigroup, similar to the fact that the relation between the semigroup and its Markov process is one-to-one [2].

Proposition 2.3. *There is an one-to-one correspondence between the Markov generator L and the Markov semigroup $\{S_t, t \geq 0\}$ on the domain $D(L)$ defined in Equation (2.6) if*

(i) The generator is given by

$$Lf = \lim_{t \to 0} \frac{S_t f - f}{t}$$

(ii) The semigroup is given by

$$S_t = \lim_{n \to \infty} \left(I - \frac{t}{n} L \right)^{-n}$$

(iii) For $f \in D(L)$ we have that $S_t f \in D(L)$ and

$$\frac{d}{dt} S_t f = S_t L f = L S_t f$$

We have now discussed the Markov process, semigroup and generator. Their correspondence can be summarized in the following figure, based on *van Wiechen* [16].

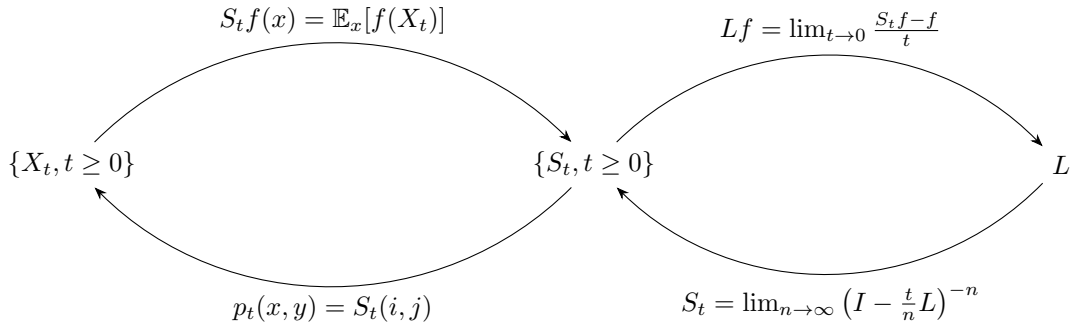

Figure 2.1: Overview of the one-to-one relations between the Markov process, semigroup and generator

Earlier we introduced that transition rates must have exponential waiting times. We can now extend this example and define its semigroup and generator.

Example 2.1. For the continuous random walk we defined transition rates $c(x, y) \geq 0$ with total rate $c_x = \sum_{y \in \Omega} c(x, y) > 0$ where the probability is defined by $p(x, y) := c(x, y)/c_x$. By Proposition 2.1, for any point in time t where $X_t = x$, we must wait an exponential time before jumping to another point. This exponential time is distributed by $\exp(c_x)$. We can use this to compute the generator. Let K_t be the total number of jumps within the interval $[0, t]$. By the law of total expectation, we have that for any $x \in \Omega$,

$$\begin{aligned}
S_t f(x) - f(x) = \mathbb{E}_x(f(X_t)) &= \sum_{k=0}^{\infty} [\mathbb{E}(f(X_t) \cap K_t = k)] - f(x) \\
&= \mathbb{E}_x(f(X_t) \cap K_t = 0) + \mathbb{E}_x(f(X_t) \cap K_t = 1) - f(x) + \mathcal{O}(t^2) \\
&= f(x) \mathbb{P}_x(K_t = 0) + \sum_{y \in \Omega} [f(y) \mathbb{P}_x(K_t = 1) p(x, y)] + \mathcal{O}(t^2) \\
&= f(x) e^{-c_x t} + \sum_{y \in \Omega} \left[f(y)(1 - e^{-c_x t}) \frac{c(x, y)}{c_x} \right] - f(x) + \mathcal{O}(t^2) \\
&= (1 - e^{-c_x t}) \sum_{y \in \Omega} \left[\frac{c(x, y)}{c_x} (f(y) - f(x)) \right] + \mathcal{O}(t^2)
\end{aligned}$$

Here $\mathcal{O}$ is Landau's notation, and represents functions that have a smaller order of magnitude than t^2 as $t \to 0$. So $h(t) = \mathcal{O}\left(t^2\right)$ when $h(t)/t^2 \to 0$ as $t \to 0$. For $t \to 0$ we use $(1 - e^{-c_x t}) \to c_x t$

and therefore,

$$Lf = \lim_{t\to 0} \frac{S_t f - f}{t} = \sum_{y\in\Omega} [c(x,y)(f(y) - f(x))] + \mathcal{O}(t)$$

So as $t \to 0$, we conclude that the generator for a continuous random walk is given by,

$$Lf = \sum_{y\in\Omega} [c(x,y)(f(y) - f(x))] \tag{2.7}$$

2.1.4 Stationary distributions

Before ending this section on Markov processes, we end with an important property of Markov processes, namely *stationary distributions*, which will be needed in proofs in later sections. Consider a Markov process $\{X_t, t \geq 0\}$ with semigroup S_t on state space Ω with some probability distribution μ where $\mu_t = \mu S_t$.

Definition 2.4. The probability distribution μ_t is called a *stationary distribution* if for all $t \geq 0$, $\mu_t = \mu$. That is,

$$\langle S_t f, \mu\rangle = \langle f, \mu\rangle \tag{2.8}$$

where $\langle f, \mu\rangle = \int f d\mu$ or in the finite state space $\langle f, \mu\rangle = \sum_i f_i \mu_i$. This is equivalent to

$$\langle Lf, \mu\rangle = 0 \tag{2.9}$$

Example 2.2. Reconsider the generator found for the continuous time random walk in Example 2.1. Using Definition 2.4 we see that μ is a stationary distribution for this problem if,

$$\sum_{y\in\Omega} [\mu(x)c(x,y) - \mu(y)c(y,x)] = 0$$

A stronger requirement can be found which requires all the terms in the sum to be equal to zero. This is known as the *detailed balance condition* and can be used to find or check stationary distributions,

$$\mu(x)c(x,y) - \mu(y)c(y,x) = 0 \qquad \text{for all } x, y \in \Omega \tag{2.10}$$

2.2 Elements of large deviation theory

In this section we present some of the basic definitions and theorems of large deviation theory. Large deviation theory provides a mathematical framework for quantifying the probabilities of rare events in high-dimensional stochastic systems. The key objects in this theory are *rate functions*, which quantify the exponential decay of probabilities of atypical states, and *variational principles*, which allow one to evaluate asymptotic partition functions. In this section these will be introduced to derive the mean-field Glauber dynamics following from the Curie-Weiss model in Section 2.3. The section is based on the following sources [11, 13, 17–20].

2.2.1 Rate functions and the large deviation principle

We begin by defining the class of functions that quantify the exponential decay of probabilities in the large-system limit.

Definition 2.5. Let X be a topological space such that both open and closed subsets are well-defined. Then I is a well-defined rate function if,

(*i*) I is lower semi-continuous (i.e. $f : X \to [0,1]$ if $\lim_{N\to\infty} \inf f(x_N) \geq f(x) \quad \forall x_N, x \in X \ni x_N \to x$).

(*ii*) The level sets $\psi_I(\alpha) = \{x : I(x) \leq \alpha\}$ of I are compact.

A rate function that satisfies (ii) is often called a *good* rate function.

Given a rate function, we define an exponential principle describing the asymptotic decay of probabilities: the *large deviation principle* (LDP).

Definition 2.6. A family of probability measures $\{\mu_N\}_{N\geq 0}$ satisfies the *large deviation principle* with rate N and rate function $I(x)$ if,

(*i*) $I(x)$ is well-defined good rate function.

(*ii*) $\lim_{N\to\infty} \sup_{x\in C} \frac{1}{N} \log \mu_N(C) \leq -\inf_{x\in C} I(x) \quad \forall C \subseteq X, C$ is closed.

(*iii*) $\lim_{N\to\infty} \inf_{x\in O} \frac{1}{N} \log \mu_N(O) \geq -\inf_{x\in O} I(x) \quad \forall O \subseteq X, O$ is open.

Intuitively, the LDP states that μ_N assigns mass asymptotically proportional to $\mu_N(m) \approx e^{-NI(m)}$ up to subexponential corrections.

2.2.2 The log-moment generating function and the Gärtner-Ellis theorem

A key mechanism for obtaining rate functions is the Gärtner-Ellis theorem. This is a powerful result which establishes the existence of a large deviation principle for processes where the cumulant generating functions tend towards a well-behaved limit. Before introducing this theorem, we must define the log-moment generating function of a sequence of random variables $\{m_N\}_{N\geq 0}$,

$$F(\lambda) := \lim_{N\to\infty} \log\left(\mathbb{E}\left[e^{\lambda m_N(\sigma)}\right]\right) \tag{2.11}$$

defined whenever this limit exists as a finite function on some interval containing $\lambda = 0$. The corresponding rate function is defined by the Legendre-Fenchel transform.

Definition 2.7. For any function $F : \mathbb{R} \to \mathbb{R}$, the *Legendre-Fenchel transform* of F is the function $I^* : \mathbb{R} \to \mathbb{R} \cup \{\infty\}$ defined by

$$I^*(m) = \sup_{\lambda\in\mathbb{R}} [m\lambda - F(\lambda)] \tag{2.12}$$

In large deviation theory, the function I^* is the natural candidate for the rate function.

Under standard differentiability assumptions on F, this function $I^*(m)$ is indeed the LDP rate function for the sequence $\{m_N\}_{N\geq 0}$. While the Gärtner-Ellis theorem provides the general framework for dependent sequences, a more fundamental result applies when the variables are independent and identically distributed (i.i.d.).

Theorem 2.4 (Cramér's theorem)**.** *Let $\{m_N\}_{N\geq 0}$ be a sequence of real-valued i.i.d. random variables. Assume that the log-moment generating function*

$$\Lambda(\lambda) := \log\left(\mathbb{E}\left[e^{\lambda X_1}\right]\right)$$

exists as a finite function for all λ and the sample mean is given by,

$$m_N := \frac{1}{N}\sum_{i=1}^{N} X_i$$

Then the sequence $\{m_N\}_{N\geq 1}$ satisfies the large deviation principle with speed N and good, convex rate function $I(m)$ equal to the Legendre-Fenchel transform of $\Lambda(\lambda)$,

$$I(m) = \sup_{\lambda\in\mathbb{R}} \left[m\lambda - \Lambda(\lambda)\right]$$

A consequence of the LDP, given in the following theorem, is the asymptotic evaluation of probability tails, which shows that probabilities of deviations of order $\mathcal{O}(N)$ decay exponentially at rate $I(m)$.

Theorem 2.5. *if $\{m_N\}_{N\geq 0}$ satisfies the LDP with rate function I, then, for $m \in \mathbb{R}$,*

$$\lim_{N\to\infty}\left(\frac{1}{N}\log\left(\mathbb{P}(Nm_N(\sigma)) \geq Nm\right)\right) = -I(x) \tag{2.13}$$

2.2.3 Varadhan's Lemma

The most important tool in large deviation theory, especially when combined with statistical mechanics, is Varadhan's lemma. This lemma allows us to compute exponential integrals of the form that appear in partition functions.

Lemma 2.6 (Varadhan's lemma)**.** *Let $\{\mu_N\}_{N\geq 0}$ satisfy the LDP on $\mathbb{R}$ with rate N and with rate function $I(m)$. Let $F : \mathbb{R} \to \mathbb{R}$ be a continuous function that is bounded from above, then*

$$\lim_{N\to\infty}\frac{1}{N}\log\left(\mathbb{E}_{\mu_N}\left[e^{NF(m_N(\sigma))}\right]\right) = \sup_{m\in\mathbb{R}}\left(F(m) - I(m)\right) \tag{2.14}$$

In physical terms, Varadhan's lemma converts an exponential sum into a variational problem where the dominating contribution comes from the maximizer of $F(m) - I(m)$. This principle will play a central role when deriving the mean-field switching Glauber dynamics of the Curie-Weiss model in the following section.

2.3 Mean-field Glauber dynamics and the Curie-Weiss model

In this section we expand the rates $c(x, y)$ to rates that depend on states of other particles in the system equally, the *mean-field approximation*. This is done because mean-field switching rates are relevant in the field of active particle models since they allow us to capture collective behavior while reducing dimensions. One of the models that follows this mean-field approximation is the Curie-Weiss model. Here each particle interacts with all other particles equally, and the relative positions of all other particles can therefore be neglected. This model, originally intended for modeling spin in ferromagnetism, has wide applications such as neural networks and superconductivity and many other stochastic processes. For us, it provides a natural framework to introduce mean-field switching rates and will later be connected to the hydrodynamic limit of interacting particle systems in Section 3. This section is based on the following source [11]. Before starting to study properties of systems with mean-field interactions, it is natural to introduce the canonical Gibbs distribution, since it allows us to capture the collective behavior of the system in a statistical framework.

Definition 2.8. The *canonical Gibbs distribution* with parameter β associated with a system of N systems is the probability distribution on Ω_N defined by,

$$\mu_{N;\beta}(\omega) := \frac{e^{-\beta \mathscr{H}(\omega)}}{\mathbf{Z}_{\beta,N}}$$

Where the normalizing sum is the *canonical partition function* defined as,

$$\mathbf{Z}_{N;\beta} := \sum_{\omega \in \Omega_N} e^{-\beta \mathscr{H}(\omega)}$$

We will now introduce the Curie-Weiss model. This spin-model, with $\omega_i \in \{-1, 1\}$, has three important properties which will be used in the definition of the *Curie-Weiss Hamiltonian*.

(*i*) The interactions are global, i.e., each spin interacts with all other spins, and all interactions are identical. Because of this lack of geometry, this model can be seen as a *complete graph* with an edge between all spins.

(*ii*) The interactions favor agreement of spin values, i.e., for two interacting spins ω_i and ω_j their interaction contributes an energy $-\omega_i\omega_j$ to the total energy. So aligned pairs have a lower energy.

(*iii*) The spins align with the external magnetic field, i.e., for a constant external magnetic field h, a spin ω_i interacting with it contributes an energy $-h\omega_i$. So aligned spins have a smaller energy.

Definition 2.9. The *Curie-Weiss Hamiltonian* for a collection of spins $w = (w_1, ..., w_N)$ with inverse temperature β and external magnetic field h is defined by:

$$\mathscr{H}_{N;\beta,h}(\omega) := -\frac{\beta}{2N} \sum_{i,j=1}^{N} \omega_i\omega_j - h \sum_{i=1}^{N} \omega_i$$

Note 2.1. The external magnetic field h is not used in the active particle models that will be introduced later. Therefore, the external magnetic field h will be set to zero to simplify computations. This gives us the advantage that the model is invariant under a total spin flip $\omega \mapsto -\omega$.

2.3.1 Behavior for large N

To study the behavior of the field we introduce the *(magnetic) density*,

$$m_N := \frac{1}{N} \sum_{i=1}^{N} \omega_i \tag{2.15}$$

We expect that the spins should be approximately independent for small β. However, when β is large, the density in this model concentrates at one of the two ground states equally. This behavior is summarized in the following theorem,

Theorem 2.7. *Define $\beta_c = 1$ as the inverse Curie temperature. Then the following holds,*

(*i*) *When $\beta \leq \beta_c$ the magnetization concentrates at zero. That is,*

$$\forall \beta \leq \beta_c, \quad m_N \simeq 0 \qquad \text{with probability close to } 1$$

(*ii*) *When $\beta \geq \beta_c$ the magnetization is bounded away from zero. More precisely, the magnetization concentrates at the spontaneous magnetization $\pm m^*(\beta)$ equally. That is,*

$$\forall \beta \geq \beta_c, \quad m_N \simeq \begin{cases} +m^*(\beta) & \text{with probability close to } \frac{1}{2}, \\ -m^*(\beta) & \text{with probability close to } \frac{1}{2}. \end{cases}$$

This behavior is summarized in Figure 2.2 which plots the distribution of m_N for $\beta \leq \beta_c$ (left) and $\beta \geq \beta_c$ (right) [11].

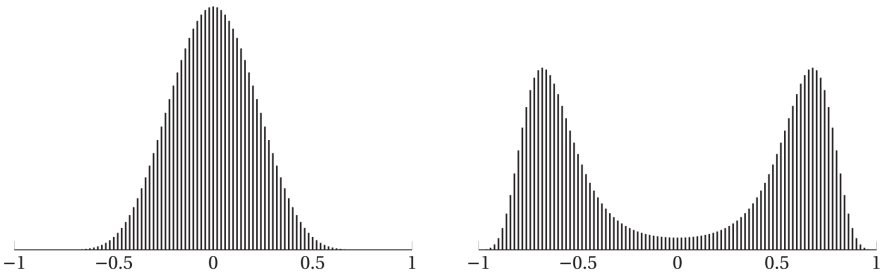

Figure 2.2: The distribution of the magnetization of the Curie-Weiss model, $\mu(m_N = \cdot)$ with $N = 100$ spins. Plot adapted from [11].

To prove this theorem we make use of the large deviation principle presented in Section 2.2. That is, we find its associated rate function.

Theorem 2.8. *Let $e(m) := -dm^2$ and $s(m) := -\left(\frac{1-m}{2}\log\left(\frac{1-m}{2}\right) - \frac{1+m}{2}\log\left(\frac{1+m}{2}\right)\right)$. Then the* free energy *$I(m)$ of the Curie-Weiss model is given by,*

$$I(m) := \beta e(m) - s(m) \tag{2.16}$$

Proof. To prove this statement we make use Cramér's theorem and Varadhan's lemma presented in Section 2.2. Cramér's theorem will allow us to show $I(m) = -s(m)$ as it treats all the particles to be i.i.d. Varadhan's lemma is used to show that the remaining term $\beta e(m)$ is part of the rate function. We start of by assuming are particles are i.i.d. and use Cramer's theorem. Let $X_i = \sigma_i$, then,

$$\mathbb{E}\left[e^{\lambda X_1}\right] = \frac{e^{\lambda} + e^{-\lambda}}{2}$$

Then the log-moment generating function is defined as

$$\Lambda(\lambda) := \log \mathbb{E}\left[e^{\lambda X_1}\right] = \log\left(\frac{e^{\lambda} + e^{-\lambda}}{2}\right)$$

Now Cramér's theorem applies to $m_N = \frac{1}{N}\sum_{i=1}^{N} X_i$. That is, m_N satisfies an LDP with speed N and a good rate function $I_0(m)$ given by the Legendre-Fenchel transform of $\Lambda(\lambda)$,

$$I_0(m) = \sup_{\lambda \in \mathbb{R}} \left(\lambda m - \log\left(\frac{e^{\lambda} + e^{-\lambda}}{2}\right)\right) \tag{2.17}$$

To find the supremum of $I_0(m)$ we must solve $dI_0(m)/dm = 0$ this gives

$$m = \frac{e^{\lambda} - e^{-\lambda}}{e^{\lambda} + e^{-\lambda}}$$

Substituting m into Equation (2.17) results in

$$I_0(m) = \frac{1-m}{2}\log\left(\frac{1-m}{2}\right) - \frac{1+m}{2}\log\left(\frac{1+m}{2}\right) = -s(m) \tag{2.18}$$

As the particles were assumed to be i.i.d. the interaction term $\beta e(m)$ is missing. We use Varadhan's lemma to find this interaction term. As the Hamiltonian of the Curie-Weiss model for $h = 0$ can be rewritten as $\mathscr{H}_{N;\beta,0}(\omega) = -\beta m_N^2 N/2$ using

$$\sum_{i,j=1}^{N} \omega_i\omega_j = \left(\sum_{i=1}^{N}\omega_i\right)^2 = (m_N N)^2,$$

we take $F(m) = \beta m^2/2$. Therefore, the Gibbs measure,

$$\tilde{\mu}_N(A) = \frac{\mu_N\left(e^{NF(m_N(\sigma))}\cdot \mathbb{1}_A\right)}{\mu_N\left(e^{NF(m_N(\sigma))}\right)} = \frac{\int_{m_N\in A} e^{NF(m_N(\sigma))}d\mu_N}{\int e^{NF(m_N(\sigma))}d\mu_N} \tag{2.19}$$

This can be rewritten as,

$$\frac{d\tilde{\mu}_{N,\beta}}{d\mu_N} = \frac{e^{NF(m_N(\sigma))}}{Z_N(\beta)}$$

with $Z_N(\beta)$ defined as the partition function, i.e., $Z_N(\beta) = \int e^{NF(m_N(\sigma)}d\mu_N$. Now we apply Varadhan's lemma to $F(m)$ to find

$$\lim_{N\to\infty}\frac{1}{N}\log\left(\mathbb{E}_{\mu_N}\left[e^{NF(m_N(\sigma))}\right]\right) = \sup_{m\in[-1,1]}(F(m) - I_0(m))$$

where $\mathbb{E}_{\mu_N}\left[e^{NF(m_N(\sigma))}\right] = \int e^{NF(m_N(\sigma)}d\mu_N$. To find $I(m)$ we apply Varadhan's lemma to both the numerator and the denominator of Equation (2.19). To simplify further notation define $\psi(\beta)$ to be given by,

$$\psi(\beta) := \lim_{N\to\infty}\frac{1}{N}\log Z_N(\beta) = \sup_{m\in[-1,1]}(F(m) - I_0(m))$$

Applying Varadhan's lemma to Equation (2.19) gives

$$I(m) = I_0(m) - F(m) - \inf_{m\in[-1,-1]}(I_0(m) - F(m)) = I_0(m) - F(m) + \psi(\beta)$$

As $\psi(\beta)$ is a constant is not important in large deviation theory and my therefore be dropped giving us the final rate function

$$I(m) = \beta e(m) - s(m)$$

□

So the rate function is of the form $I(m) = \beta e(m) - s(m)$. Finding the maxima of $\mu_{N;\beta}$ comes down to finding the maxima of $I(m)$, which is done by solving $\frac{dI(m)}{dm} = 0$. This gives,

$$m = tanh(\beta m) \tag{2.20}$$

This function is the known as the *mean-field equation* and will be seem repeatedly during the course of this thesis. Plotting the function, as done in Figure 2.3.1, shows that this function satisfies Theorem 2.7. Therefore by proving the system has the rate function $I(m)$ in Theorem 2.8 we have immediately proven Theorem 2.7.

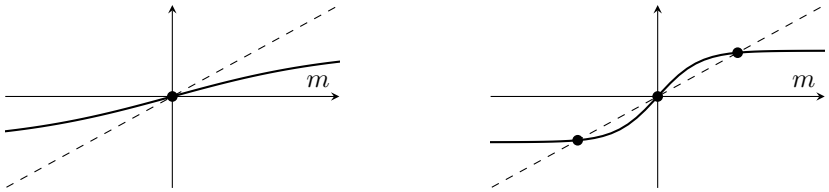

Figure 2.3: Two plots of Equation (2.20) where on the left, $\beta \leq \beta_c$, and the right $\beta \geq \beta_c$. These plots show respectively $\beta = 0.5$ and $\beta = 2$.

2.3.2 Mean-field switching rate for the Curie-Weiss model

This section couples the Curie-Weiss model with active particle systems, and thereby with Markov processes seen in Section 2.1. This is done by giving the mean-field switching rate associated with the Curie-Weiss model and proving that this rate satisfies both the mean-field Equation (2.20) and the detailed balance condition (Equation (2.10)).

Theorem 2.9. *Let $\{\sigma_t\}_{t\geq 0}$ a Markov process where $\sigma_i \in \{-1, 1\}$ and $m_N := \frac{1}{N}\sum_{j=1}^{N}\sigma_j$. Then, the Curie-Weiss Glauber rates defined by,*

$$c(\sigma, m_N(\sigma)) = e^{-\sigma\beta m_N} \tag{2.21}$$

are rates that satisfy both the mean-field Equation (2.20) *and the detailed balance equation as $N \to \infty$ where $\mu = \mu_{N;\beta}$ is defined as the canonical Gibbs distribution with the Curie-Weiss Hamiltonian, i.e.,*

$$\mu_{N;\beta}(\sigma^i)c(\sigma_i, m_N(\sigma^i)) = \mu_{N;\beta}(\sigma)c(\sigma, m_N(\sigma))$$

Proof. Below a sketch of the proof is provided. We start by showing that $c(\sigma, m_N(\sigma))$ satisfies the detailed balance equation together with $\mu_{N;\beta}$. First of all, note that if we start with a configuration of total spin S and switch the sign of σ_i to get the configuration σ^i with total spin S'. Then the spin difference between these two configurations is $-2\sigma_i$. For the magnetization we have,

$$m_N = \frac{S}{N} \qquad \text{and} \qquad m_N^i = \frac{S'}{N} = \frac{S - 2\sigma_i}{N}$$

Using the Hamilton, we then get,

$$\frac{\mu_{N;\beta}(\sigma^i)}{\mu_{N;\beta}(\sigma)} = e^{\mathscr{H}_{N;\beta,0}(\sigma^i) - \mathscr{H}_{N;\beta,0}(\sigma)} = e^{\frac{-\beta}{2N}\left((S-2\sigma_i)^2 - S^2\right)} = e^{\frac{-\beta}{N}(-2\sigma_i S + 2)} = e^{-\beta\left(-2\sigma_i m_N + \frac{2}{N}\right)}$$

Since N is very large (i.e. we let $N \to \infty$) we have $\frac{\mu_{N;\beta}(\sigma^i)}{\mu_{N;\beta}(\sigma)} = e^{2\sigma_i m_N}$. By definition of $c(\sigma, m_N(\sigma))$ we find $\frac{c(\sigma, m_N(\sigma))}{c(\sigma_i, m_N(\sigma^i))} = e^{2\sigma_i\beta m_N}$. Therefore it satisfies the detailed balance equation since,

$$\frac{\mu_{N;\beta}(\sigma^i)}{\mu_{N;\beta}(\sigma)} = e^{2\sigma_i\beta m} = \frac{c(\sigma, m_N(\sigma))}{c(\sigma_i, m_N(\sigma^i))}$$

We will now show that $c(\sigma, m_N(\sigma))$ satisfies the mean-field Equation (2.20). First, remember that the generator for the continuous random walk, given in Example 2.1 applied here and is of the form,

$$Lm_N(\sigma) = \sum_{i=1}^{N} c(\sigma_i, m_N(\sigma^i))\left(m_N(\sigma^i) - m_N(\sigma)\right)$$

To simplify calculations, we normalize $c(\sigma, m_N(\sigma))$,

$$c'(\sigma, m_N(\sigma)) = \frac{c(\sigma, m_N(\sigma))}{\sum_{\sigma\in\{-1,1\}} c(\sigma, m_N(\sigma))} = \frac{e^{-\sigma\beta m_N}}{e^{-\beta m_N} + e^{\beta m_N}} = \frac{1}{2}\left(1 - \sigma\tanh(\beta m_N)\right)$$

This allows us to write the generator as follows,

$$\begin{aligned} Lm_N(\sigma) &= \sum_{i=1}^{N} c'(\sigma_i, m_N)\left(m_N(\sigma^i) - m_N(\sigma)\right) = \sum_{i=1}^{N} c'(\sigma_i, m_N)\left(-\frac{2\sigma_i}{N}\right) \\ &= -\frac{2}{N}\sum_{i=1}^{N}\frac{1}{2}(1-\sigma_i\tanh(\beta m_N))\sigma_i \overset{\sigma_i^2=1}{=\!=\!=} -\frac{1}{N}\sum_{i=1}^{N}(\sigma_i - \tanh(\beta m_N)) \\ &= -\frac{1}{N}\sum_{i=1}^{N}(\sigma_i) + \tanh(\beta m_N) = -m_N(\sigma) + \tanh(\beta m_N(\sigma)) \end{aligned}$$

Consider $m_N(t) = m_N(\sigma_t)$. Using basic techniques for taking the hydrodynamic limit (see Section 2.4) such as Dynkin's formula for Markov processes, we find that as $N \to \infty$, fluctuations vanish and $m_N(t)$ converges in probability to the deterministic trajectory given by,

$$\dot{m}(t) = -m(t) + \tanh(\beta m(t)) \qquad \text{with } m(0) = \lim_{N\to\infty} m_N(0) \tag{2.22}$$

in equilibrium (i.e. as $t \to \infty$) this gives us the mean-field Equation (2.20). □

2.4 Density profiles and the microscopic stochastic limit

In this section we focus on the question of how microscopic stochastic dynamics of particles in Ω produces macroscopic deterministic behavior in $\mathbb{R}$. Something that is important as it allows us to bridge the gap from random non-deterministic configurations in the micro world to deterministic profiles in the macro world. Like the *law of large numbers* that averages out when we zoom out to large scales, we introduce *density profiles* which allows for static scaling in space and later the *hydrodynamic limit* which also allows for time rescaling. We will see that this transition can in certain cases be non-trivial i.e., different processes in Ω can yield the same result on $\mathbb{R}$. However, it does allow us to prove that basic particle configurations follow partial differential equations; and can thus link microscopic systems with important laws of physics, such as the diffusion equation or the heat flow equation. This section is based on the following pieces of literature [2, 12, 16, 21].

2.4.1 Density profiles

For this section we look at particle configurations on $V := X_N \times S$, where $S \subset \mathbb{Z}$ is finite and the particles are indistinguishable. Here X_N can either be an infinite domain $\mathbb{Z}$ or a periodic torus $\mathbb{T}_N$ In this case $(x, \sigma) \in V$ represents a particle with position $x \in X_N$ and internal state $\sigma \in S$. We can now define $\Omega := \mathbb{N}_0^V$ and an initial distribution with $\eta(x) \in \Omega$ as the number of particles at site x.

To go from the micro- to macroscopic world we introduce the scaling parameter $N \in \mathbb{N}$. This parameter lets a macroscopic point $x \in \mathbb{R}$ correspond to a micro-point $\lfloor xN \rfloor \in X_N$. Formally that is,

Definition 2.10. For $\{\eta^N : N \in \mathbb{N}\}$ a sequence of configurations in Ω, we call a sequence of measures $\{\pi^N : N \in \mathbb{N}\}$ on $\frac{1}{N}\mathbb{Z}$ the *empirical measure* if

$$\pi^N := \frac{1}{N} \sum_{(x,\sigma)\in V} \eta^N(x, \sigma)\delta_{(\frac{x}{N},\sigma)}$$

Note that π^N is still a microscopic measure. However, if we let $N \to \infty$ this measure will converge to some measure in $\mathbb{R}$. This measure has the form $\rho(x)dx$ with $\rho : \mathbb{R} \times S \to \mathbb{R}_{\geq 0}$, where the function ρ is called the *(macroscopic) density profile*. Formally the convergence of these measures is defined as the following,

Definition 2.11. Let $\rho : V \to \mathbb{R}_{\geq 0}$ be a density profile,

(*i*) A sequence of configurations $\{\eta^N, N \in \mathbb{N}\}$ *corresponds* to ρ if for all smooth test functions $\phi \in C^\infty_{c,S}(\mathbb{R})$,

$$\int \phi(x, \sigma)d\pi^N(x, \sigma) \to \int \phi(x, \sigma)\rho(x, \sigma)dx, \qquad \text{as } N \to \infty$$

(*ii*) A sequence of probability measures $\{\nu^N, N \in \mathbb{N}\}$ *corresponds* to ρ if for the sequence of stochastic variables $\{\eta^N, N \in \mathbb{N}\}$, where $\eta^N \sim \nu^N$ for every N, and for all smooth test functions $\phi \in C^\infty_{c,S}(\mathbb{R})$,

$$\int \phi(x, \sigma)d\pi^N(x) \xrightarrow{\mathbb{P}} \int \phi(x, \sigma)\rho(x, \sigma)dx, \qquad \text{as } N \to \infty$$

where $C^\infty_{c,S} = \{\phi : \mathbb{R} \times S \to \mathbb{R}, \text{ where } \phi \text{ smooth and compact}\}$ on the infinite domain $\mathbb{Z}$ and $C^\infty_{c,S} = \{\phi : \mathbb{R} \times S \to \mathbb{R}, \text{ where } \phi \text{ smooth and periodic}\}$ on the periodic domain $\mathbb{T}_N$.

2.4.2 Hydrodynamic limit

To link our particle configurations to partial differential equations we do not only require a scaling in space, but also in time. We want to see how the density profile changes as the microscopic configuration $\{\eta_t, t \geq 0\}$ changes over time. Therefore, the time must also be scaled. For many

Markov processes, such as the continuous random walk considered in example 2.1, for a fixed time t, the distance moved in that time will be of order $\sqrt{(t)}$ as the standard deviation is of this order. So to have significant movement in the macroscopic density profile we must scale time with N^2 and will therefore look at the Markov process $\{\eta_{N^2t}, t \geq 0\}$. The rescaled empirical measure for the hydrodynamic limit will be of the form,

$$\pi_t^N := \frac{1}{N} \sum_{(x,\sigma)\in V} \eta_{N^2t}^N(x,\sigma)\delta_{(\frac{x}{N},\sigma)} \tag{2.23}$$

When paired with a test function $\phi \in C_{c,S}^{\infty}(\mathbb{R})$, π_t^N will be of the form,

$$\pi_t^N(\phi) := \langle \phi, \pi_t^N \rangle = \frac{1}{N} \sum_{(x,\sigma)\in V} \eta_{N^2t}^N(x,\sigma)\phi(\tfrac{x}{N},\sigma) \tag{2.24}$$

As in the case of density functions, the empirical measure converges to a macroscopic measure. This convergence can occur in both probability and in mean square. The two standard convergence notions are defined below.

Definition 2.12. For every, $t \geq 0$, $\epsilon > 0$ and $\phi \in C_{c,S}^{\infty}(\mathbb{R})$, we have convergence in probability for some probability measure μ^ρ if

$$\lim_{N\to\infty} \mathbb{P}_{\mu^\rho}\left(\left|\pi_t^N(\phi) - \sum_{\sigma\in S}\int \rho_t(x,\sigma)\phi(x,\sigma)dx\right| > \epsilon\right) = 0,$$

where $\rho_t(x,\sigma)$ solves the partial differential equation $\dot{\rho}_t = A^*\rho_t$ with the initial condition $\rho_0(x,\sigma) = \rho(x,\sigma)$. Note that A^* is the adjoint generator on a density function (see Definition 2.14).

Definition 2.13. For every, $t \geq 0$ and $\phi \in C_{c,S}^{\infty}(\mathbb{R})$, we have convergence in mean square (L^2-space) for some probability measure μ^ρ if

$$\lim_{N\to\infty} \mathbb{E}_{\mu^\rho}\left(\left|\pi_t^N(\phi) - \sum_{\sigma\in S}\int \rho_t(x,\sigma)\phi(x,\sigma)dx\right|^2\right) = 0,$$

where $\rho_t(x,\sigma)$ solves the partial differential equation $\dot{\rho}_t = A^*\rho_t$ with the initial condition $\rho_0(x,\sigma) = \rho(x,\sigma)$.

Remark 2.1. We recall the connection between PDEs $\dot{\rho}_t = A^*\rho_t$ and semigroups and generators we have covered in Section 2.1. Here, $\rho_t = e^{tA^*}\rho_0$ is the same as the known equation $S_t = e^{tL}$ where ρ_t is the semigroup, and A^* is the generator. Then the PDE follows the Kolmogorov forward equation derived in Proposition 2.3.

Remark 2.2. Using the well known fact that $\mathbb{V}ar[X] = \mathbb{E}[X^2] - \mathbb{E}[X]^2$, we see that Definition 2.13 is implied by,

$$\mathbb{E}\left[\pi_t^N(\phi)\right] \overset{\mu^\rho}{\to} \sum_{\sigma\in S}\int \rho_t(x,\sigma)\phi(x,\sigma)dx$$

and,

$$\mathbb{V}ar\left[\pi_t^N(\phi)\right] \overset{\mu^\rho}{\to} 0$$

When giving the proof for a hydrodynamic limit using test functions, we often have a generator L working on a test function, while we would rather have a generator working on the density. We can make this change using the following definition.

Definition 2.14. Given a compactly supported generator L acting on a test function $\phi \in C_{c,S}^{\infty}$ and a density $\rho \in C^2$ that are both compact. Then its formal adjoint L^* is defined by,

$$\int \rho(x,\sigma)(L\phi)(x,\sigma)dx = \int (L^*\rho)(x,\sigma)\phi(x,\sigma)dx$$

Generally, the formal adjoint L^* can be found by integration by parts as there are no boundary terms.

2.5 Martingales and Dynkin's formula

In this section we introduce martingales and the Dynkin's formula as they are often used in the proof of a hydrodynamic limit. Dynkin's formula uses martingales to give us a simple framework to show that a generator converges to a partial differential equation. Additionally, we introduce two theorems that can be used in proofs following Dynkin's formula. This section is based on theory from the following sources [2, 12, 16]. We start off with the definition of the martingale.

Definition 2.15. A continuous stochastic process $\{M_t, t \geq 0\}$ on $(\Omega, \mathscr{F}, \mathbb{P})$ is called a *martingale* with respect to a filtration $\{\mathscr{F}_t, t \geq 0\}$ if it is an $\mathscr{F}_t$-adapted process such that the *martingale property* is satisfied, i.e., for all $0 \leq s \leq t$ we have,

$$\mathbb{E}[M_t|\mathscr{F}_s] = M_s$$

Note that this shows that a martingale has a constant expectation, and therefore that the best prediction for the future is the current state. We use this definition to state the Dynkin martingale.

Theorem 2.10 (Dynkin's formula)**.** *Let $\{X_t, t \geq 0\}$ be an $\mathscr{F}_t$-adapted Markov process on $(\Omega, \mathscr{F}, \mathbb{P})$, generated by L. Then for any $f \in D(L)$, the process M defined as,*

$$M_t^f := f(X_t) - f(X_0) - \int_0^t Lf(X_s)ds$$

is a martingale on $(\Omega, \mathscr{F}, \mathbb{P})$ with respect to the filtration $\{\mathscr{F}_t, t \geq 0\}$.

Proof. To show that M_t^f is a martingale, we must show it satisfies the martingale property. Choose $0 \leq s \leq t$,

$$\begin{aligned}\mathbb{E}\left[M_t^f - M_s^f|\mathscr{F}_s\right] &= \mathbb{E}\left[f(X_t) - f(X_s) - \int_s^t Lf(X_r)dr \mid \mathscr{F}_s\right] \\ &= \mathbb{E}\left[F(X_t)|\mathscr{F}_s\right] - \mathbb{E}\left[f(X_s)|\mathscr{F}_s\right] - \int_0^{t-s} \mathbb{E}\left[Lf(X_{s+r})|\mathscr{F}_s\right] dr\end{aligned}$$

Here, we used the Fubini theorem in the last equation. Since $\{X_t, t \geq 0\}$ is $\mathscr{F}_t$-adapted and Markovian, the expectation given the whole past $\mathscr{F}_s$ is equal to the expectation given X_s. Combining this with the definition of the semigroup,

$$\begin{aligned}\mathbb{E}\left[M_t^f - M_s^f|\mathscr{F}_s\right] &= \mathbb{E}\left[F(X_t)|X_s\right] - \mathbb{E}\left[f(X_s)|X_s\right] - \int_0^{t-s} \mathbb{E}\left[Lf(X_{s+r})|X_s\right] dr \\ &= S_{t-s}f(X_s) - f(X_s) - \int_0^{t-s} S_r Lf(X_s)dr\end{aligned}$$

Using Proposition 2.3(iii), where we saw that $\frac{d}{dt}S_t f = S_t Lf$, we may rewrite the integral as,

$$\int_0^{t-s} S_r Lf(X_s)dr = \int_0^{t-s} \frac{\partial}{\partial r} S_r f(X_s)dr = S_{t-s}f(X_s) - f(X_s).$$

Hence we indeed find that

$$\mathbb{E}\left[M_t^f - M_s^f|\mathscr{F}_s\right] = S_{t-s}f(X_s) - f(X_s) - S_{t-s}f(X_s) + f(X_s) = 0,$$

therefore M_t^f is a martingale with respect to the filtration $\mathscr{F}_t$. □

Proving hydrodynamic limits using Dynkin's formula requires us to show that the martingale associated to the empirical measure goes to zero in the scaling limit as $N \to \infty$, as this shows us the limiting solution is deterministic. For this we use three extra theorems for which we first need to introduce quadratic variation of a martingale which is done in the following two definitions.

Definition 2.16. Let $P = \{t_0, t_1, ..., t_n\}$ be a partition of the interval $[0, t]$ such that $0 = t_0 < t_1 < ... < t_n = t$. The *mesh size* of this partition is a norm $||\cdot||_m$ defined as

$$||P||_m = \max_{1 \leq k \leq m} |t_k - t_{k-1}|$$

Definition 2.17. Let M be a càdlàg local martingale on $(\Omega, \mathscr{F}, \mathbb{P})$, then the *optional quadratic variation* $[M]_t$ of M is defined as the limit in probability of the sum of squared increments.

$$[M]_t := \lim_{||P||_m \to 0} \sum_{k=1}^{n} (M_{t_k} - M_{t_{k-1}})^2 \tag{2.25}$$

Theorem 2.11. *Let M be a martingale on $(\Omega, \mathscr{F}, \mathbb{P})$ such that $M_t \in L^2(\Omega, \mathscr{F}, \mathbb{P})$ for all $t \geq 0$ and $M_0 = 0$, then there exists a unique predictable quadratic variation $\langle M \rangle$ starting at zero such that $[M] - \langle M \rangle$ is a martingale.*

Note that if M is continuous, then $[M] = \langle M \rangle$. To express the quadratic variation of the Dynkin martingale, we first introduce the *carré du champ* operator.

Definition 2.18. Let L be the generator of a Markov process. The *carré du champ* operator $\Gamma(f, g)$ is defined for functions f, g (where $f, g, fg \in D(L)$) as:

$$\Gamma(f, g) = L(fg) - f(Lg) - g(Lf) \tag{2.26}$$

In the case where $f = g$, we denote $\Gamma(f) := \Gamma(f, f) = L(f^2) - 2f(Lf)$.

We can now state the two theorems below and will apply the second theorem to the example of the continuous random walk generator. The proofs for these theorems can be found in the references given for this section.

Theorem 2.12 (Doob's L^p inequality)**.** *Let M_t be a martingale indexed by an interval $[0, t]$ of real numbers, relative to a filtration $\mathscr{F}_t$. Then for $p > 1$,*

$$\mathbb{E}\left[\sup_{0 \leq s \leq t} |M_s|^p\right] \leq \left(\frac{p}{p-1}\right)^p \mathbb{E}\left[|M_t|^p\right] \tag{2.27}$$

Theorem 2.13. *Let L be the generator of a Markov process X and take $f \in D(L)$ such that $f^2 \in D(L)$. Then the predictable quadratic variation of the Dynkin martingale is given by,*

$$\langle M^f \rangle_t = \int_0^t \Gamma(f)(X_s) ds \tag{2.28}$$

Example 2.3. As Theorem 2.13 will be applied often, we will apply it to the generator for the continuous random walk we found in Example 2.1 to simplify proofs later. Remember that the generator for the continuous random walk was given by

$$Lf = \sum_{y \in \Omega} [c(x, y)(f(y) - f(x))]$$

We first compute the carré du champ operator $\Gamma(f) = Lf^2 - 2fLf$:

Applying Theorem 2.13 for a function f that satisfies its requirement gives,

$$\begin{aligned}
\Gamma(f)(\eta) &= \sum_{\eta' \in \Omega} c(\eta, \eta') \left(f^2(\eta') - f^2(\eta)\right) - 2f(\eta) \sum_{\eta' \in \Omega} c(\eta, \eta') \left(f(\eta') - f(\eta)\right) \\
&= \sum_{\eta' \in \Omega} \left(c(\eta, \eta') \left(f^2(\eta') - 2f(\eta) f(\eta') + f^2(\eta)\right)\right) \\
&= \sum_{\eta' \in \Omega} \left(c(\eta, \eta') \left(f(\eta') - f(\eta)\right)^2\right)
\end{aligned}$$

Substituting this into Theorem 2.13, the quadratic variation of the Dynkin martingale is given by

$$\langle M \rangle_t = \int_0^t \left[\sum_{\eta' \in \Omega} \left(c(\eta_s, \eta') \left(f(\eta') - f(\eta_s)\right)^2\right] ds \tag{2.29}$$

2.6 Brownian motion and the Fokker-Planck equation

In this section we introduce Brownian motion and the Fokker-Planck equation. This is done as later results, following from the analysis of the hydrodynamic limit, can easily be linked to Brownian motion. This allows for a broader interpretation of the results. The section start with the definition of Brownian motion, with does not include a drift, and relates this to continuous random walk seen in Section 2.1, PDEs and stochastic differential equations (SDEs). The remainder of this section focuses on the Fokker-Planck equation in which an effective drift term is present. The following section is based on [2, 12, 17].

2.6.1 Simple Brownian motion and its relation to the symmetric random walk

Brownian motion originates from the erratic trajectories of pollen grains observed by Robert Brown in 1827. Since then this phenomena, simply the random collisions of any particle causing it to undergo irregular and erratic motion, has been observed in many fields and turned into a large mathematical object. It allows us to understand why associated PDEs (i.e. drift-diffusion equations) appear naturally in the hydrodynamic limits of stochastic particle systems. Mathematically, Brownian motion is defined as follows,

Definition 2.19. A stochastic process $\{B_t, t \geq 0\}$ is called *Brownian motion* if:

(*i*) $B_0 = 0$.

(*ii*) All increments are independent. That is for $0 = t_0 \leq t_1 \leq \ \ldots \ \leq t_m$, $B_{t_1} - B_{t_0}, B_{t_2} - B_{t_1}, \ \ldots \ , B_{t_m} - B_{t_{m-1}}$ are independent.

(*iii*) For all $s < t$, the increments are normally distributed with,

$$\mathbb{E}[B_t - B_s] = 0, \qquad \mathbb{V}\mathrm{ar}(B_t - B_s) = t - s \tag{2.30}$$

(*iv*) Sample paths $t \mapsto B_t$ are continuous.

This definition shows us, that intuitively speaking, Brownian motion is continuous random motion with no preferred direction and alinearly growing variance. One can also consider Brownian motion starting from a position x. Then by the independence of increments it can be shown that $B_t = x + \mathcal{N}(0, t)$ is indeed an equivalent description of Brownian motion. In the sections prior to this we have mostly studied continuous random walks $\{X_t, t \geq 0\}$. This is closely related to Brownian motion and actually equivalent under the same scaling of time and space that was introduced in Section 2.4. This is summarized in the following theorem, for which a sketch of the proof will be given below.

Theorem 2.14. *A symmetric random walk $\{X_t, t \geq 0\}$ has the scaling limit $\{B_t, t \geq 0\}$ (i.e. Brownian motion) by scaling $x \to x/N$ and $t \to tN^2$,*

$$X_t^N := \{\tfrac{1}{N} X_{N^2 t}, t \geq 0\} \ \xrightarrow{N \to \infty} \ \{\sqrt{2D} B_t, t \geq 0\} \tag{2.31}$$

Proof. We sketch this proof by showing that the symmetric random walk and Brownian motion have the same generators and therefore have similar probabilistic behavior. Note that for the symmetric random walk the generator is defined as:

$$L_N f(x) = \frac{1}{2} \frac{f(x + \frac{1}{N}) - 2f(x) + f(x - \frac{1}{N})}{N^2} \tag{2.32}$$

Taking the Taylor expansion and the limit $N \to \infty$ gives

$$\lim_{N \to \infty} L_N f(x) = \frac{1}{2} f''(x) \tag{2.33}$$

With the generator for the symmetric random walk in hand, we are left with finding the generator for Brownian motion. Note that $B_t = x + \mathcal{N}(0, \sqrt{2D}t)$ was equivalent to Brownian motion with

diffusion coefficient D. Therefore we can find that the semigroup is given by,

$$\begin{aligned} S_t f(x) &= \mathbb{E}_x \left[f(x + \mathcal{N}(0, \sqrt{2D}t) \right] \\ &= f(x) + f'(x)\mathbb{E}_x \left[\mathcal{N}(0, \sqrt{2D}t) \right] + \frac{1}{2} f''(x)\mathbb{E}_x \left[\mathcal{N}(0, \sqrt{2D}t)^2 \right] + \mathcal{O}(t) \\ &= f(x) + Df''(x)t + \mathcal{O}(t) \end{aligned}$$

Now, using the definition of the generator we see that the generator for the symmetric random walk and Brownian motion are indeed equivalent using the scaling $\sqrt{2D}$,

$$L_B f(x) = \lim_{t \to 0} \frac{S_t f(x) - f(x)}{t} = Df''(x) \tag{2.34}$$

□

2.6.2 Simple Brownian motion and its relation to PDEs and SDEs

To relate random walks to PDEs, we start by relating Brownian motion to SDEs and PDEs. This section focuses on relating simple Brownian motion to PDEs and SDEs, whereas the following section does this for Brownian motion where an active part is also present. In a similar fashion as the convergence, the SDE relating a random walk to Brownian motion is given by,

$$dX_t = \sqrt{2D} dB_t \tag{2.35}$$

Note that this follows immediately from the fact that,

$$X_{t+\Delta t} - X_t \approx \sqrt{2D}\sqrt{\Delta t}\, \mathcal{N}(0, t)$$

This SDE corresponds to the following PDE,

$$\frac{\partial \rho}{\partial t} = D \frac{\partial^2 \rho}{\partial x^2} \tag{2.36}$$

The PDE and SDE are two equivalent formulations of the same underlying phenomenon, one probabilistic, one deterministic. Note that the fundament solution of the PDE, a Gaussian, matches the stochastic description

$$\rho(x, t) = \frac{1}{\sqrt{4\pi D t}} e^{-\frac{x^2}{4Dt}} \tag{2.37}$$

2.6.3 Brownian motion with drift

If a constant directional bias is present, such as self-propulsion, the local motion involves a drift velocity v. The associated SDE can be found by considering not a probability 1/2 to move to the left or right but instead r_+ and r_-. This will result in the advection-diffusion SDE,

$$dX_t = v dt + \sqrt{2D} dB_t \tag{2.38}$$

where $v = r_+ - r_-$ and $D = \frac{1}{2}(r_+ + r_-)$. We can relate this SDE to the associate PDE using the Kolmogorov Forward equation,

Theorem 2.15 (Kolmogorov Forward equation)**.** *For standard Brownian motion B_t with the associated SDE*

$$dX_t = v dt + \sqrt{2D} dB_t$$

The Fokker-Planck equation for the probability density is given by,

$$\partial_t \rho = -\partial_x (v\rho) + \partial_x^2 (D\rho) \tag{2.39}$$

Proof. We sketch the proof of this theorem using the Kolmogorov forward equation given in Proposition 2.3 and the adjoint operator given in Definition 2.14. Remember that the Kolmogorov forward equation was given by,

$$\frac{d}{dt}\mathbb{E}[f(X_t)] = \mathbb{E}[Lf(X_t)]$$

Expression the expectations as integrals over the density $\rho(x,t)$ and using the adjoint operator one finds

$$\frac{\partial \rho}{\partial t} = L^*\rho$$

Note that generator of SDE is given by

$$Lf(x) = v\frac{\partial f}{\partial x} + D\frac{\partial^2 f}{\partial x^2}$$

Calculting the adjoint L^* immediatelly gives the PDE. □

Note that the solution of the PDE is a Gaussian centered at vt,

$$\rho(x,t) = \frac{1}{\sqrt{4\pi D t}} e^{-\frac{(x-vt)^2}{4Dt}} \tag{2.40}$$

In section 3 we derive the hydrodynamic limit of a much more complex interacting particle system. However, in section and 4 we will see that, at large scales, the system will behave like the PDE above, and thus like Brownian motion with effective diffusion coefficient D and effective velocity v. This is an example of the many models that many stochastic microscopic models reduce, at large scales, to a drift-diffusion model and that have the same scale invariance as Brownian motion.

3 Model and proof of the hydrodynamic limit under the global and local magnetization

In this section, we bridge the gap between the microscopic stochastic dynamics of active particles and the macroscopic deterministic description derived in the hydrodynamic limit. We begin by defining the specific microscopic interacting particle system acting on a one-dimensional lattice, incorporating diffusion, active transport, and internal state switching. The core of this section is dedicated to proving that, under the hydrodynamic scaling introduced in Section 2.4, the empirical measure of this process converges to a solution of a nonlinear partial differential equation (PDE).

Section 3.1 defines the microscopic model and presents a proof of the hydrodynamic limit for the global magnetization and derives the associated reaction-diffusion-advection equation. Subsequently, Section 3.2 extends this validity to the case of local magnetization. Since local interactions involve non-smooth functions, which violate the assumptions in the main proof, we provide a proof demonstrating that the discrete local magnetization converges to its continuous counterpart. This closes the only gap in the proof and the rest of the proof remains the same as in the case of the global magnetization.

3.1 Proof for the global magnetization

We explicitly define the dynamics of the active particle system that is the focus of this thesis. The model describes a collection of independent particles moving an one-dimensional domain X_N, this can either be a discrete torus $X_N = \mathbb{T}_N$ or on an infinite line $X_N = \mathbb{Z}$ each carrying an internal state $\sigma \in S = \{-1, 1\}$ that determines its direction of motion. The full configuration is therefore of the form:

$$V_N := X_N \times S, \qquad \Omega_N = \mathbb{N}^{V_N} \tag{3.1}$$

where $\eta(x, \sigma) \in \Omega_N$ assigns to each site the number of particles at position x with internal state σ. Each of these particles moves according to three types of dynamics:

- (i) Diffusion: at rate $\gamma_N = \gamma N^2$ a particle performs a nearest neighbor jump, i.e., $(x, \sigma) \to (x \pm 1, \sigma)$.
- (ii) Active jump: at rate $\lambda_N = \lambda N$ a particle performs an active jump in the direction of its internal state, i.e., $(x, \sigma) \to (x + \sigma, \sigma)$.
- (iii) Internal state flip: at mean-field rate $c(\sigma, m_N(\eta))$ a particle flips its internal state, i.e., $(x, \sigma) \to (x, -\sigma)$.

These three types of dynamics give rise to the following generator L_N acting on $f : \Omega_N \to \mathbb{R}$:

$$\begin{aligned} L_N f(\eta) = \gamma_N &\sum_{(x,\sigma)\in V_N} \eta(x,\sigma) \left(f(\eta^{(x,\sigma)\to(x+1,\sigma)}) + f(\eta^{(x,\sigma)\to(x-1,\sigma)}) - 2f(\eta) \right) \\ &+ \lambda_N \sum_{(x,\sigma)\in V_N} \eta(x,\sigma) \left(f(\eta^{(x,\sigma)\to(x+\sigma,\sigma)}) - f(\eta) \right) \\ &+ \sum_{(x,\sigma)\in V_N} c(\sigma, m_N(\eta))\eta(x,\sigma) \left(f(\eta^{(x,\sigma)\to(x,-\sigma)}) - f(\eta) \right) \end{aligned}$$

Here the configuration $\eta^{(x,\sigma)\to(y,\sigma)}$ is obtained by moving one particle from (x, σ) to (y, σ). Mathematically,

$$\eta^{x,y}(z) := \begin{cases} \eta(z), & \text{if } z \notin \{x, y\}, \\ \eta(x), & \text{if } z = y, \\ \eta(y), & \text{if } z = x. \end{cases} \tag{3.2}$$

In this discrete case, the magnetization is defined as,

$$m_N(\eta) := \frac{1}{|\eta|} \sum_{x\in X_N} (\eta(x, 1) - \eta(x, -1)) \qquad \text{where } |\eta| := \sum_{(x,\sigma)\in V_N} \eta(x, \sigma) \tag{3.3}$$

Using the definition of the empirical measure given in Equation (2.23), $m_N(\eta)$ can be written as the following,

$$m_N(\eta_t^N) = m(\pi_t^N(\eta)) := \frac{\langle \pi_t^N(\eta), \mathbb{1}_{\sigma=1} - \mathbb{1}_{\sigma=-1} \rangle}{\langle \pi_t^N(\eta), 1 \rangle} \tag{3.4}$$

This motivates the following definition of the magnetization corresponding to a density $\rho(x,\sigma) : V \to \mathbb{R}_{\geq 0}$:

$$m(\rho) = \frac{\langle \rho, \mathbb{1}_{\sigma=1} - \mathbb{1}_{\sigma=-1} \rangle}{\langle \rho, 1 \rangle} \tag{3.5}$$

Which represents the average orientation of the particle system. We initialize the system with an independent number of particles to each site according to a Poisson-distribution. This is consistent with the macroscopic profile $\rho_0 : [0,1] \times S \to \mathbb{R}_{\geq 0}$,

$$\mu_N^\rho = \bigotimes_{(x,\sigma)\in V} \text{Pois}\left(\rho_0\left(\frac{x}{N}, \sigma\right)\right) \tag{3.6}$$

Note that this measure satisfies Definition 2.11 because the resulting empirical measure $\pi_0^N(\phi)$ converges in probability to the macroscopic density profile ρ_0 as $N \to \infty$. This is the case as the test function is chosen such that on the periodic domain $V = \mathbb{T}_N$, ϕ is taken to be periodic and on the infinite domain $V = \mathbb{Z}$, ϕ is assumed to have compact support (Definition 2.11). With these definitions in hand, we are able to prove to which partial differential equation this microscopic process converges in the hydrodynamic limit, as $N \to \infty$. For this proof, we need the following lemma,

Lemma 3.1. *Let η_0^N be distributed according to the product Poisson measure of Equation (3.6) with $\rho_0 : [0,1] \times S \to \mathbb{R}_{\geq 0}$. Consider the independent particle dynamics given above. Then, for every $t \geq 0$, the law of η_t^N is again a product Poisson measure with parameters $\rho_t^N(x,\sigma) = \mathbb{E}[\eta_t^N(x,\sigma)]$, i.e.,*

$$\eta_t^N(x,\sigma) \sim Pois(\rho_t^N(x,\sigma)), \qquad \textit{independently for each } (x,\sigma) \in V_N$$

Proof. See Kipnis & Landim chapter 1.3 for the proof [22]. □

Theorem 3.2. *Let $\rho_0 \in C_{c,S}^\infty$ be an initial macroscopic profile and let μ_N^ρ be the compatible initial conditions. Then, for every $t \geq 0$, we have*

$$\lim_{N\to\infty} \mathbb{E}_{\mu_N^\rho}\left(\left|\pi_t^N(\phi) - \sum_{\sigma\in S}\int \rho_t(x,\sigma)\phi(x,\sigma)dx\right|^2\right) = 0,$$

where ρ_t satisfies the following partial differential equation,

$$\dot{\rho}_t(x,\sigma) = \gamma\Delta\rho_t(x,\sigma) - \sigma\lambda\partial_x\rho_t(x,\sigma) + c(-\sigma, m(\rho_t))\rho_t(x,-\sigma) - c(\sigma, m(\rho_t))\rho_t(x,\sigma) \tag{3.7}$$

with initial condition $\rho_0(x,\sigma) = \rho(x,\sigma)$, where $0 \leq c(\sigma, m(\rho_t)) \leq C_c$ for $C_c \in \mathbb{R}_{\geq 0}$

Proof. We prove Theorem 3.2 using Dynkin's formula given in Theorem 2.10. Dynkin's formula will take the following form,

$$M_t^N(\phi) = \pi_t^N(\phi) - \pi_0^N(\phi) + \int_0^t L_N\pi_s^N(\phi)ds \tag{3.8}$$

We start this proof by showing $\pi_0^N(\phi)$ converges to $\langle \rho_0, \phi \rangle$. Afterwards, we will show the integral containing the generator converges to an integral containing the PDE. We will finish by showing the martingale M_t^N vanishes. Additionally as the test functions ϕ are either periodic or have compact support the boundary terms that arise when using integration by parts will be zero for either boundary condition, leading to the same macroscopic equation

Note that η_0^N is distributed according to the Poisson measure with the macroscopic profile ρ_0 as defined by Equation (3.6). This gives that empirical measure at time $t = 0$ is given by,

$$\pi_0^N(\phi) = \frac{1}{N} \sum_{(x,\sigma)\in V_N} \eta_0^N(x,\sigma)\phi\left(\frac{x}{N},\sigma\right)$$

We now show $\pi_0^N(\phi)$ converges to $\langle \rho_0, \phi\rangle$ in the L^2-space, by showing the expectation converges to $\langle \rho_0, \phi\rangle$, while the variance goes to zero.

$$\begin{aligned}
\mathbb{E}\left[\pi_0^N(\phi)\right] &= \frac{1}{N} \sum_{(x,\sigma)\in V_N} \phi\left(\frac{x}{N},\sigma\right) \mathbb{E}\left[\eta_0^N(x,\sigma)\right] \\
&= \frac{1}{N} \sum_{(x,\sigma)\in V_N} \phi\left(\frac{x}{N},\sigma\right) \rho_0\left(\frac{x}{N},\sigma\right) \\
&= \sum_{\sigma\in S} \int_0^1 \phi(x,\sigma)\rho_0(x,\sigma)dx = \langle \rho_0, \phi\rangle
\end{aligned}$$

We may go from the sum to the integral as this is the exact Riemann sum that approximates the integral over the torus.

$$\mathbb{V}ar\left[\pi_0^N(\phi)\right] = \frac{1}{N^2} \sum_{(x,\sigma)\in V_N} \phi^2\left(\frac{x}{N},\sigma\right) \mathbb{V}ar\left[\eta_0^N(x,\sigma)\right] = \frac{1}{N^2} \sum_{(x,\sigma)\in V_N} \phi^2\left(\frac{x}{N},\sigma\right) \rho_0\left(\frac{x}{N},\sigma\right) = \mathcal{O}\left(\frac{1}{N}\right)$$

As the sum has N spacial terms we are left with $\mathcal{O}\left(\frac{1}{N}\right)$. This shows us that $\pi_0^N(\phi)$ converges to $\langle \rho_0, \phi\rangle$ in the L^2 sense.

Now, we show that the integral converges to one containing ρ_t. Before doing this, we must show that $\pi_t^N \to \rho_t dx$ in the L^2 sense. This requires us to show to the expectation of $\pi_t^N(\phi)$ converges to $\langle \rho_t, \phi\rangle$ and that its variance vanishes.

$$\begin{aligned}
\mathbb{E}\left[\pi_t^N(\phi)\right] &= \frac{1}{N} \sum_{(x,\sigma)\in V_N} \phi\left(\frac{x}{N},\sigma\right) \mathbb{E}\left[\eta_t^N(x,\sigma)\right] \\
&= \frac{1}{N} \sum_{(x,\sigma)\in V_N} \phi\left(\frac{x}{N},\sigma\right) \rho_t\left(\frac{x}{N},\sigma\right) \\
&= \sum_{\sigma\in S} \int_0^1 \phi(x,\sigma)\rho_t(x,\sigma)dx = \langle \rho_t, \phi\rangle
\end{aligned}$$

To go from line one to line two we use the Poisson invariance for independent particles presented in Lemma 3.1. By exactly the same argument as for the convergence of the initial condition one can see that the variance goes to zero.

To improve readability, the convergence of the generator L to the PDE is split into three parts, i.e., the three processes of this system. For each of these three processes a test function as defined in Equation (2.24) is used. Additionally, Taylor expansion, Proposition 2.3(iii) and the adjoint relation as defined in definition 2.14 are used to complete this part if the proof. Applying the generator of the diffusive part to a test function gives us,

$$
\begin{aligned}
L_N^{dif}\pi_t^N(\phi) &= \gamma_N \sum_{(x,\sigma)\in V_N} \eta_t^N(x,\sigma)(\langle \pi_t^N(\eta^{(x,\sigma),\ \to(x+1,\sigma)}),\phi\rangle + \langle \pi_t^N(\eta^{(x,\sigma),\ \to(x-1,\sigma)}),\phi\rangle \\
&\quad - 2\langle \pi_t^N(\eta),\phi\rangle) \\
&= \frac{\gamma_N}{N} \sum_{(x,\sigma)\in V_N} \eta_t^N(x,\sigma)\left(\phi\left(\frac{x+1}{N},\sigma\right) + \phi\left(\frac{x-1}{N},\sigma\right) - 2\phi\left(\frac{x}{N},\sigma\right)\right) \\
&= \gamma_N\left(\frac{1}{N^3}\sum_{(x,\sigma)\in V_N} \eta_t^N(x,\sigma)\phi''\left(\frac{x}{N},\sigma\right) + \mathcal{O}\left(\frac{1}{N^3}\right)\right) \\
&= \gamma_N\left(\frac{1}{N^2}\pi_t^N(\phi'') + \mathcal{O}\left(\frac{1}{N^3}\right)\right) = \gamma\pi_t^N(\phi'') + \mathcal{O}\left(\frac{1}{N}\right)
\end{aligned}
$$

This shows why we scale γ with N^2. Using Proposition 2.3(iii),

$$
\frac{\partial}{\partial t}\mathbb{E}\left[\pi_t^N(\phi)\right] = \mathbb{E}\left[L_N^{dif}\pi_t^N(\phi)\right] = \mathbb{E}\left[\gamma\pi_t^N(\phi'')\right]
$$

Using $\pi_t^N \to \rho_t dx$, the Riemann sum and integrating by parts to find the adjoint relation, we find this is equivalent to,

$$
\frac{\partial}{\partial t}\sum_{\sigma\in S}\int \rho_t(x,\sigma)\phi(x,\sigma)dx = \sum_{\sigma\in S}\int \rho_t(x,\sigma)\gamma\phi''(x,\sigma)dx = \sum_{\sigma\in S}\int \gamma\rho_t''(x,\sigma)\phi(x,\sigma)dx
$$

Both the integral and the sum must hold for any region and therefore,

$$
\frac{\partial\rho_t(x,\sigma)}{\partial t} = \gamma\frac{\partial^2\rho_t(x,\sigma)}{\partial x^2} \tag{3.9}
$$

For the active jumps, we again apply the generator for this active part to a test function,

$$
\begin{aligned}
L_N^{act}\pi_t^N(\phi) &= \lambda_N \sum_{(x,\sigma)\in V_N} \eta_t^N(x,\sigma)\left(\langle \pi_t^N(\eta^{(x,\sigma),\ \to(x+\sigma,\sigma)}),\phi\rangle - \langle \pi_t^N(\eta),\phi\rangle\right) \\
&= \frac{\lambda_N}{N}\sum_{(x,\sigma)\in V_N} \eta_t^N(x,\sigma)\left(\phi\left(\frac{x+\sigma}{N},\sigma\right) - \phi\left(\frac{x}{N},\sigma\right)\right)
\end{aligned}
$$

Note that if we Taylor expand $\phi\left(\frac{x+\sigma}{N}\right)$ around x/N we find,

$$
\phi\left(\frac{x+\sigma}{N}\right) = \phi\left(\frac{x}{N}\right) + \phi'\left(\frac{x}{N}\right)\left(\frac{x+\sigma}{N} - \frac{x}{N}\right) + \mathcal{O}\left(\frac{1}{N^2}\right) = \phi\left(\frac{x}{N}\right) + \frac{\sigma}{N}\phi'\left(\frac{x}{N}\right) + \mathcal{O}\left(\frac{1}{N^2}\right)
$$

and we can thus rewite the generator to,

$$
\begin{aligned}
L_N^{act}\pi_{\eta(N^2t)}^N(\phi) &= \lambda_N\left(\frac{\sigma}{N^2}\sum_{(x,\sigma)\in V_N} \eta_{N^2t}^N(x,\sigma)\phi'\left(\frac{x}{N},\sigma\right) + \mathcal{O}\left(\frac{1}{N^2}\right)\right) \\
&= \lambda_N\left(\frac{\sigma}{N}\pi_t^N(\phi') + \mathcal{O}\left(\frac{1}{N^2}\right)\right) = \lambda\sigma\pi_t^N(\phi') + \mathcal{O}\left(\frac{1}{N}\right)
\end{aligned}
$$

This shows why we scale λ with N. Using Proposition 2.3(iii),

$$
\frac{\partial}{\partial t}\mathbb{E}\left[\pi_t^N(\phi)\right] = \mathbb{E}\left[L_N^{act}\pi_t^N(\phi)\right] = \mathbb{E}\left[\lambda\sigma\pi_t^N(\phi')\right]
$$

Equivalently,

$$
\frac{\partial}{\partial t}\sum_{\sigma\in S}\int \rho_t(x,\sigma)\phi(x,\sigma)dx = \sum_{\sigma\in S}\int \rho_t(x,\sigma)\sigma\lambda\phi'(x,\sigma)dx = -\sum_{\sigma\in S}\int \sigma\lambda\rho_t'(x,\sigma)\phi(x,\sigma)dx
$$

Note that the final expression contains a minus sign. This is the case as we only use integrate by parts once to find the adjoint generator L^*, whereas in the case of diffusion, we do this twice. Finally, we have,

$$\frac{\partial \rho_t(x,\sigma)}{\partial t} = -\lambda\sigma \frac{\partial \rho_t(x,\sigma)}{\partial x} \tag{3.10}$$

For the internal state flips, we apply its generator to a test function,

$$\begin{aligned} L_N^{int}\pi_t^N(\phi) &= \sum_{(x,\sigma)\in V_N} \eta_t^N(x,\sigma)c(\sigma, m_N(\eta))\left(\langle \pi_t^N(\eta^{(x,\sigma),\,\to(x,-\sigma)}),\phi\rangle - \langle \pi_t^N(\eta),\phi\rangle\right) \\ &= \frac{1}{N}\sum_{(x,\sigma)\in V_N} \eta_t^N(x,\sigma)c(\sigma, m(\pi_t^N(\eta)))\left(\phi\left(\frac{x}{N},-\sigma\right) - \phi\left(\frac{x}{N},\sigma\right)\right) \end{aligned}$$

This shows as we do not have to scale c. Following the procedure we have seen twice before, we get,

$$\frac{\partial}{\partial t}\mathbb{E}\left[\pi_t^N(\phi)\right] = \mathbb{E}\left[L_N^{int}\pi^N_{\eta(N^2t)}(\phi)\right] = \mathbb{E}\left[c(\sigma, m(\rho_t))\left(\pi_t^N(\phi(x,-\sigma)) - \pi_t^N(\phi(x,\sigma))\right)\right]$$

We simplify this further to find,

$$\begin{aligned} \frac{\partial}{\partial t}\sum_{\sigma\in S}\int \rho_t(x,\sigma)\phi(x,\sigma)dx &= \sum_{\sigma\in S}\int \rho_t(x,\sigma)c(\sigma,m(\rho_t))\left(\phi(x,-\sigma)-\phi(x,\sigma)\right)dx \\ &= \sum_{\sigma\in S}\int \rho_t(x,\sigma)c(\sigma,m(\rho_t))\phi(x,-\sigma)dx - \sum_{\sigma\in S}\int \rho_t(x,\sigma)c(\sigma,m(\rho_t))\phi(x,\sigma)dx \\ &= \sum_{\sigma'\in S}\int \rho_t(x,-\sigma')c(-\sigma',m(\rho_t))\phi(x,\sigma')dx - \sum_{\sigma\in S}\int \rho_t(x,\sigma)c(\sigma,m(\rho_t))\phi(x,\sigma)dx \\ &= \sum_{\sigma\in S}\int \left[c(-\sigma,m(\rho_t))\rho_t(x,-\sigma) - c(\sigma,m(\rho_t))\rho_t(x,\sigma)\right]\phi(x,\sigma)dx \end{aligned}$$

and we thus have the following PDE for the internal state jumps,

$$\frac{d\rho_t(x,\sigma)}{dt} = c(-\sigma,m(\rho_t))\rho_t(x,-\sigma) - c(\sigma,m(\rho_t))\rho_t(x,\sigma) \tag{3.11}$$

Combining Equation (3.9)-(3.11) gives the desired partial differential equation. We are only left with showing that the martingale $M_t^N(\phi)$ goes to zero. This part of the proof is an adapted version of the proof by Van Wiechen [16]. Note that because of the initial conditions we have as $N\to\infty$, $\mathbb{E}[M_0^N]=0$ and therefore $\mathbb{E}[M_t^N]=0$ for all $t\geq 0$ since it has a constant expectation. Therefore it is enough to show,

$$\lim_{N\to\infty}\mathbb{E}\left[\sup_{0\leq s\leq t}(M_s^N)^2\right] = 0$$

By Doob's L^p inequality (2.12), we have that,

$$\mathbb{E}\left[\sup_{0\leq s\leq t}(M_s^N)^2\right] \leq 4\mathbb{E}\left[(M_t^N)^2\right] = 4\mathbb{E}\left[\langle M^N\rangle_t\right]$$

We now use Theorem 2.13, which shows that $\langle M^N\rangle_t$ is given by,

$$\langle M^N\rangle_t = \int_0^t [L_N(\pi_s^N(\phi))^2 - 2\pi_s^N(\phi)L_N\pi_s^N(\phi)]ds$$

Using Example 2.3, we see that for the for generator of this model we have,

$$
\begin{aligned}
&L_N(\pi_s^N(\phi))^2 - 2\pi_s^N(\phi)L_N\pi_s^N(\phi) \\
&\quad= \gamma_N \sum_{(x,\sigma)\in V_N} \eta_s^N(x,\sigma)\frac{1}{N^2}\left(\left[\phi\left(\frac{x+1}{N},\sigma\right) - \phi\left(\frac{x}{N},\sigma\right)\right]^2 + \left[\phi\left(\frac{x-1}{N},\sigma\right) - \phi\left(\frac{x}{N},\sigma\right)\right]^2\right) \\
&\quad+ \lambda_N \sum_{(x,\sigma)\in V_N} \eta_s^N(x,\sigma)\frac{1}{N^2}\left(\left[\phi\left(\frac{x+\sigma}{N},\sigma\right) - \phi\left(\frac{x}{N},\sigma\right)\right]^2\right) \\
&\quad+ \sum_{(x,\sigma)\in V_N} c(\sigma, m_N(\eta))\eta_s^N(x,\sigma)\frac{1}{N^2}\left(\left[\phi\left(\frac{x}{N},-\sigma\right) - \phi\left(\frac{x}{N},\sigma\right)\right]^2\right)
\end{aligned}
$$

We must simplify the term for the internal flips. Note that $(\phi(\sigma) - \phi(-\sigma))^2 = (\phi(-\sigma) - \phi(\sigma))^2$, $(a-b)^2 \le 2a^2 + 2b^2$ and that we assumed $0 \le c(\sigma, m_N(\eta)) \le C_c$,

$$
\begin{aligned}
&\sum_{(x,\sigma)\in V_N} c(\sigma, m_N(\eta))\eta_s^N(x,\sigma)\frac{1}{N^2}\left(\left[\phi\left(\frac{x}{N},-\sigma\right) - \phi\left(\frac{x}{N},\sigma\right)\right]^2\right) \\
&\le \frac{C_c}{N^2}\sum_{x\in X_N}\left(\eta_s^N(x,\sigma) + \eta_s^N(x,-\sigma)\right)\left[\phi\left(\frac{x}{N},-\sigma\right) - \phi\left(\frac{x}{N},\sigma\right)\right]^2 \\
&\le \frac{C_c}{N^2}\sum_{x\in X_N}\left(\eta_s^N(x,\sigma) + \eta_s^N(x,-\sigma)\right)\left[2\phi^2\left(\frac{x}{N},-\sigma\right) + 2\phi^2\left(\frac{x}{N},\sigma\right)\right] \\
&= \frac{2C_c}{N^2}\sum_{x\in X_N}\left(\left(\eta_s^N(x,\sigma) + \eta_s^N(x,-\sigma)\right)\sum_{\sigma\in S}\phi^2\left(\frac{x}{N},\sigma\right)\right)
\end{aligned}
$$

Using Taylor expansion we find,

$$
\begin{aligned}
&L_N(\pi_s^N(\phi))^2 - 2\pi_s^N(\phi)L_N\pi_s^N(\phi) \le \gamma\sum_{(x,\sigma)\in V_N}\eta_s^N(x,\sigma)\left(\left[\frac{1}{N}\phi' + \frac{1}{2N^2}\phi''\right]^2 + \left[-\frac{1}{N}\phi' + \frac{1}{2N^2}\phi''\right]^2\right) \\
&+ \frac{\lambda}{N}\sum_{(x,\sigma)\in V_N}\eta_s^N(x,\sigma)\left(\left[\frac{\sigma}{N}\phi' + \frac{\sigma^2}{2N^2}\phi''\right]^2\right) + \frac{2C_c}{N^2}\sum_{x\in X_N}\left(\left(\eta_s^N(x,\sigma) + \eta_s^N(x,-\sigma)\right)\sum_{\sigma\in S}\phi^2\left(\frac{x}{N},\sigma\right)\right) \\
&= \gamma\sum_{(x,\sigma)\in V_N}\eta_s^N(x,\sigma)\left(\left[2\left(\frac{1}{N}\phi'\right)^2 + \mathcal{O}\left(\frac{1}{N^3}\right)\right]\right) + \frac{\lambda}{N}\sum_{(x,\sigma)\in V_N}\eta_s^N(x,\sigma)\left(\left[\left(\frac{\sigma}{N}\phi'\right)^2 + \mathcal{O}\left(\frac{1}{N^3}\right)\right]\right) \\
&+ \frac{2C_c}{N^2}\sum_{x\in X_N}\left(\left(\eta_s^N(x,\sigma) + \eta_s^N(x,-\sigma)\right)\sum_{\sigma\in S}\phi^2\left(\frac{x}{N},\sigma\right)\right) \\
&= \frac{4\gamma}{N^2}\sum_{(x,\sigma)\in V_N}\eta_s^N(x,\sigma)\left(\phi'\left(\frac{x}{N},\sigma\right)^2\right) + \frac{\lambda}{N^3}\sum_{(x,\sigma)\in V_N}\eta_s^N(x,\sigma)\sigma^2\left(\phi'\left(\frac{x}{N},\sigma\right)^2\right) \\
&+ \frac{2C_c}{N^2}\sum_{x\in X_N}\left(\left(\eta_s^N(x,\sigma) + \eta_s^N(x,-\sigma)\right)\sum_{\sigma\in S}\phi^2\left(\frac{x}{N},\sigma\right)\right) + \mathcal{O}\left(\frac{1}{N^2}\right)
\end{aligned}
$$

Now it is clear that as $N \to \infty$ this goes to 0 in probability. And therefore by the dominated convergence theorem, we see that,

$$
\lim_{N\to\infty}\mathbb{E}\left[\langle M^N\rangle_t\right] = \int_0^t \lim_{N\to\infty}\mathbb{E}[L_N(\pi_s^N(\phi))^2 - 2\pi_s^N(\phi)L_N\pi_s^N(\phi)]ds = 0
$$

And thus the martingale vanished as $N \to \infty$ and we find Equation (3.2) and have,

$$
\langle \pi_t, \phi\rangle = \langle \pi_0, \phi\rangle + \int_0^t \langle \pi_s, (\gamma\phi'' - \lambda\sigma\phi' + \text{flip-adjoint})\rangle ds \tag{3.12}
$$

□

Corollary 3.3. *Furthermore, under the same assumption as theorem 3.2, we define* $m_t := m(\rho_t)$. *Then* m_t *solves the following ordinary differential equation,*

$$\dot{m_t} = c(-1, m_t)(1 - m_t) - c(1, m_t)(1 + m_t) \tag{3.13}$$

In Section 2.3 we introduced the Curie-Weiss Glauber rates, we can show that the partial differential equation from Theorem 3.3 also satisfies the mean-field equation.

Example 3.1. Along the same lines as the proof of Theorem 2.9, we can show that Equation (3.13) abides the mean-field equation if $c(\sigma, m_t)$ follow the Curie-Weiss Glauber rates defined in Equation (2.21). As $t \to \infty$ we will reach equilibrium in which $\dot{m_t} \to 0$, so,

$$0 = e^{\beta m_t}(1 - m_t) - e^{-\beta m_t}(1 + m_t)$$

Rewriting this immediately gives,

$$m_t = \tanh(\beta m_t)$$

3.2 Local magnetization

This section extends the proof for the hydrodynamic limit of Section 3.1 to the case of the local magnetization. While the derivation in Section 3.1 relied on the smoothness of the test functions, the local magnetization will be defined via a discrete indicator function which is discontinuous. Here, we prove that under the hydrodynamic limit, this discrete local magnetization converges to its continuous counterpart. This result justifies the use of the derived PDE for systems with local interactions, as the remainder of the hydrodynamic proof remains identical once this convergence is established. We define the local magnetization to be,

$$m_N(\eta, x) = \langle \pi_t^N * i_\epsilon, \mathbb{1}_{\sigma=1} - \mathbb{1}_{\sigma=-1} \rangle = \frac{1}{2\epsilon N} \sum_{|y-x| \leq \epsilon N} \left(\eta^N_{N^2 t}(y, 1) - \eta^N_{N^2 t}(y, -1) \right) \tag{3.14}$$

where $i_\epsilon = \frac{1}{2\epsilon} \mathbb{1}_{[-\epsilon, \epsilon]}$. The following theorem states that for this non-smooth function we can still find its continuous counterpart.

Theorem 3.4. *As $N \to \infty$ the local magnetization, as defined by Equation (3.14), converges to*

$$m_\epsilon(x, t) = \frac{1}{2\epsilon} \int_{x-\epsilon}^{x+\epsilon} (\rho^+(y, t) - \rho^-(y, t)) dy \tag{3.15}$$

under the hydrodynamic limit. Then, letting $\epsilon \to 0$ gives,

$$m_{loc}(x, t) = \rho^+(x, t) - \rho^-(x, t) \tag{3.16}$$

Proof. The proof of this theorem is sketched below. The hydrodynamic theorem we proved in the previous section shows that $\langle \pi_t^N, \phi \rangle \xrightarrow[N \to \infty]{\mathbb{P}} \langle \rho_t, \phi \rangle$ if $\phi \in C^\infty_{c,S}$. However the test function that fits the local magnetization is not smooth, as

$$\phi_{x,\epsilon}(u, \sigma) = i_\epsilon(u - x)(\mathbb{1}_{\sigma=1} - \mathbb{1}_{\sigma=-1})$$

is discontinuous at the boundaries. To solve this we use the smoothened version of $\phi_{x,\epsilon}(u, \sigma)$ and prove that it converges and its difference with $\phi_{x,\epsilon}(u, \sigma)$ goes to zero. That is, we let J_δ be a standard smooth modifier on the torus and define,

$$\phi^{(\delta)}_{x,\epsilon} := \phi_{x,\epsilon} * J_\delta \in C^\infty_{c,S}$$

Note that $||\phi^{(\delta)}_{x,\epsilon}||_\infty \leq ||\phi_{x,\epsilon}||_\infty = \frac{1}{2\epsilon}$ and $\phi^{(\delta)}_{x,\epsilon} \to \phi_{x,\epsilon}$ uniformly as $\delta \downarrow 0$. This allows us to rewrite $\langle \pi_t^N, \phi \rangle$ as

$$\langle \pi_t^N, \phi_{x,\epsilon} \rangle = \langle \pi_t^N, \phi^{(\delta)}_{x,\epsilon} \rangle + \langle \pi_t^N, \phi_{x,\epsilon} - \phi^{(\delta)}_{x,\epsilon} \rangle$$

As the first section is smooth, $\langle \pi_t^N, \phi^{(\delta)}_{x,\epsilon} \rangle \xrightarrow[N \to \infty]{\mathbb{P}} \langle \rho_t, \phi^{(\delta)}_{x,\epsilon} \rangle$. We now prove the second section goes to zero as $\delta \downarrow 0$, note that for all N,

$$\langle \pi_t^N, \phi_{x,\epsilon} - \phi^{(\delta)}_{x,\epsilon} \rangle \leq ||\phi_{x,\epsilon} - \phi^{(\delta)}_{x,\epsilon}||_\infty \langle \pi_t^N, 1 \rangle$$

Since $\langle \pi_t^N, 1 \rangle$ equals the average density, which is constant in time, we have,

$$\langle \pi_t^N, 1 \rangle = \int_0^1 (\rho_0^+ + \rho_0^-)(u) du =: M < \infty$$

Therefore,

$$\sup_N |\langle \pi_t^N, \phi_{x,\epsilon} - \phi^{(\delta)}_{x,\epsilon} \rangle| \leq M ||\phi_{x,\epsilon} - \phi^{(\delta)}_{x,\epsilon}||_\infty \xrightarrow[\delta \downarrow 0]{} 0$$

and thus we have,

$$\langle \pi_t^N, \phi_{x,\epsilon} \rangle \xrightarrow[N \to \infty]{\mathbb{P}} \langle \rho_t, \phi^{(\delta)}_{x,\epsilon} \rangle \xrightarrow[\delta \downarrow 0]{} \langle \rho_t, \phi_{x,\epsilon} \rangle$$

because $\rho_t \in C_{\mathbb{T},S}$ and $\phi^{(\delta)}_{x,\epsilon} \to \phi_{x,\epsilon}$ uniformly. We can now explicitly compute the magnetization,

$$\begin{aligned}\langle \rho_t, \phi_{x,\epsilon} \rangle &= \sum_{\sigma=\pm 1} \int_0^1 \rho^\sigma(y,t) i_\epsilon(y-x)(\mathbb{1}_{\sigma=1} - \mathbb{1}_{\sigma=-1}) dy \\ &= \frac{1}{2\epsilon} \int_{x-\epsilon}^{x+\epsilon} (\rho^+(y,t) - \rho^-(y,t)) dy\end{aligned}$$

Furthermore, as $\epsilon \to 0$,

$$m_{loc}(x,t) = \rho^+(x,t) - \rho^-(x,t)$$

Thus proving the theorem □

Note that as this theorem is proven, the rest of the proof given in section 3.1 remains identical as only the convergence of m_N to m was needed. Therefore, under the local magnetization, the system converges to the following PDE,

$$\dot{\rho_t}(x,\sigma) = \gamma \Delta \rho_t(x,\sigma) - \sigma\lambda \partial_x \rho_t(x,\sigma) + c(-\sigma, m(\rho_t))\rho_t(x,-\sigma) - c(\sigma, m(\rho_t))\rho_t(x,\sigma)$$

4 Perturbative, Fourier-Laplace and weakly nonlinear analysis of the hydrodynamic limit for different rates c

The following section focuses on analyzing the partial differential equation derived in Theorem 3.2, i.e., the PDE derived by taking the hydrodynamic limit of generator defined in Section 3.

$$\dot{\rho_t}(x,\sigma) = \gamma\Delta\rho_t(x,\sigma) - \sigma\lambda\partial_x\rho_t(x,\sigma) + c(-\sigma, m(\rho_t))\rho_t(x,-\sigma) - c(\sigma, m(\rho_t))\rho_t(x,\sigma)$$

with initial condition $\rho_0(x,\sigma) = \rho(x,\sigma)$. As the analysis of the PDE varies heavily depends on the rates $c(\sigma, m)$, the analysis will be done for three different rates. These rates are the constant, the linear and the Curie-Weiss Glauber rates, which will all be discussed in a separate subsection (4.1-4.3). For all these rates we will study their long term behavior. We will study their long-term behavior. And for the Curie-Weiss Glauber rates we will also analyze how the system behaves under the local magnetization. This is done in Section 4.4. During this section the following definition of the Fourier transform is used,

$$\hat{f}_q(t) = \int_X f(x,t)e^{-iqx}dx, \qquad f(x,t) = \mathcal{F}^{-1}[\hat{f}_q(t)](x) \tag{4.1}$$

As the derivation of the hydrodynamic limit was valid for both the infinite domain $X = \mathbb{R}$ that was compactly supported or the periodic domain $X = [0,1]$, the inverse Fourier has different forms in each. For the infinite and periodic domain respectively we have,

$$f(x,t) := \frac{1}{2\pi}\int_{-\infty}^{\infty}\hat{f}(q)e^{iqx}dq \qquad f(x,t) := \sum_{q/2\pi\in\mathbb{Z}}\hat{f}_q(t)e^{iqx} \tag{4.2}$$

Note that we have taken $q/2\pi \in \mathbb{Z}$ as we have $q := 2\pi k$. Importantly, under the Fourier transform one has $\partial_x \mapsto iq$ and $\Delta \mapsto -q^2$. The Laplace transform of the previously defined Fourier transform is defined as below. Note that under the Laplace transform $\mathcal{L}(\partial_t\hat{f}) = z\bar{f}(z) - \hat{f}(0)$.

$$\bar{f}_q(z) = \mathcal{L}\{\hat{f}_q(t)\}(z) := \int_0^{\infty} e^{-zt}\hat{f}_q(t)dt, \quad \hat{f}_q(t) = \mathcal{L}^{-1}\{\bar{f}_q\}(t) := \frac{1}{2\pi i}\int_{\sigma_0-i\infty}^{\sigma_0+i\infty} e^{qt}\bar{f}_q(z)dz \tag{4.3}$$

All the derivations will follow similar procedure which we we introduce briefly. In order to study the long-term behavior of the systems we aim to find the effective velocity and diffusion coefficient that were introduced in Section 2.6 on Brownian motion. To do this we linearize the PDEs and then take the Fourier-Laplace transform to find the structure function which is invariant under scaling and from which we can immediately see the effective transport coefficient. We will now find this structure function for simple Brownian motion, so that they can easily be compared. Simple Brownian motion starting from $\rho(x,0) = \delta(x)$ has the following PDE,

$$\partial_t\rho = D\partial_x^2\rho$$

given by Equation (2.36). Taking the Fourier-Laplace transform then yields the following structure function,

$$S(q,z) = \int \rho(x,t)e^{-iqx}e^{-zt}dxdt = \frac{1}{z+Dq^2} \tag{4.4}$$

We worked under scaling $x \to x/\epsilon$ and $t \to t/\epsilon^2$ (where $\epsilon = 1/N$). In the Fourier-Laplace domain, this corresponds to scaling the wavenumber with $q \to \epsilon q$ and the frequency with $z \to \epsilon^2 z$. One can therefore see that this $S(q,z)$ satisfies the scaling behavior $\epsilon^2 S(\epsilon q, \epsilon^2 z) = S(q,z)$ and thus that Brownian motion is invariant under scaling. Therefore if for a certain model it is the case that

$$\lim_{\epsilon\to 0}\epsilon^2 S(\epsilon q, \epsilon^2 q) = \frac{1}{z+Dq^2} \tag{4.5}$$

this model has diffusive scaling behavior with diffusion constant D. We can do similar derivation for Brownian motion with drift given by,

$$\partial_t\rho = -\partial_x(v\rho) + \partial_x^2(D\rho)$$

Then we say that if for a certain model it is the case that,

$$\lim_{\epsilon \to 0} \epsilon^2 S(\epsilon q, \epsilon^2 q) = \frac{1}{z + iqv + Dq^2} \tag{4.6}$$

this model has diffusive scaling behavior with diffusion constant D and drift velocity v,

4.1 Analysis for constant rates

We start by analyzing the PDE for the easiest rates, that is the constant rates $c(\sigma, m) = c_0$. To rigorously understand the long-term behavior of this system we analyze the convergence of the characteristic function under hydrodynamic scaling. We calculate the Fourier-Laplace transform of the density and apply the diffusive scaling limit $\epsilon := 1/N \to 0$ to find the global transport coefficients of this system. To simplify calculations and notation, we define,

$$\begin{cases} \rho_+(x,t) := \rho_t(x, \sigma = +1), \\ \rho_-(x,t) := \rho_t(x, \sigma = -1) \end{cases} \tag{4.7}$$

With the initial condition $\rho_\pm(x,0) = \rho_0(x, \sigma = \pm 1) = \rho(x, \pm\sigma)$. Using this definition we can split the PDE of Equation (3.2) up into two PDEs for $\sigma = +1$ and $\sigma = -1$,

$$\begin{cases} \partial_t \rho_+ = \gamma \Delta \rho_+ - \lambda \partial_x \rho_+ + c(-1)\rho_- - c(+1)\rho_+, \\ \partial_t \rho_- = \gamma \Delta \rho_- + \lambda \partial_x \rho_- + c(+1)\rho_+ - c(-1)\rho_- \end{cases} \tag{4.8}$$

We define the local density and local magnetization as follows,

$$\begin{cases} \rho(x,t) := \rho_+(x,t) + \rho_-(x,t), \\ s(x,t) := \rho_+(x,t) - \rho_-(x,t) \end{cases} \tag{4.9}$$

With the initial conditions $\rho(x,0) = \rho_+(x,0) + \rho_-(x,0)$ and $s(x,0) = \rho_+(x,0) - \rho_-(x,0)$. This allows us to write Equation (4.8) in terms of the density and magnetization, that is,

$$\begin{cases} \partial_t \rho = \gamma \Delta \rho - \lambda \partial_x s, \\ \partial_t s = \gamma \Delta s - \lambda \partial_x s - 2c_0 s \end{cases} \tag{4.10}$$

This equation is considerably easier to analyze. We aim to find one equation in the Fourier-Laplace field that describes this entire system. To start we take the Fourier transform,

$$\begin{cases} \partial_t \hat{\rho} = -\gamma q^2 \hat{\rho} - i\lambda q \hat{s}, \\ \partial_t \hat{s} = -\gamma q^2 \hat{s} - i\lambda q \hat{s} - 2c_0 \hat{s} \end{cases} \tag{4.11}$$

However, as we still have the time-derivatives we must additionally take the Laplace-transform, this yields,

$$\begin{cases} z\bar{\rho} - \hat{\rho}(0) = -\gamma q^2 \bar{\rho} - i\lambda q \bar{s}, \\ z\bar{s} - \hat{s}(0) = -\gamma q^2 \bar{s} - i\lambda q \bar{s} - 2c_0 \bar{s} \end{cases} \tag{4.12}$$

As we consider system with a normalized density with $\rho(x,0) = \delta(x)$ and with no initial spin excess, we can without loss of generality assume that $\hat{\rho}(0) = 1$ and $\hat{s}(0) = 0$. The second Equation (4.12) allows us to express the fast mode $\bar{s}$ entirely in terms of the slow mode $\bar{\rho}$. This is known as adiabatic elimination, here applicable as the spin variable relaxes at a rate $2c_0$ while the density is conserved. This gives,

$$\bar{s} = \frac{i\lambda q}{z + \gamma q^2 + 2c_0} \bar{\rho}$$

Substituting this equation back into the first equation of Equation (4.12) yields a closed form for the density propagator $\bar{\rho}(q,z)$,

$$\bar{\rho} = \frac{1}{z + \gamma q^2 + \frac{\lambda^2 q^2}{z + \gamma q^2 + 2c_0}} \tag{4.13}$$

To retrieve the macroscopic behavior, we apply the diffusive scaling of space and time introduced in Section 2.4. That is, $x \to x/\epsilon$ and $t \to t/\epsilon^2$ (where $\epsilon = 1/N$). In the Fourier-Laplace domain, this corresponds to scaling the wavenumber with $q \to \epsilon q$ and the frequency with $z \to \epsilon^2 z$. We define the scaled structure function $S(q, z)$ as,

$$S(q, z) := \lim_{\epsilon \to 0} \epsilon^2 \bar{\rho}(\epsilon q, \epsilon^2 z)$$

Substituting the scaled variables into Equation (4.13) and dividing the numerator and denominator by ϵ^2 we obtain,

$$S_\epsilon(q, z) = \lim_{\epsilon \to 0} \frac{\epsilon^2}{\epsilon^2 z + \gamma \epsilon^2 q^2 + \frac{\lambda^2 \epsilon^2 q^2}{\epsilon^2 z + \gamma \epsilon^2 q^2 + 2c_0}} = \lim_{\epsilon \to 0} \frac{1}{z + \gamma q^2 + \frac{\lambda^2 q^2}{2c_0 + \epsilon^2 (z + \gamma q^2)}} = \frac{1}{z + \left(\gamma + \frac{\lambda^2}{2c_0}\right) q^2}$$

Taking the limit $\epsilon \to 0$, the term $\epsilon^2(z + \gamma q^2)$ in the denominator vanishes. Then, the structure function converges to,

$$S_{macro}(q, z) = \frac{1}{z + \left(\gamma + \frac{\lambda^2}{2c_0}\right) q^2} \tag{4.14}$$

This limiting form matches the propagator for a standard diffusion model equation $\partial_t \rho = D \partial_x^2 \rho$ as given in Section 2.6. We can this directly identify the effective transport coefficient from the poles of this function. Since there is no term linear in iq in the denominator, the effective velocity is zero. The coefficient of the q^2 term yields the effective diffusion coefficient, and thus,

$$v_{eff} = 0 \quad \text{and} \quad D_{eff} = \gamma + \frac{\lambda^2}{2c_0} \qquad \text{when} \qquad c(\sigma, m) = c_0 \tag{4.15}$$

Thus, our models large and long-term behavior can be approximated by the following advection-diffusion PDE,

$$\partial_t \rho = \left(\gamma + \frac{\lambda^2}{2c_0}\right) \partial_x^2 \rho \tag{4.16}$$

This derivation demonstrated that the effective diffusion is composed of the passive Brownian diffusion γ and an active enhancement $\lambda^2/2c_0$. The active term is inversely proportional to the flipping rate $2c_0$, showing that rapid direction switching suppresses the persistent active motion, reducing it to a diffusive process at large scales.

4.1.1 Inversion of the scaling limit and the emergence of Gaussian behavior

Having established that the scaled structure function converges to $S_{macro}(q, z) = \left(z + D_{eff} q^2\right)^{-1}$ in the hydrodynamic limit, we can now invert this process to recover the probability density function in real space and time. In this section we do this on the infinite domain, Section 4.3.3 does this for both domains. This inversion is done to provide a concrete physical interpretation of the effective diffusion constant derived in the previous section. To retrieve the time-domain evolution, we first preform the inverse Laplace transform,

$$\hat{\rho}_{macro}(q, t) = \mathcal{L}^{-1}\left\{\frac{1}{z + D_{eff} q^2}\right\} = e^{-D_{eff} q^2 t} \hat{\rho}(q, 0) \tag{4.17}$$

Assuming one particle starts a the origin we have $\hat{\rho}(q, 0) = 1$. To find the spatial distribution $\rho(x, t)$, we apply the inverse Fourier transform on the infinite domain,

$$\rho(x, t) = \mathcal{F}^{-1}\left\{e^{-D_{eff} q^2 t}\right\} = \frac{1}{\sqrt{4\pi D_{eff} t}} \exp\left(-\frac{x^2}{4 D_{eff} t}\right) \tag{4.18}$$

This result confirms that, under the constant rates, the complex interplay of active transport and random switching homogenizes into a standard Gaussian packet. The active part of the particles does not generate a net drift velocity but instead results in an enhanced diffusion coefficient. Note that this is the exact same solution as the probability density function for simple Brownian motion given by Equation (2.37).

4.2 Analysis for linear rates

In this section we expand our horizon to a more complex rate, the linear rate $c = c_0 - \sigma\beta m$, where β is small such that $c > 0$. Note that this is the first order expansion of the Curie-Weiss Glauber rates $e^{-\sigma\beta m}$ when taking $c_0 = 1$. As in the previous section, we split up the PDE so consider the different magnetization states. Then take the Fourier-Laplace transform over the PDE linearized around its steady state to better understand these rates. To simplify calculations we assume that the total mass is normalized, that is $\int_0^1 \rho(x,t) = 1$. This allows us, without loss of generality, to simplify the total magnetization to,

$$m = \frac{\int_0^1 (\rho_+(x,t) - \rho_-(x,t))dx}{\int_0^1 (\rho_+(x,t) + \rho_-(x,t))dx} = \int_0^1 s(x,t)dx \tag{4.19}$$

By adding and subtraction both equations found in Equation (4.8), we find that for ρ and s we have,

$$\begin{cases} \partial_t \rho = \gamma\Delta\rho - \lambda\partial_x s, \\ \partial_t s = \gamma\Delta s - \lambda\partial_x \rho + 2(c(-1,m)\rho_- - c(1,m)\rho_+) \end{cases}$$

The second line can be simplified further by using $\rho_\pm = (\rho \pm s)/2$ to give the final form

$$\begin{cases} \partial_t \rho = \gamma\Delta\rho - \lambda\partial_x s, \\ \partial_t s = \gamma\Delta s - \lambda\partial_x \rho - 2c_0 s + 2\beta\rho m \end{cases} \tag{4.20}$$

4.2.1 Linearization around the steady state

In order to analyze this equation, and particularly its long-term behavior, we linearize it around its steady state $s \equiv 0$. Here we have $\rho \equiv \rho_0 = 1$ by assumption. We now assume that around this steady state we have small perturbations (indexed with $\tilde{\cdot}$). That is, $\rho(x,t) = \rho_0 + \tilde{\rho}(x,t)$, $s(x,t) = 0 + \tilde{s}(x,t)$ and $m(x,t) = \tilde{m}(x,t)$. Substituting this into Equation (4.22) and getting rid of smaller order terms (such as $\tilde{\rho}(x,t)$ and $\tilde{m}(t)$), gives,

$$\begin{cases} \partial_t \tilde{\rho} = \gamma\Delta\tilde{\rho} - \lambda\partial_x \tilde{s}, \\ \partial_t \tilde{s} = \gamma\Delta\tilde{s} - \lambda\partial_x \tilde{\rho} - 2c_0\tilde{s} + 2\beta\rho_0\tilde{m} \end{cases} \tag{4.21}$$

We can take the Fourier transform. Note that be definition of the Fourier transform $\tilde{m} = \hat{s}_0(t)$, this allows us to write the Fourier transformed as,

$$\begin{cases} \partial_t \hat{\rho} = -\gamma q^2\hat{\rho} - i\lambda q\hat{s}, \\ \partial_t \hat{s} = -\gamma q^2\hat{s} - i\lambda q\hat{\rho} - 2c_0\hat{s} + 2\beta\rho_0\hat{s}_0\delta_{q,0} \end{cases} \tag{4.22}$$

Where $\delta_{q,0}$ is the Dirac delta function. This differential equation exhibits different behavior for $q \neq 0$ and $q = 0$. These cases will therefore be studied separately. Note that for $q \neq 0$ we find the exact same case as for the constant rates, that is Equation (4.11). Therefore, the higher-order modes of the Fourier transformed exhibit the same behavior as in the case of constant rates, and thus we will find that the global transport coefficients are given by Equation (4.15). While the zero-order mode, i.e. the total magnetization, may differ. In the case of $q = 0$, the equation simplifies to,

$$\begin{cases} \partial_t \hat{\rho}_0 = 0, \\ \partial_t \hat{s}_0 = -2c_0\hat{s}_0 + 2\beta\rho_0\hat{s}_0 \end{cases} \tag{4.23}$$

Therefore the magnetization we find the following equation, which can be solved immediately,

$$\partial_t m(t) = -2(c_0 - \beta\rho_0)m(t) \qquad \Rightarrow \qquad m(t) = m(0)e^{2(c_0-\beta\rho_0)t} \tag{4.24}$$

Therefore, as β is chosen to be smaller than c_0/ρ_0 the global magnetization decays to $m = 0$, while as $\beta \geq c_0/\rho_0$ the magnetization grows towards $m = \pm 1$.

4.3 Analysis for Curie-Weiss Glauber rates

In this section we consider the final, and most complex rates: the Curie-Weiss Glauber rates $c(\sigma, m) = e^{-\beta\sigma m}$. We split the PDE and linearize around the steady state before we do a Fourier-Laplace analysis. We use this to find the global transport coefficients and find solutions for the local density $\rho(x,t)$. Lastly, we apply a weakly nonlinear analysis to get a quantitative idea about the nonlinear behavior. We split the PDE using $\rho(x,t) := \rho_+(x,t) + \rho_-(x,t)$ and $s(x,t) := \rho_+(x,t) - \rho_(x,t)$. Similarly as in the case of linear rates, we find that the PDE may be written as,

$$\begin{cases} \partial_t \rho = \gamma \Delta \rho - \lambda \partial_x s, \\ \partial_t s = \gamma \Delta s - \lambda \partial_x \rho - 2\cosh(\beta m) s + 2\sinh(\beta m)\rho \end{cases} \tag{4.25}$$

4.3.1 Linearization around the steady state

We linearize the equation around its steady state $m(t) \equiv s_0/\rho_0$ where s_0/ρ_0 solves $m_0 = \tanh(\beta m_0)$. At this steady state we have $\rho(x,t) \equiv \rho_0$ and $s(x,t) \equiv s_0$. Assume that around this state we have small perturbations, i.e., $\rho(x,t) = \rho_0 + \tilde{\rho}(x,t)$, $s(x,t) = s_0 + \tilde{s}(x,t)$ and $m(t) = m_0 + \tilde{m}(t)$. We will show that under these assumptions we have,

$$\begin{cases} \partial_t \tilde{\rho} = \gamma \Delta \tilde{\rho} - \lambda \partial_x \tilde{s}, \\ \partial_t \tilde{s} = \gamma \Delta \tilde{s} - \lambda \partial_x \tilde{\rho} + 2S\tilde{\rho} - 2C\tilde{s} + K\tilde{m} \end{cases} \tag{4.26}$$

Where $C := \cosh(\beta m_0), S := \sinh(\beta m_0)$ and $K = 2\beta\rho_0/C$. To show these equalities, we must use the following approximations,

$$\sinh(x+\delta x) \approx \sinh(x) + \cosh(x)\delta x \qquad \cosh(x+\delta x) \approx \cosh(x) + \sinh(x)\delta x$$

One can easily see that this is true by looking that definition of the derivative. Using this we can approximate the hyperbolic functions by getting rid of higher-order terms,

$$2\sinh(\beta m)\rho \approx 2(S + \beta C\tilde{m})(\rho_0 + \tilde{\rho}) \approx 2S\rho_0 + 2S\tilde{\rho} + 2\beta C\rho_0\tilde{m}$$

$$-2\cosh(\beta m)s \approx -2Cs_0 - 2C\tilde{s} - 2\beta S m_0 \tilde{m}$$

This allows us to find the final simplified form, that is,

$$2\sinh(\beta m)\rho - 2\cosh(\beta m)s \approx 2S\tilde{\rho} - 2C\tilde{s} + (2\beta C\rho_0 - 2\beta S m_0)\tilde{m} = 2S\tilde{\rho} - 2C\tilde{s} + K\tilde{m}$$

Now we have found the version seen in Equation (4.26), only the variable K does not match yet. Using $m_0 = S/C$ and the known identity $\cosh^2(x) - \sinh^2(x) = 1$ we can write K as,

$$K = 2\beta C\rho_0 - 2\beta S m_0 = 2\beta C\rho_0 - 2\beta\frac{\rho_0 S^2}{C} = 2\beta\rho_0\left(\frac{C^2 - S^2}{C}\right) = \frac{2\beta\rho_0}{C}$$

4.3.2 Fourier-Laplace analysis with Curie-Weiss Glauber rates

To determine the global transport coefficients for the Curie-Weiss rates, we employ the same Fourier-Laplace analysis as has been done in Section 4.1 and Section 4.2. However, unlike the constant rate case, the coupling between the spin relaxation and the active drift is more complex. Starting from the linearized equations we may take the Fourier transform to find,

$$\begin{cases} \partial_t \hat{\rho} = -\gamma q^2 \hat{\rho} - i\lambda q \hat{s}, \\ \partial_t \hat{s} = -\gamma q^2 \hat{s} - i\lambda q \hat{\rho} + 2S\hat{\rho} - 2C\hat{s} + K\tilde{m}\delta_{q,0} \end{cases} \tag{4.27}$$

$\mathbf{q \neq 0}$: Note that the forcing term is only present for $q = 0$. Therefore we will treat these two cases separately. We start with the $q \neq 0$ case as this allows for the analysis of the global transport

coefficients. As the global forcing term $K\tilde{m}$ is not present we can find Laplace transform with initial conditions $\hat{\rho}(0) = 1$ and $\hat{s}(0) = 0$, which is given by,

$$\begin{cases} z\bar{\rho} - 1 = -\gamma q^2 \bar{\rho} - i\lambda q \bar{s}, \\ z\bar{s} = -\gamma q^2 \bar{s} - i\lambda q \bar{\rho} + 2S\bar{\rho} - 2C\bar{s} \end{cases} \tag{4.28}$$

The spin variable $\bar{s}$ is the fast mode, relaxing at a rate proportional to $2C$. We adiabatically eliminate it by solving the second equation for $\bar{s}$ in terms of $\bar{\rho}$,

$$\bar{s} = \frac{2S - i\lambda q}{2C + z + \gamma q^2}\bar{\rho}$$

Substituting this back into the density equation allows us to find a closed form density propagator $\bar{\rho}(q, z)$,

$$\bar{\rho}(q, z) = \frac{1}{z + \gamma q^2 + \frac{i\lambda q(2S - i\lambda q)}{2C + z + \gamma q^2}} \tag{4.29}$$

To identify the transport coefficients, we look for the poles of this function in the hydrodynamic limit. We expect a drift v_{eff} and diffusion D_{eff}, meaning the z will be of the form $z = -iv_{eff}q - D_{eff}q^2$ up to the second order of q. We expand the denominator term around this drift. Assuming $|z| \ll 2C$ (the adiabatic approximation), we can approximate the fraction in the denominator,

$$\frac{1}{2C + z + \gamma q^2} \approx \frac{1}{2C - iv_{eff}q} \approx \frac{1}{2C}\left(1 - \frac{iv_{eff}q}{2C}\right)$$

Substituting this expansion into Equation (4.29) and collecting terms by order of q:

$$\bar{\rho}(q, z) = \frac{1}{z + \gamma q^2 + i\lambda q(2S - i\lambda q)\frac{1}{2C}\left(1 - \frac{iv_{eff}q}{2C}\right)} = \frac{1}{z + \frac{2i\lambda S}{2C}q + \gamma q^2 + \frac{\lambda^2 q^2}{2C} - \frac{2i\lambda S q^2}{2C}\left(\frac{iv_{eff}}{2C}\right) + \mathcal{O}\left(q^3\right)} \tag{4.30}$$

We can now identify the global transport coefficients form the terms linear and quadratic in q in the denominator. The linear term iq gives the effective velocity. From the expansion, we have $\frac{2i\lambda S}{2C}q$. Thus,

$$v_{eff}q = \frac{2\lambda S}{2C}q \Rightarrow v_{eff} = \lambda\frac{S}{C} = \lambda\tanh(\beta m_0) = \lambda m_0$$

Substituting the result for v_{eff} back into Equation (4.30) allows us to find the diffusion coefficient,

$$\bar{\rho}(q, z) = \frac{1}{z + imq + \gamma q^2 + \frac{\lambda^2}{2C}\left(1 - \frac{S^2}{C^2}\right)q^2} = \frac{1}{z + imq + \left(\gamma + \frac{\lambda^2}{2C^3}\right)q^2} \tag{4.31}$$

In conclusion we have the following global transport coefficients,

$$v_{eff} = \lambda\tanh\left(\beta m_0\right) \quad \text{and} \quad D_{eff} = \gamma + \frac{\lambda^2}{2\cosh^3(\beta m_0)} \qquad \text{when} \quad c(\sigma, m) = e^{-\sigma\beta m} \tag{4.32}$$

Which can also be written in terms of only m_0 using the mean-field equation $m_0 = \tanh(\beta m_0)$,

$$v_{eff} = \lambda m_0 \quad \text{and} \quad D_{eff} = \gamma + \frac{\lambda^2}{2}\left(1 - m_0^2\right)^{3/2} \tag{4.33}$$

We can formally verify this result by applying the hydrodynamic scaling limit in a co-moving frame. We define the scaled propagator shifted by the drift velocity as $S_\epsilon(q, z) = \lim_{\epsilon\to 0}\epsilon^2\bar{\rho}(\epsilon q, \epsilon^2 z - iv\epsilon q)$. Substituting expression 4.31 into the limit gives

$$S_\epsilon(q, z) = \lim_{\epsilon\to 0}\epsilon^2\bar{\rho}(\epsilon q, \epsilon^2 z - iv\epsilon q) = \lim_{\epsilon\to 0}\epsilon^2\frac{1}{\epsilon^2 z - im_0\epsilon q + im_0\epsilon q + \left(\gamma + \frac{\lambda^2}{2C^3}\right)\epsilon^2 q^2}$$

Taking the limit indeed shows us that we have found the correct global transport coefficients,

$$S_{macro}(q, z) = \frac{1}{z + \left(\gamma + \frac{\lambda^2}{2C^3}\right)q^2} \tag{4.34}$$

Remark 4.1. By similar reasoning as in Equation (4.16) v_{eff} and D_{eff} can again be used to approximate our model by an advection-diffusion PDE following the theory presented in Section 2.6. That is,

$$\partial_t \rho + \lambda \tanh(\beta m_0) \partial_x \rho = \left(\gamma + \frac{\lambda^2}{2\cosh^3(\beta m_0)} \right) \partial_x^2 \rho \tag{4.35}$$

Remark 4.2. Note that as $m_0 \to 0$, we have that $\tanh(\beta m_0) \to 0$ and $\cosh(\beta m_0) \to 1$. Therefore one finds that the global transport coefficients are given by,

$$v_{eff} = 0 \quad \text{and} \quad D_{eff} = \gamma + \frac{\lambda^2}{2}$$

which is indeed equal to the global transport coefficients when the rates $c(\sigma, m)$ are chosen to be constant. Here no drift velocity is present as the magnetization converges to zero.

Remark 4.3. Note that as $m_0 \to \pm 1$, we have that $\tanh(\beta m_0) \to \pm 1$. Therefore one finds that the global transport coefficients are given by,

$$v_{eff} = \pm\lambda \quad \text{and} \quad D_{eff} = \gamma$$

This shows us that, under $m_0 \to \pm 1$, the active movement of the particles leads to an active drift instead of an increased diffusion coefficients. This is the case as the internal states, and thus the direction of the particles, is aligned.

$\mathbf{q = 0}$: We now consider the case where $q = 0$. Here Equation (4.27) reduces to

$$\begin{cases} \partial_t \hat{\rho}_0 = 0, \\ \partial_t \hat{s}_0 = 2S\hat{\rho}_0 - 2C\hat{s}_0 + K\tilde{m}(t) \end{cases} \tag{4.36}$$

Now, we determine the Laplace transform of these two equations to get a better understanding of their behavior. The first equation can be solved directly, giving $\bar{\rho}_0(z) = \rho_0(0)/z$. However, for the second equation we must first simplify $\tilde{m}(t)$,

$$m(t) = \frac{\int_0^1 s(x,t)dx}{\int_0^1 \rho(x,t)dx} \approx \frac{s_0 + \hat{s}_0}{\rho_0 + \hat{\rho}_0} \approx \frac{s_0}{\rho_0} + \frac{\hat{s}_0}{\rho_0} - \frac{s_0}{\rho_0}\frac{\hat{\rho}_0}{\rho_0} \Rightarrow \tilde{m}(t) = \frac{\rho_0 \hat{s}_0 - s_0 \hat{\rho}_0}{\rho_0^2} \tag{4.37}$$

We can substitute this into the Equation (4.36) and rearrange to find,

$$\partial_t \hat{s}_0 = -\Gamma \hat{s}_0 + \Lambda \hat{\rho}_0 \qquad \text{where} \qquad \Gamma = 2\left(C - \frac{\beta}{C}\right), \quad \Lambda = 2S\left(1 - \frac{\beta}{C^2}\right) \tag{4.38}$$

We can now take the Laplace transform as use $\tilde{\rho}_0(s) = \rho_0(0)/z$ to find that $\bar{s}_0(z)$ is given by,

$$\bar{s}_0(z) = \frac{\hat{s}_0(0)}{z + \Gamma} + \frac{\Lambda \hat{\rho}_0(0)}{z(z + \Gamma)} \tag{4.39}$$

From this equation we immediately see that the poles are located at $z = 0$ and $z = -\Gamma = -2\left(C - \frac{\beta}{C}\right)$. This first pole corresponds to the constant time-independent mass conservation of $\tilde{\rho}(x,t)$. The pole at $s = -\Gamma$ describes the exponential term that decays as $\Gamma > 0$ and grows as $\Gamma < 0$, in which case it would be linearly unstable. However by looking at Γ we see that $\Gamma > 0$ for $\beta \neq 1$, whereas $\Gamma = 0$ for $\beta = 1$. This shows us that $\beta = 1$ is indeed an unstable state. Using this can take the inverse Laplace transform to find that $\hat{s}_0(t)$ changes with,

$$\hat{s}_0(t) = \left(\hat{s}_0(0) - \frac{\Lambda}{\Gamma}\hat{\rho}_0(0) \right) e^{-\Gamma t} + \frac{\Lambda}{\Gamma}\hat{\rho}_0(0) \tag{4.40}$$

Remark 4.4. We can show that under the assumption $\Gamma > 0$ Equation (4.40) satisfies the mean-field equation. To do this, substitute Equation (4.40) into Equation (4.37) that we found for $\tilde{m}(t)$. Let $t \to \infty$,

$$\lim_{t\to\infty} \tilde{m}(t) = \frac{1}{\rho_0}\frac{\Lambda \hat{\rho}_0(0)}{\Gamma} - \frac{s_0 \hat{\rho}_0(t)}{\rho_0^2}$$

Note that since the total density is conserved $\hat{\rho}_0(t) = \hat{\rho}_0(0)$. Therefore as $\lim_{t\to\infty} \tilde{m}(t) = 0$ by substituting Γ and Λ found in Equation (4.38), one finds,

$$\frac{\Lambda}{\Gamma} = \frac{s_0}{\rho_0} \Rightarrow m_0 = \tanh(\beta m_0) \qquad \text{as} \qquad t \to \infty \tag{4.41}$$

4.3.3 Solution of the problem in the real domain

Having determined the macroscopic structure function $S_{macro}(q, z)$ in Section 4.3.2, we now invert the scaling limit to recover the probability density $\rho(x, t)$ in real space and time. This provides a physical interpretation of the derived transport coefficients v_{eff} and D_{eff}. Recall from Equation (4.31) that the density propagator in the Fourier-Laplace domain converges to,

$$\bar{\rho}_{macro}(q, z) = \frac{1}{z + iv_{eff}q + D_{eff}q^2}$$

where the coefficients are given by Equation (4.32) as $v_{eff} = \lambda \tanh(\beta m_0)$ and $D_{eff} = \gamma + \frac{\lambda^2}{2\cosh^3(\beta m_0)}$. Note that is propagator is directly recognized as the propagator for the standard advection-diffusion equation introduced in Section 2.6. We now show that under our boundary and initial conditions we indeed get similar real space and time solutions for $\rho(x, t)$. We first perform the inverse Laplace transform to recover the time-evolution of the spatial modes. Using the standard transform $\mathcal{L}^{-1}\{(z + a)^{-1}\} = e^{-at}$, we find the Fourier propagator $\hat{\rho}(q, t)$ to be

$$\hat{\rho}(q, t) = \mathcal{L}^{-1}\left\{\frac{1}{z + (iv_{eff}q + D_{eff}q^2)}\right\} = \exp\left(-\left(iv_{eff}q + D_{eff}q^2\right)t\right)\hat{\rho}(q, 0) \tag{4.42}$$

This expression describes the evolution of a Fourier mode q. That is, it oscillates with frequency $\omega = -v_{eff}q$ (the drift) and decays with rate $D_{eff}q^2$ (the diffusion). The form of the final density profile $\rho(x, t)$ depends on the choice of spatial domain and boundary conditions. We consider both the infinite line and the periodic torus as the hydrodynamic limit works for both these conditions.

For a system on the infinite line, the inverse Fourier transform was given by the integral $\rho(x, t) = \frac{1}{2\pi}\int_{-\infty}^{\infty} \hat{\rho}(q, t)e^{iqx}dq$. Substituting the propagator derived above gives,

$$\rho(x, t) = \frac{1}{2\pi}\int_{-\infty}^{\infty} \hat{\rho}(q, 0)e^{-D_{eff}q^2 t}e^{iq(x - v_{eff}t)}dq \tag{4.43}$$

Assuming a Dirac delta initial condition $\rho(x, 0) = \delta(x)$, we have $\hat{\rho}(q, 0) = 1$. The integral becomes a standard Gaussian integral,

$$\rho(x, t) = \frac{1}{\sqrt{4\pi D_{eff}t}} \exp\left(-\frac{(x - v_{eff}t)^2}{4D_{eff}t}\right) \tag{4.44}$$

This result shows that the interplay of active transport and Curie-Weiss switching homogenizes into a fundamental Gaussian solution drifting at velocity v_{eff} where the diffusion coefficient also depends on the choice of β. Note that is this the same as solution to the Fokker-Planck equation given in Section 2.6.3.

For the finite domain with periodic boundary conditions used in our hydrodynamic derivation, the wavenumbers are discrete for $q/2\pi \in \mathbb{Z}$. The inverse transform was defined by the series summation and thus gives

$$\rho(x, t) = \sum_{q/2\pi\in\mathbb{Z}} \hat{\rho}_q(t)e^{iqx} = \sum_{q/2\pi\in\mathbb{Z}} \hat{\rho}_q(0)e^{-D_{eff}q^2 t}e^{iq(x - v_{eff}t)} \tag{4.45}$$

Taking the inverse Fourier-transform of this function is a bit more complex and requires us to use the periodic Green function. That is, define the periodic Green's function $G_{per}(x, t)$ by

$$G_{per}(x, t) = \sum_{q/2\pi\in\mathbb{Z}} \widehat{G_{per}}_q(t)e^{iqx} \qquad \text{where} \qquad \widehat{G_{per}}_q(t) = e^{-q^2 Dt}e^{-iqvt} \tag{4.46}$$

This allows to write $\rho(x,t)$ as a convolution of ρ_0 and $G_{per}(x,t)$, i.e.,

$$\rho(x,t) = \sum_{q/2\pi\in\mathbb{Z}} \hat{\rho}_q(0) e^{iq(x-vt)-Dq^2t} = \sum_{q/2\pi\in\mathbb{Z}} \hat{\rho}_q(0) e^{-q^2Dt} e^{iq(x-vt)} = \sum_{q/2\pi\in\mathbb{Z}} \hat{\rho}_q(0) \widehat{G_{per}}_q(t) e^{iqx}$$
$$= (\rho_0(\cdot) * G_{per}(\cdot,t))(x) = \int_0^1 G_{per}(x-y,t)\rho_0(y)dy$$

To express $G_{per}(x,t)$ without the use of the Fourier transform we must use the Poisson summation formula which is given by,

$$\sum_{q/2\pi\in\mathbb{Z}} \hat{f}(q)e^{iqx} = \sum_{n\in\mathbb{Z}} f(x-n) \tag{4.47}$$

Then by the definition of the gaussian and its Fourier transformed we find,

$$G_{per}(x,t) = \sum_{q/2\pi\in\mathbb{Z}} \widehat{G_{per,q}}(t) e^{iqx} = \sum_{q/2\pi\in\mathbb{Z}} e^{-q^2Dt} e^{iq(x-vt)} = \sum_{n\in\mathbb{Z}} \frac{1}{\sqrt{4\pi Dt}} e^{-\frac{(x-vt-n)^2}{4Dt}} \tag{4.48}$$

Thus allowing us to write local density $\rho(x,t)$ in its final form,

$$\rho(x,t) = \int_0^1 \left(\sum_{n\in\mathbb{Z}} \frac{1}{\sqrt{4\pi Dt}} e^{-\frac{(x-vt-y-n)^2}{4Dt}} \right) \rho_0(y)dy \tag{4.49}$$

This form explicitly shows that the probability mass wraps around the domain boundaries. As $t \to \infty$, the exponential terms decay for all $k \neq 0$, and the system relaxes to the uniform stationary state $\rho(x,\infty) = \hat{\rho}_0(0) = \int \rho_0(x)dx$, consistent with the mass conservation pole at $z = 0$ found in Section 4.3.2.

Example 4.1. In this example we consider the initial distribution $\rho_0(x) = cos(q_0 x)$. We will show that one can easily compute $\rho(x,t)$ and show the displacement of the initial local clustering. Note that the Fourier transformed of $\rho_0(x)$ has $\hat{\rho}_{q_0}(0) = \hat{\rho}_{-q_0}(0) = 1/2$, while for all other k $\hat{\rho}_q(0) = 0$. By filling this in into Equation (4.49) one can immediately see that $\rho(x,t)$ reduces to

$$\rho(x,t) = cos(q_0(x-vt))e^{-D(q_0)^2t} \tag{4.50}$$

So the initial local clustering moves actively with speed v, while it amplitude is damped with the diffusion coefficient D.

4.3.4 Solutions of the problem under homogeneous initial conditions

Under homogeneous initial conditions, we can simplify the partial differential equation further. This allows us to better study the behavior of the magnetization in different regimes. The following section will start by providing the details for this derivation. Furthermore, it will study the behavior of the magnetization in four different regimes.

Take the homogeneous initial conditions to be $\rho^+(x,0) = \rho_0^+$ and $\rho^-(x,0) = \rho_0^-$ and define $\rho_0 = \rho_0^+ + \rho_0^-$. This allows us rewrite the PDE for $(\rho(x,t), s(x,t))^T$ given by Equation (4.25) to the following, as the spatial terms will be zero,

$$\begin{cases} \partial_t \rho = 0, \\ \partial_t s = -2\cosh(\beta m)s + 2\sinh(\beta m)\rho \end{cases} \tag{4.51}$$

Note that $\partial_t \rho = 0$ gives $\rho(t) = \rho_0$. The bottom equation contains both $s(t)$ and $m(t)$. We can write $s(t)$ in terms of $m(t)$ by using $m(t) = \int s(x,t)dx / \int \rho(x,t)dx = s(t)/\rho_0$ as the spatial terms can be neglected. Subsisting $s(t) = m(t)\rho_0$ gives,

$$\partial_t m = -2\cosh(\beta m)m + 2\sinh(\beta m) \tag{4.52}$$

We can split this ODE to find the following solution,

$$\int_{m(0)}^{m(t)} \frac{du}{\sinh(\beta u) - u\cosh(\beta u)} = \int_{m(0)}^{m(t)} \frac{du}{\cosh(\beta u)(\tanh(\beta u) - u)} = 2t \tag{4.53}$$

where $m(0) = m_0 = (\rho_0^+ - \rho_0^-)/(\rho_0^+ + \rho_0^-)$. As this integral is not solvable analytically, we can make appropriate approximations in different regimes to get an idea of the behavior of the magnetization $m(t)$. We discuss four different regimes:

(*i*) $\boldsymbol{\beta \gg 1}$ ***and*** $\boldsymbol{m \ll 1}$: In this regime we start by defining $y = \beta u$, this allows us to rewrite the second integral of Equation (4.53) to the following,

$$\frac{1}{\beta}\int_{y(0)}^{y(t)} \frac{dy}{\cosh(y)(\tanh(y) - y/\beta)} = 2t \tag{4.54}$$

one may assume $y/\beta \ll \tanh(y)$, i.e., $\tanh(y) - y/\beta \approx \tanh(y)$. This allows us to write the integral in Equation (4.53) to one that is solvable,

$$\frac{1}{\beta}\int_{y(0)}^{y(t)} \frac{dy}{\sinh(y)} = 2t \quad \Rightarrow \quad \tanh\left(\frac{\beta m(t)}{2}\right) = \tanh\left(\frac{\beta m(0)}{2}\right) e^{2\beta t} \tag{4.55}$$

Here, we can find $m(t)$ explicitly under the following condition,

$$m(t) = \frac{2}{\beta}\arctan\left(\tanh\left(\frac{\beta m(0)}{2}\right) e^{2\beta t}\right) \quad \text{when} \quad \left|\tanh\left(\frac{\beta m(0)}{2}\right)\right| e^{2\beta t} < 1 \tag{4.56}$$

The shape of this function is similar to the behavior we see, in roughly the regime $0.1 < m < 0.9$, when solving the PDE numerically. This will be presented in Section 8 and can be seen in Figure 8.1 for $\sigma = 1$.

(*ii*) $\boldsymbol{\beta = 1}$: For the critical case $\beta = 1$, expanding the hyperbolic terms gives a simple form that is correct up to the fifth-order, i.e., $\sinh(m) - m\cosh(m) = -\frac{1}{3}m^3 + \mathcal{O}\left(m^5\right)$. Substituting this into the first integral of Equation (4.53) gives,

$$\int_{m(0)}^{m(t)} -\frac{3}{m^3} dm = 2t \quad \Rightarrow \quad m(t) = \sqrt{\frac{1}{1 + \frac{4}{3}m^2(0)t}}\, m(0) \tag{4.57}$$

This shows that in the critical case we have convergence to zero with a rate that is inversely proportional to $\sqrt{t}$.

(*iii*) $\boldsymbol{m \approx 0}$: for $|m|$ small, we can neglect higher-order terms in the we expansions of the hyperbolic terms to find $\sinh(m) - m\cosh(m) \approx (\beta - 1)m$. Substituting this into the first integral of Equation (4.53) gives,

$$\partial_t m(t) = 2(\beta - 1)m(t) \quad \Rightarrow \quad m(t) = m(0)e^{2(\beta-1)t} \tag{4.58}$$

This shows us that only for for $\beta < 1$, we converge to zero.

(*iv*) $\boldsymbol{m \approx \pm 1}$: We show the derivation of $m(t)$ for $m \approx 1$. The derivation for $m \approx -1$ is similar. If the magnetization is close to 1, we may assume $m(t) = 1 - \delta(t)$ for $\delta(t)$ small. Using this we can expand the hyperbolic terms, i.e., $\tanh(\beta m) \approx 1 - 2e^{-2\beta}e^{2\beta\delta} \approx 1$ and $\cosh(\beta m) \approx \frac{1}{2}e^{\beta}e^{-\beta\delta} \approx \frac{1}{2}e^{\beta}(1 - \beta\delta) \approx \frac{1}{2}e^{\beta}$. This allows us to rewrite the ODE from Equation (4.52) to,

$$\partial_t m(t) \approx 2\cosh(\beta m(t))\delta \approx e^{\beta}\delta = 2t \quad \Rightarrow \quad \partial_t \delta(t) = e^{\beta}\delta(t) \tag{4.59}$$

This ODE is solvable and by substituting $m(t) = 1 - \delta(t)$ and the initial conditions we find,

$$\begin{cases} m(t) = 1 - (1 - m(0))e^{-\beta t} & \text{for} \quad m \approx 1 \\ m(t) = -1 + (1 + m(0))e^{-\beta t} & \text{for} \quad m \approx -1 \end{cases} \tag{4.60}$$

These equations mimic the behavior we see in numerical simulations in roughly the regime $0.9 < |m| < 1$. Again, this can be seen in Figure 8.1 for $\sigma = 1$.

4.3.5 Weakly nonlinear analysis of the associated amplitude equation

After having studied the linearized behavior of the PDE, this section builds upon the previous and focuses on the weakly nonlinear behavior the PDE by finding and analyzing it associated amplitude equation. For simplicity, and without loss of generality, we assume the total mass $\int_0^1 \rho(x,t) = 1$ and $\rho_0 = 1$. This reduces the magnetization to $m(t) = \int_0^1 s(x,t)dx$. We can now find an equation for the total magnetization by integrating over $\partial_t s$, i.e.,

$$\partial_t m(t) = \int_0^1 \partial_t s dx = 2\left(\sinh(\beta m) - m\cosh(\beta m)\right) \tag{4.61}$$

Note that this ODE is the same as in Equation (4.52). We expand the hyperbolic functions to cubic order in m,

$$\partial_t m = 2\left(\rho_0 \sinh(\beta m) - m\cosh(\beta m)\right) = 2\left(\rho_0\left(\beta m + \frac{\beta^3 m^3}{6}\right) - m\left(1 + \frac{\beta^2 m^2}{2}\right)\right) + \mathcal{O}\left(m^5\right)$$

This allows us to find an approximated differential equation for the magnetization $m(t)$, which is of the form,

$$\partial_t m = am + bm^3 + \mathcal{O}\left(m^5\right) \qquad \text{where} \qquad a = 2(\beta - 1), \quad b = \beta^2\left(\frac{\beta}{3} - 1\right) \tag{4.62}$$

To understand it nonlinear behavior set a control parameter ϵ slightly supercritical near the bifurcation point, i.e., $\beta = 1 + \epsilon$. This immediately gives that $a = 2\epsilon$. As we are looking for the slow non-linear evolution of the system we set the time scale $T = \epsilon t$ and small amplitude scaling $M(t) = \sqrt{\epsilon}A(T)$. Note that this is the standard scaling, that we have for example also seen in the scaling of the generator of this model. However, that this is indeed the proper scaling will be shown shortly. This scaling allows us to write the differential as $\partial_t m(t) = \epsilon^{3/2}\partial_T A(T)$. Furthermore the right-hand side of the differential equation may be rewritten as,

$$am + bm^3 + \mathcal{O}\left(m^5\right) = 2\epsilon^{3/2} + be^{3/2}A^3 + \mathcal{O}\left(\epsilon^{5/2}\right)$$

As all the terms contain an $\epsilon^{3/2}$-term we may divide by this to obtain the following amplitude equation,

$$\frac{dA}{dT} = 2A + bA^3 \tag{4.63}$$

Note that the fixed points of the differential equation are located at $A^* = 0$ and $A^{*2} = -2/b$. by the definition of b we see that $b < 0 \Leftrightarrow \beta < 3$ and $b > 0 \Leftrightarrow \beta > 3$. This allow us to categorize the behavior of the system into three different regimes:

- (i) $\beta\rho_0 < 1$: Linear stability, where $m = 0$ is stable.
- (ii) $1 < \beta < 3$: As A^* are real in this domain the system will converge to $m = \pm 1$ is stable. However, initial local clustering could be preserved, but slowly damped.
- (iii) $\beta > 3$: As A^* is complex in this domain, and therefore one must include higher-order terms to determine its exact behavior. However, we expect the system to converge $m = \pm 1$ and initial clustering to remain longer.

4.4 Analysis for Curie-Weiss rates with local magnetization

During the proof of the hydrodynamic limit in Section 3 and in the previous section, the magnetization was assumed to be global. However, it is expected that the behavior of the system differs under local magnetization. This section, therefore, focuses on the behavior of the system with Curie-Weiss Glauber rates under a local magnetization. The proof of the hydrodynamic limit for a local magnetization was given in Section 3.2. For the local magnetization, we define an interaction kernel $K(x)$ as a normalized function which can be calculated as follows,

$$m_{loc}(x) = \frac{\int_0^1 K(x-y)s(y,t)dy}{\int_0^1 K(x-y)\rho(y,t)dy} = \frac{(K*s)(x,t)}{(K*\rho)(x,t)} \tag{4.64}$$

Assume that the Fourier-transformed of $K(x)$ is given by $K(q)$. Note that for a global magnetization one would have $K(x) = 1$, and for a completely local magnetization one would have $K(x) = \delta(x)$. Under $K(x) = \delta(x)$, $m_{loc}(x)$ is equivalent to the local magnetization that was used in the proof of the hydrodynamic limit of Section 3.2. However, in next sections other variants of the local magnetization are used. Therefore this section is written for a a general local magnetization, not a purely local magnetization. Other possibilities for $K(x)$ include a finite-range Gaussian or a oscillatory kernel. In this section we will derive the Fourier-Laplace-transformed for general $K(x)$ and find the global transport coefficients for both a constant kernel and the Taylor expansion of a general Fourier-transformed kernel.

In order to find the Fourier-transformed of the PDE, we linearize the equation around its steady state $m(t) \equiv m_0 = s_0/\rho_0$, $\rho(x,t) \equiv \rho_0$ and $s(x,t) \equiv s_0$. We take small perturbation around the steady state, $\rho(x,t) = \rho_0 + \tilde{\rho}(x,t)$, $s(x,t) = s_0 + \tilde{s}(x,t) + m(t) \equiv m_0 + \tilde{m}(x,t)$. These are the same conditions as in the case of the global magnetization and therefore the PDE for $(\tilde{\rho}, \tilde{s})$ can be expressed as follows,

$$\begin{cases} \partial_t \tilde{\rho} = \gamma \Delta \tilde{\rho} - \lambda \partial_x \tilde{s}, \\ \partial_t \tilde{s} = \gamma \Delta \tilde{s} - \lambda \partial_x \tilde{\rho} + 2S\tilde{\rho} - 2C\tilde{s} + K\tilde{m} \end{cases}$$

Where $K = 2\beta\rho_0/C$. Note that as ρ_0 and s_0 are constants, $K * \rho_0 = \rho_0$ and $K * s_0 = s_0$. We may use this to rewrite $m_{loc}(x,t)$,

$$m_{loc}(x,t) = \frac{K*s}{K*\rho} = \frac{s_0 + K*\tilde{s}}{\rho_0 + K*\tilde{\rho}} = \frac{s_0}{\rho_0} + \frac{K*\tilde{s}}{\rho_0} - \frac{s_0}{\rho_0}\frac{K*\tilde{\rho}}{\rho_0} \quad \Rightarrow \quad \tilde{m_{loc}}(x,t) = \frac{K*\tilde{s}}{\rho_0} - \frac{s_0 K*\tilde{\rho}}{\rho_0^2} \tag{4.65}$$

Note that this derivation follows the same method as in previous section and $m_{loc}(x,t)$ has a similar form as Equation (4.37). Using the fact that convolution becomes a multiplication in the Fourier regime, we can take the Fourier transform,

$$\begin{cases} \partial_t \hat{\rho} = -\gamma q^2 \hat{\rho} - i\lambda q \hat{s} \\ \partial_t \hat{s} = -\gamma q^2 \hat{s} - i\lambda q \hat{\rho} + 2S\hat{\rho} - 2C\hat{s} + \frac{2\beta\rho_0}{C}\hat{\tilde{m}} \end{cases} \tag{4.66}$$

Substituting the expression for $\hat{\tilde{m}}$, the feedback term becomes $\frac{2\beta}{C}\hat{K}(q)(\hat{s} - m_0\hat{\rho})$. Here we used that $\frac{Ks_0}{\rho_0^2} = \frac{2\beta m_0}{C}$ using $m_0 = s_0/\rho_0$ and $\frac{K}{\rho_0} = \frac{2\beta}{C}$. The evolution of the fast mode $\hat{s}$ is then,

$$\partial_t \hat{s} = -\left(\gamma q^2 + 2C - \frac{2\beta}{C}\hat{K}(q)\right)\hat{s} - \left(i\lambda q - 2S + \frac{2\beta m_0}{C}\hat{K}(q)\right)\hat{\rho} \tag{4.67}$$

We are now left with taking the Laplace transform, where we use $\hat{\rho}(0) = 1$ and $\hat{s}(0) = 0$,

$$\begin{cases} z\bar{\rho} - 1 = -\gamma q^2 \bar{\rho} - i\lambda q \bar{s} \\ z\bar{s} = -\left(\gamma q^2 + 2C - \frac{2\beta}{C}\hat{K}(q)\right)\bar{s} - \left(i\lambda q - 2S + \frac{2\beta m_0}{C}\hat{K}(q)\right)\bar{\rho} \end{cases} \tag{4.68}$$

Since the spin variable relaxes much faster than the density evolves, we adiabatically eliminate $\bar{s}$,

$$\bar{s} = \frac{2S - \frac{2\beta m_0}{C}\hat{K}(q) - i\lambda q}{z + \gamma q^2 + 2C - \frac{2\beta}{C}\hat{K}(q)}\bar{\rho} \tag{4.69}$$

Substituting this the first Equation of equation (4.68) leads to the independent density propagator $\bar{\rho}(q,z)$

$$\bar{\rho}(q,z) = \frac{1}{z+\gamma q^2 + \frac{i\lambda q\left(2S - \frac{2\beta m_0}{C}\hat{K}(q) - i\lambda q\right)}{z+\gamma q^2 + 2C - \frac{2\beta}{C}\hat{K}(q)}} \tag{4.70}$$

The remaining derivation varies with the choice of $\hat{K}(q)$. Three different cases are discussed below, i.e., the global magnetization $\hat{K}(q) = 0$, the (fully) local magnetization $\hat{K}(q) = 1$ and an even Taylor expanded version of $\hat{K}(q)$, $\hat{K}(q) \approx 1 - i\sigma q - \kappa q^2/2 + \mathcal{O}\left(q^4\right)$.

4.4.1 Derivation for the global magnetization $\hat{\mathbf{K}}(\mathbf{q}) = \mathbf{0}$

This case must be the same as the derivation provided in Section 4.3 as we work under the exact same assumptions and is therefore only given as indicator to show that our previous steps have been correct. Substituting $\hat{K}(q) = 0$ in equation (6.18) gives,

$$\bar{\rho}(q,z) = \frac{1}{z+\gamma q^2 + \frac{i\lambda q(2S - i\lambda q)}{z+\gamma q^2 + 2C}} \tag{4.71}$$

this is exactly the same as Equation (4.29). Thus giving us the following global transport coefficients,

$$v_{eff} = \lambda \tanh\left(\beta m_0\right) \quad \text{and} \quad D_{eff} = \gamma + \frac{\lambda^2}{2\cosh^3(\beta m_0)} \tag{4.72}$$

4.4.2 Derivation for the fully local magnetization $\hat{\mathbf{K}}(\mathbf{q}) = \mathbf{1}$

The more interesting case is $\hat{K}(q) = 1$ as this provides new insight in how the system behaves under local interactions. As we proved in Section 3.2 that the hydrodynamic limit to the same PDE is valid all the assumptions remain the same in this derivation. The only difference is the value of $\hat{K}(q)$. Substituting $\hat{K}(q) = 1$ in Equation (6.18) gives,

$$\bar{\rho}(q,z) = \frac{1}{z+\gamma q^2 + \frac{i\lambda q\left(2S - \frac{2\beta m_0}{C} - i\lambda q\right)}{z+\gamma q^2 + 2C - \frac{2\beta}{C}}} \tag{4.73}$$

To find the global transport coefficients we start expanding the fraction in the denominator. We can rewrite the denominator of that fraction by assuming that z will be of the form $z = -iv_{eff}q - D_{eff}q^2$ and neglecting second or higher order terms to find

$$\frac{1}{z+\gamma q^2 + 2C - \frac{2\beta}{C}} \approx \frac{1}{2C - \frac{2\beta}{C} - iv_{eff}q} \approx \frac{1}{2C - \frac{2\beta}{C}}\left(1 - \frac{iv_{eff}q}{2C - \frac{2\beta}{C}}\right) \tag{4.74}$$

Substituting this back into Equation (4.73) gives,

$$\bar{\rho}(q,z) = \frac{1}{z+\gamma q^2 + i\lambda q\left(2S - \frac{2\beta m_0}{C} - i\lambda q\right)\left(\frac{1}{2C - \frac{2\beta}{C}}\left(1 - \frac{iv_{eff}q}{2C - \frac{2\beta}{C}}\right)\right)} \tag{4.75}$$

To find the global transport coefficients we must find the terms linear to iq for the effective velocity and linear to q^2 for the diffusion coefficient. For the effective velocity we find that using $z = -iv_{eff}q - D_{eff}q^2$ and $m_0 = S/C$ that after dividing by iq,

$$v_{\text{eff}} = \lambda\frac{2S - \frac{2\beta m_0}{C}}{2C - \frac{2\beta}{C}} = \lambda\frac{2m_0(C - \frac{\beta}{C})}{2(C - \frac{\beta}{C})} = \lambda m_0 = \lambda\tanh(\beta m_0) \tag{4.76}$$

Note that this active drift is the same as for the global magnetization. Substituting the effective velocity back into Equation (4.75) allows us to find the terms linear with q^2,

$$\bar{\rho}(q,z) = \frac{1}{z+\gamma q^2 + i\lambda q\left(2S - \frac{2\beta m_0}{C} - i\lambda q\right)\left(\frac{1}{2C - \frac{2\beta}{C}}\left(1 - \frac{i\lambda m_0 q}{2C - \frac{2\beta}{C}}\right)\right)} \tag{4.77}$$

Working this out and neglecting third or higher order terms leaves us with,

$$\bar{\rho}(q,z) = \frac{1}{z + i\lambda m_0 q + \gamma q^2 + \lambda^2 \frac{1-m_0^2}{2(C-\beta/C)} q^2} \tag{4.78}$$

Using that $1 - m_0^2 = 1/C^2$ allows us to simplify the equation even further giving us the following global transport coefficients,

$$v_{eff} = \lambda \tanh(\beta m_0) \quad \text{and} \quad D_{eff} = \gamma + \frac{\lambda^2}{2\cosh(\beta m_0)(\cosh^2(\beta m_0) - \beta)} \tag{4.79}$$

Even though the active drift remains the same, this derivation shows that local interactions significantly enhance the diffusion coefficient compared to the global case. The term $(\cosh^2(\beta m_0) - \beta)$ in the denominator indicates that as the system approaches criticality ($C^2 \approx \beta$), the diffusion coefficient diverges. Here fluctuations are enhanced and lead to a long-lived spatially de-ordered state. This negative diffusion coefficient is, in the physics of active matter, a signature for pattern formation. If $D_{eff} < 0$ the homogeneous state is unstable, and the system will spontaneously form high-density clusters, a phenomenon often seen in Motility-Induced Phase Separation (MIPS).

4.4.3 Derivation for a general local kernel

In the following section we derive the global transport coefficient for a general kernel. We start with a symmetric $K(x)$ as they are used most often. Afterwards we give the coefficients for for an asymmetric $K(x)$ which exhibits different behavior. For a symmetric $K(x)$, the odd moments of the expansion of $\hat{\mathrm{K}}(\mathrm{q})$ will be zero and we can therefore take $\hat{K}(q) = 1 - \kappa q^2/2 + \mathcal{O}\left(q^4\right)$ with $\kappa \in \mathbb{R}$. This simplifies finding the modes. Substituting this into Equation (4.70) shows us that up to the second order of q nothing changes and thus no difference will be observed in the transport coefficients. We therefore have,

$$v_{eff} = \lambda \tanh(\beta m_0) \quad \text{and} \quad D_{eff} = \gamma + \frac{\lambda^2}{2\cosh(\beta m_0)(\cosh^2(\beta m_0) - \beta)} \tag{4.80}$$

We now switch to the case where the $K(x)$ is asymmetric, here the expanded version of the Fourier-transformed kernel is of the form $K(q) = 1 - i\sigma q - \kappa q^2/2$ where $\sigma, \kappa \in \mathbb{R}$. Because of the $i\sigma q$ we get a different second order term in the denominator of $\bar{\rho}$. If one works this out, one finds,

$$v_{eff} = \lambda \tanh(\beta m_0) \quad \text{and} \quad D_{eff} = \gamma + \frac{\lambda^2}{2\cosh(\beta m_0)(\cosh^2(\beta m_0) - \beta)} - \frac{\lambda\beta\sigma(m_0 - m_0)}{\cosh^2(\beta m_0) - \beta} \tag{4.81}$$

So the additional term due to drift cancels out and reduces the diffusion coefficient to the same one as the diffusion coefficient for the local case.

5 Biological constraints for the movement of kinesin along microtubules.

Active transport by motors is an example of intracellular transport in which molecular motors actively move cargo along cytoskeletal filaments, such as messenger ribonucleoprotein (mRNP) complexes. While the mathematical framework derived in the previous sections was formulated in abstract terms, its specific components, active motion, state switching, and mean-field interactions, are necessary to capture this biological system. in this section, we derive the modeling requirements directly from the biological context. Rather than capturing the full cycle of these molecular motors, specifically kinesin motors, and their role in a complex three-dimensional geometry, we construct a minimal physical model that isolates the mechanisms most critical for collective transport phenomena: active motion, stochastic switching between active states, diffusive noise and crowding due to the finite binding capacity of the filament. This allows us to capture non-trivial collective behavior such as density- and interaction-dependent effective velocities and spatial heterogeneities. At the same time, this modeling approach still allows for analytical approximations and fast large-scale simulations.

Throughout this section, biological processes are translated into simplified mathematical rules. The remainder of this section is organized as follows. Section 5.1 establishes the biological motivation for the specific model ingredients, including the structure of microtubules and the dynamics of kinesin motors and reviews relevant literature highlighting the limitations of old models and motivating the present approach and research goals. In Section 5.2 we build upon the introduction and formulate the exact central research goals and give the physical hypothesis regarding cooperative transport. Section 5.3 gives additional background on the exclusion rule and on the theoretical predictions associated with it for the global transport coefficients for this biological model.

5.1 Biological background and motivation

To construct a physically relevant model, we must identify the governing constraints of intracellular transport, specifically regarding mRNP complexes. These complexes consist of mRNA molecules packaged with proteins and serve as genetic blueprints for protein synthesis. They must be transported from the nucleus to specific subcellular locations where translation occurs. This spatial transport is crucial for processes such as cell polarity and neuronal signaling [5, 6]. Because passive diffusion is inefficient over cellular length scales, and particularly ineffective within the crowded intracellular environment, mRNPs cannot simply drift to their targets [23, 24]. Instead, they rely on active transport mechanisms driven by molecular motors, such as kinesin. Consequently, developing a model that captures the governing constraints is crucial for understanding how biological systems achieve efficient directed transport despite the stochastic nature of the cellular environment.

One of the primary transport tracks is the microtubule network. Microtubules (MTs) are biopolymers of tubulin dimers arranged in protofilaments and provide well-defined binding sites for molecular motors. Because the length of an MT is orders of magnitude larger than its width, and molecular motors are chemically constrained to step along protofilaments, the transport along individual MTs can be treated as one-dimensional [25]. Furthermore, the well-defined and discrete binding sites naturally motivate the use of a lattice-based description in which kinesin motors occupy distinct discrete positions.

Kinesin motors are ATP-driven enzymes that transport cargo along MTs, predominantly to the plus end [5, 10]. Their motion is characterized by forward steps or paused behavior, both with occasional diffusive fluctuations [10]. So, rather than frequently reversing direction, as seen in many run-and-tumble systems, regulation of transport efficiency primarily occurs through pausing and reactivation of the motor-cargo complexes. At the level of the biological model, this behavior can be represented by an internal state variable that differs for an active transport state and an

inactive state. Transitions between these states are governed by biochemical cues and local or global interactions. This motivates a switching rate in which the internal state determines the mobility of the particle.

Additionally, intracellular transport is inherently collective and thus, especially on small MTs, kinesin-driven motion cannot solely be regulated by interaction via their internal states. That is, kinesin molecules cannot freely overtake one another, leading to congestion and jamming along MTs. These crowding effects reduce the effective transport velocity and alter first-passage times [10]. Consequently, for a realistic model of mRNP transport interactions arising from finite binding capacity must be taken into account, especially for high motor densities.

Previously, no model has been made that incorporates all these constraints. The work of Meskers [17], provided a foundation for deriving diffusion coefficients in the presence of exclusion. However, a significant gap remains, her model treated particles and their internal state as independent. Consequently, it was unable to capture the nuanced crowding behavior observed in the experimental data of Kushwaha et al [10], where Kinesin-II motors demonstrate a specific resilience to jamming. that suggests their switching or stepping rates are coupled to the collective density in a way that simple exclusion models cannot replicate. Even a more complex but still independent model like TASEP-LK explored by Kushwaha et al [10] is unable to capture this behavior.

This discrepancy highlights an 'interaction gap' in the current literature. Standard exclusion models account for steric hindrance but often neglect cooperative regulation. To address this, we introduce Curie-Weiss mean-field switching rates into the exclusion framework. By allowing individual switching rates to be influenced by the magnetization, we aim to capture the cooperative dynamics observed in biological experiments.

5.2 Research goals and hypotheses

The central objective of the physical component of this thesis is to investigate the physical mechanisms that allow for robust intracellular transport despite the constraints of crowding and stochasticity. Specifically, we aim to resolve the discrepancy between standard exclusion models (like TASEP) and the experimental observation that Kinesin-II motors maintain high velocities even at high densities [10]. This leads to the primary research question: How do cooperative interactions between motors and spatial heterogeneity regulate transport efficiency and organization? We hypothesize that transport is not solely determined by steric exclusion, but is actively modulated by collective switching dynamics, where the internal state of a motor depends on the state of its neighbors.

To address these questions, we employ a minimal active-diffusion model with internal state switching. Unlike standard run-and-tumble models where particles act independently, or pure exclusion processes that lack internal states, our model couples the motility state of the particles to the collective configuration of the system, either locally or globally. This choice is motivated by the need to bridge the 'interaction gap' identified in the literature, allowing us to quantify how local and global motor configurations influence the macroscopic observables such as the effective transport velocity and diffusion coefficient.

To capture the cooperative nature of motor regulation, we implement internal state transitions using Curie-Weiss Glauber rates. In this framework, the probability of a motor switching between active and inactive states is not constant, but depends on a local or global magnetization that represents the influence of surrounding motors. This specific choice allows us to introduce a tunable parameter, β, which controls the sensitivity of switching dynamics, and thus is a measure of cooperative motor-cargo regulation. By varying β, we can systematically study how the sensitivity of motors to their environment affects their resilience to jamming and their ability to form coherent clusters. We expect that higher values of β (stronger cooperation) will correlate with increased transport efficiency in crowded regimes.

To model spatial regulation of mRNPs, the framework allows for spatially heterogeneous switching rates. That is, the model can run using a tunable local or global magnetization. That is, we introduce a tunable parameter, σ, which controls the distance over which particles interact with each other. By varying σ, we can systematically study the effects of different interaction distances on the global transport coefficient and on the formation of local structures. We expect that for low σ more local structures will form and different regimes can persist simultaneously affecting the global transport coefficients for $\beta > 1$ (the regime in which particles want to be in the same state). Additionally this spatial heterogeneity caused by exclusion violates the assumptions of the hydrodynamic derivation. Therefore, this thesis aims to find the differences, but also consistencies, between the mean-field hydrodynamic PDE and this exclusion- and local-based simulation.

5.3 Exclusion interactions and crowding effects

Transport of molecular motor along microtubules is subject to geometric constraints. MTs have discrete binding sites and each kinesin motor occupies a finite amount of space when bound to the filament. As a consequence, motors on the same filament cannot easily overtake each other or simultaneously occupy the same binding site. This becomes particularly relevant at moderate to high motor densities, when crowding leads to the formation of queues and traffic jams, resulting in a reduction of the effective transport velocity and increased residence times. Experimental studies show that such jamming effects occur regularly, especially in regions where motors accumulate due to regulatory or anchoring mechanisms [8]. Any realistic model must therefore incorporate exclusion interactions.

In the biological model, exclusion is implemented by limiting the occupation number of each site. That is, let $n(x,t)$ be the number of particles occupying site x at time t, the exclusion condition is,

$$n(x,t) \leq k \tag{5.1}$$

where $k \in \mathbb{N}$ is the maximum allowed capacity. $k = 1$ corresponds to hard exclusion, while $k > 1$ models finite local capacity or soft exclusion. Importantly, while the underlying dynamics remain stochastic and local mean-field based, exclusion introduces interactions between individual particles. We must therefore renormalize the transport rates after knowing which target sites are available.

Exclusion-driven transport has been studied considerably in the context of the asymmetric simple exclusion process (ASEP) and its totally asymmetric variant (TASEP) [7, 10]. In these one-dimensional lattice models, particles hop to neighboring sites subject to hard-core exclusion, with rate p for the positive direction and q for the negative direction (with $p+q = 1$). Under the TASEP model one has $q = 0$. We now give a short derivation of their effective velocities as this observable is extensively studied this thesis. To start, let the system be in a stationary Bernoulli product measure with density $\rho \in [0,1]$. Then, the probability of a right jump is given by $\rho(1-\rho)$ and to the left by $(1-\rho)\rho$. Hence the *average current* and *effective particle velocity* can be calculated

$$J_{ASEP}(\rho) = (p-q)\rho(1-\rho) \qquad v_{eff}^{ASEP}(\rho) = \frac{J(\rho)}{\rho} = (p-q)(1-\rho) \tag{5.2}$$

So each particle is linearly slowed down by blocking from others and at full density $\rho = 1$ motion stops [7].

While the above models are insightful, they differ fundamentally from our biological model. First, in the (T)ASEP model particles possess no internal state with switching dynamics. These dynamics introduce cooperative behavior which are hard to capture in an simple v_{eff} function. Second, these switching dynamics rely on local or global magnetization. Finally, in the (T)ASEP model particle motion is not combined with diffusion. Therefore, preforming this derivation for the biological model is hard analytically, but can be approximated. Without exclusion we know that for the hydrodynamic PDE with Curie-Weiss Glauber rates the effective velocity for right and left moving particles is given by Equation (4.32). That is $v_{eff} = \lambda m(\beta)$ where $m(\beta)$ can be found by

solving $m(\beta) = \tanh(\beta m(\beta))$. Shifting this to right and non-moving particles we can approximate that under exclusion the effective velocity will be given by,

$$v_{eff}(\rho, \beta) \approx \lambda \frac{1 + m(\beta)}{2} \cdot (1 - \mathbb{P}[\text{target site blocked}]) \approx \lambda \frac{1 + m(\beta)}{2} (1 - \Phi(\rho, \beta)) \tag{5.3}$$

where $\Phi(\beta)$ approximates what is the probability that a target site is not available. Predictions of such functions $\Phi(\rho, \beta)$ will be discussed in Equation (6.19).

6 One-dimensional biological PDE model

To describe the macroscopic density evolution of mRNP complexes transported by kinesin, we can adapt the mean-field hydrodynamic framework derived in Section 3. While the previous derivation was general, here we map the internal state $\sigma \in \{-1, 1\}$ specifically to the biologically relevant inactive and active motility states of the motor proteins. we start by giving a baseline continuum description to predict the large-scale transport phenomena in Section 6.1. Secondly we include exclusion in Section 6.2 based on work by Kourbane-Houseene et a [4] and try to derive the global transport coefficients in this more complex case.

The requirements for the model given in Section 5 exactly match the model presented in Section 3 for the continuum case, with the only exception the internal states $\sigma \in \{-1, 1\}$ do not have velocities $\{-1, 1\}$ but rather $\{0, 1\}$ as there is one inactive state and on active right moving state. As all the details are the same we reference Section 3 for the exact details of the continuum model. The PDE and the small change needed to adjust for the shift in the active velocities will be given below.

Additionally, the PDE presented in section 6.1 will be solved computationally to verify if the long-term linearized theoretical results match the long-term results of a computational simulations. The exact method of how to solve this PDE computationally will not be discussed as it follows the most well-known and widely used methods to solve a PDE numerically. The exact details can be found in the code [26].

6.1 Coarse-grained PDE model modified for biological parametrization

We consider a one-dimensional spatial domain $Y = [0, 1]$ where each particle has internal state $\sigma \in S = \{-1, +1\}$, interpreted as the active and inactive transport states. Let the macroscopic densities for $t \geq 0$ be denoted by $\rho_-(x, t)$ and $\rho_+(x, t)$, then the PDE is given by,

$$\begin{cases} \partial_t \rho_+ = \gamma \Delta \rho_+ - \lambda \partial_x \rho_+ + c(m, -1)\rho_- - c(m, +1)\rho_+, \\ \partial_t \rho_- = \gamma \Delta \rho_- + c(m, +1)\rho_+ - c(m, -1)\rho_- \end{cases} \tag{6.1}$$

where directed motion has rate λ and the diffusion rate γ. Note that the PDE only differs from the original PDE (Equation (4.8)) in λ since we now have active and inactive movement. Therefore for this model we can also find the effective velocity and effective diffusion under steady state homogeneous assumptions,

$$v_{eff} \approx \lambda \frac{1 + m(\beta)}{2} \quad \text{and} \quad D_{eff} \approx \gamma + \frac{\lambda^2}{2\cosh^3(\beta m(\beta))} \tag{6.2}$$

where $m(\beta)$ is found by solving $m = \tanh(\beta m)$ and with Curie-Weiss Glauber rates under a local magnetization with a Gaussian kernel, mathematically,

$$c(m(x, t), \sigma) = e^{-\sigma \beta m(x,t)} \quad \text{where} \quad m(x, t) = \frac{(K_\sigma * s)(x, t)}{(K_\sigma * \rho)(x, t)} \quad \text{with} \quad K_\sigma(x) = \frac{1}{\sqrt{2\pi\sigma^2}} e^{-\frac{x^2}{2\sigma^2}} \tag{6.3}$$

with density $\rho = \rho_+ + \rho_-$ and magnetic difference $s = \rho_+ - \rho_-$. In the proof in Section 3 we assumed periodic or infinite boundary conditions. However for a polar finite MT this is not possible. Therefore, we consider Neumann boundary conditions of the form

$$\partial_x \rho_+(0, t) = \partial_x \rho_+(1, t) = 0, \qquad \partial_x \rho_-(0, t) = \partial_x \rho_-(1, t) = 0 \tag{6.4}$$

The mathematical framework derived in Section 3 remains valid for very broad range of initial conditions. As long as the initial distribution are chosen from some Poisson distribution (Equation (3.6)) this PDE model remains valid. Exact initial conditions will be given in Section 7.1. Note that, as seen in the analyses in Section 4, under homogeneous steady state assumption the PDE, from Equation (6.1) will converge to a PDE of the following form:

$$\partial_t \rho = -v_{eff} \partial_x \rho + D_{eff} \Delta \rho \tag{6.5}$$

where v_{eff} the effective velocity and D_{eff} the diffusion coefficient.

6.2 Coarse-grained PDE model under the exclusion principle

In this section we expand the hydrodynamic PDE derived in Section 3 to derive v_{eff} and D_{eff} under exclusion to try and find the global transport coefficients theoretically for the biological model. We start by adjusting the PDE to fit for these forces based on a paper by Kourbane-Houseene et al. [4]. By a similar method as in Section 4.3, v_{eff} and D_{eff} will be found. Note that, for simplicity of the computations, this will be done in the frame in which active particles can move left and right instead of the in Section 6.1 considered inactive and right moving particles. Based on Kourbane-Houseene et al. [4], the PDE for our system can be written as,

$$\begin{cases} \partial_t \rho = \gamma \Delta \rho - \lambda \partial_x \left[(1-\rho) s \right], \\ \partial_t s = \gamma \Delta s - \lambda \partial_x \left[(1-\rho) \rho \right] + 2 \sinh(\beta m) \rho - 2 \cosh(\beta m) s \end{cases} \tag{6.6}$$

Note that this very similar to the PDE without exclusion given in Equation (4.25) except for the $(1-\rho)$ found in the terms for the active movement. To find v_{eff} and D_{eff} we expand ρ and s around the steady homogeneous state, similar as in Section 4.3. Mathematically, we take $\rho(x,t) \equiv \rho_0$ and $s(x,t) \equiv s_0$ such that $m_0 = s_0/\rho_0$ with $m_0 = \tanh(\beta m_0)$. Linearizing around the steady state, i.e. take $\rho(x,t) = \rho_0 + \tilde{\rho}(x,t)$ and $s = s_0 + \tilde{s}(x,t)$, gives

$$\begin{cases} \partial_t \tilde{\rho} = \gamma \Delta \tilde{\rho} - \lambda(1-\rho_0) \partial_x \tilde{s} + \lambda s_0 \partial_x \tilde{\rho}, \\ \partial_t \tilde{s} = \gamma \Delta \tilde{s} - \lambda(1-2\rho_0) \partial_x \tilde{\rho} + 2S\tilde{\rho} - 2C\tilde{s} + K\tilde{m} \end{cases} \tag{6.7}$$

where $C = \cosh(\beta m_0)$, $S = \sinh(\beta m_0)$ and $K = 2\beta\rho_0/C$. This is the same as in Section 4.3. However, this PDE differs in the terms for the active movement. To simplify computations we preform a Galilean transformation, that is $x' = x - v_0 t, \quad v_0 := \lambda s_0 = \lambda \rho_0 m_0$. This results the following PDE,

$$\begin{cases} \partial_t \tilde{\rho} = \gamma \Delta \tilde{\rho} - \lambda(1-\rho_0) \partial_x \tilde{s}, \\ \partial_t \tilde{s} = \gamma \Delta \tilde{s} - \lambda(1-2\rho_0) \partial_x \tilde{\rho} + 2S\tilde{\rho} - 2C\tilde{s} + K\tilde{m} + \lambda s_0 \partial_x \tilde{s} \end{cases} \tag{6.8}$$

With PDE properly linearized around the steady state ρ_0, s_0, we apply the Fourier-Laplace transform to derive the global transport coefficients. As was the case for the derivation with no exclusion in Section 4.3 we start by taking the Fourier transform for $q \neq 0$,

$$\begin{cases} \partial_t \hat{\rho} = -\gamma q^2 \hat{\rho} - i\lambda(1-\rho_0) q \hat{s}, \\ \partial_t \hat{s} = -\gamma q^2 \hat{s} - i\lambda(1-2\rho_0) q \hat{\rho} + 2S\hat{\rho} - 2C\hat{s} \end{cases} \tag{6.9}$$

We can now take the Laplace transform and use, again, that $\bar{\rho}(0) = 1$, $\bar{s}(0) = 0$,

$$\begin{cases} z\bar{\rho} - \bar{\rho}(0) = -\gamma q^2 \bar{\rho} - i\lambda(1-\rho_0) q \bar{s}, \\ z\bar{s} - \bar{s}(0) = -\gamma q^2 \bar{s} - i\lambda(1-2\rho_0) q \bar{\rho} + 2S\bar{\rho} - 2C\bar{s} \end{cases} \tag{6.10}$$

We proceed with the adiabatic elimination of the fast mode $\bar{s}$ by solving the second equation of Equation (6.10),

$$\bar{s}(q,z) = \frac{2S - i\lambda(1-2\rho_0)q}{2C + z + \gamma q^2 - i\lambda s_0 q} \bar{\rho}(q,z) \tag{6.11}$$

Substituting this into the first equation of Equation (6.10) yields the independent density propagator,

$$\bar{\rho}(q,z) = \frac{1}{z + \gamma q^2 + i\lambda(1-\rho_0) q \left(\frac{2S - i\lambda(1-2\rho_0)q}{2C + z + \gamma q^2 + i\lambda s_0 q} \right)} \tag{6.12}$$

To find the effective velocity v_{eff} and D_{eff}, we analyze the poles under the assumption of $z = -iv_{eff}q - D_{eff}q^2$. We expand the denominator term around the drift, assuming the adiabatic limit $|z| \ll 2C$,

$$\frac{1}{2C + z + \gamma q^2 + i\lambda s_0 q} \approx \frac{1}{2C - iv_{eff}q + i\lambda s_0 q} \approx \frac{1}{2C} \left(1 - \frac{iq}{2C}(v_{eff} - \lambda s_0) \right) \tag{6.13}$$

Substituting this expansion back into the density propagator (6.12),

$$\bar{\rho}(q,z) = \frac{1}{z + \gamma q^2 + i\lambda(1-\rho_0)q\,(2S - i\lambda(1-2\rho_0)q)\,\frac{1}{2C}\left(1 - \frac{iq}{2C}(v_{eff} - \lambda s_0)\right)} \tag{6.14}$$

We now collect terms order by order to identify the coefficients. The linear terms in iq, indicating the effective velocity are,

$$i\lambda(1-\rho_0)q\frac{2S}{2C} = i\lambda(1-\rho_0)\tanh(\beta m_0)q = i\lambda(1-\rho_0)m_0 q \tag{6.15}$$

using $m_0 = S/C$. For the effective diffusion we must look of the quadratic terms linear with q^2, we collect the diffusion term, the active term, and the relaxation correction term. Noting that $v_{eff} + \lambda s_0 = \lambda(1-\rho_0)m_0 - \lambda\rho_0 m_0 = \lambda(1-2\rho_0)m_0$,

$$\gamma q^2 + i\lambda(1-\rho_0)q(-i\lambda(1-2\rho_0)q)\frac{1}{2C} + i\lambda(1-\rho_0)q\frac{2S}{2C}\left(-\frac{iq}{2C}(v + \lambda s_0)\right) \tag{6.16}$$

Working this out results in the following,

$$\gamma q^2 + \frac{\lambda^2(1-\rho_0)(1-2\rho_0)}{2C}(1+m^2)q^2 \tag{6.17}$$

Substituting Equation (6.15) and (6.17) back into Equation (6.14) simplifies the density propagator to

$$\bar{\rho}(q,z) = \frac{1}{z + i\lambda(1-\rho_0)mq + \gamma q^2 + \frac{\lambda^2(1-\rho_0)(1-2\rho_0)}{2C}(1+m^2)q^2} \tag{6.18}$$

From this it we can read that v_{eff} and D_{eff} are given by,

$$v_{eff} = \lambda(1-\rho_0)m_0 \qquad \text{and} \qquad D_{eff} = \gamma + \frac{\lambda^2(1-\rho_0)(1-2\rho_0)}{2\cosh(\beta m_0)}\left(1+m_0^2\right) \tag{6.19}$$

To formally verify that derived global transport coefficients are correct under hydrodynamic scaling, we shift to a co-moving frame. We define the scaled propagator shifted by the drift velocity $v_{eff} = \lambda(1-\rho_0)m_0$ as,

$$S_\epsilon(q,z) = \lim_{\epsilon\to 0} \epsilon^2 \bar{\rho}(\epsilon q, \epsilon^2 z - i v_{eff}\epsilon q) \tag{6.20}$$

Substituting expression (6.18) into this function results in

$$S_\epsilon(q,z) = \lim_{\epsilon\to 0} \frac{\epsilon^2}{\epsilon^2 z - i v_{eff}\epsilon q + i v_{eff}\epsilon q + D_{eff}\epsilon^2 q^2} \tag{6.21}$$

Dividing the numerator and denominator by ϵ^2 and taking the limit shows us that the density profile converges to the macroscopic structure function:

$$S_{macro}(q,z) = \frac{1}{z + D_{\text{eff}} q^2} \tag{6.22}$$

This shows us that the structure function indeed converges with the same global transport coefficients. These transport coefficients show important properties that depend on the average density ρ_0 in an interesting manner. We will now interpret these coefficient and compare them to there simpler counterparts following from the TASEP model (Section 5.3). The effective velocity $v_eff = \lambda(1-\rho_0)m_0$ demonstrates how the exclusion principle modifies active transport. This result is closely related to the TASEP model, where the drift is also scaled by the available volume $(1-\rho_0)$, as seen in Equation (5.2). This indicated that as the density increases, the ability of the particles to 'run' is hindered by their neighbors. In the limit $\rho_0 \to 1$, the velocity vanishes, representing a fully jammed state.

The effective diffusion coefficient provides us a window into the phenomenon on Motility-Induced Phase Seperation (MIPS). For a standard random walk, increasing the density simply leads to more collisions. However, here the factor $(1-2\rho_0)$ in the numerator can lead to a drastic reduction in the diffusion coefficient. When this active contribution becomes sufficiently negative (relative to the passive diffusion γ), it signals an instability in the homogeneous density profile. Then particles tend to cluster rather than disperse, leading to the formation of local structures.

7 One-dimensional biological particle model

The hydrodynamic PDE derived in Section 6.1 neglects discrete spatial structure, finite particle effects and correlations induced by crowding and exclusion. To fully address the research question regarding the role of local interactions and exclusion in transport regulation, this section introduces a particle-based model that explicitly resolves individual motors on a discrete lattice and incorporates exclusion introduced in Section 5. The particle model constructed here therefore remains closer to the requirements presented in Section 5. This allows for systematic comparison between the hydrodynamic limit and the microscopic dynamics. In Section 7.1-7.3 an overview of the model, its rules and parameters is given. Section 7.4 gives a pseudocode for the Gillespie algorithm that is used in which all the rules introduced in the previous sections are combined.

7.1 State space and microscopic configuration

We consider a one-dimensional lattice of length N, representing a single MT protofilament, i.e.,

$$X = \{0, 1, \ \dots \ , N\} \subseteq \mathbb{Z}$$

where $N\Delta x$ denotes the physical length of the MT and Δx is the tubulin dimer length. Without loss of generality we set $N\Delta x = 1$ to simplify the modeling approach. The system state at time $t \geq 0$, is then given by,

$$\eta(t) = \{(x_i(t), \sigma_i(t), b_i(t))\}_{i=1}^{M}, \quad \text{where} \quad x_i(t) \in X, \sigma_i \in S = \{-1, +1\}, b_i \in B = \{0, 1\} \tag{7.1}$$

Where σ_i represents the internal state of the particle which we associated to its active drift in Section 7.2. $b_i(t)$ indicates if particle i is anchored ($b_i = 1$) or not ($b_i = 0$). This will be explained in more detail in Section 7.3. We then define the local occupation number as,

$$n(x, t) := \sum_{i=1}^{M} \mathbb{1}_{\{x_i(t)=x\}} \tag{7.2}$$

At both boundaries Neumann BCs apply. That is we suppress any jump would leave the domain so no creation or annihilation of particles at the boundary is possible. Mathematically, we define the admissible jump set to be,

$$\mathcal{N}(x) = \begin{cases} \{1\}, & x = 0, \\ \{x-1, x+1\}, & 1 \leq x \leq N-1, \\ \{N-1\}, & x = N, \end{cases} \tag{7.3}$$

The model derived in Section 3 worked on any initial condition chosen from a Poisson distribution. To test both mathematical rigor of the model and mimic the biological context we each propose a different initial condition. To test the model and link it to the mathematics developed in Section 3 and 4 we propose that the particles are randomly homogeneously divided over the domain X with equal probability to be in each state. This will create what we call a homogeneous initial condition with noise because of the random placement at a position and random choice of the internal state. It is expected that this state is close to the steady state of the system and therefore allows us to compare the model to the theoretical predictions.

This is not a biologically motivated initial condition. As discussed in Section 5, The distributions of the motors is not uniform but depends on specific biochemical cues. Additionally, as the active particles move from left to right, an initial conditions must have with more particles on the left than on the right. More precisely, the microscopic configuration η_N^0 is initialized for a fixed number of particles N by treating the initial macroscopic density profile $\rho_0(x, \sigma)$ as a probability density. For each particle $i \in \{1, \ \dots \ , N\}$, we first determine its state $\sigma \in \{-1, +1\}$ according to a fraction f_+, which indicates the initial fraction of particles in the active state. Then, its position x_i is

drawn from a probability density function $P(x|\sigma)$ defined by the normalized shape of the initial profile,

$$x_i \sim \Psi_\sigma(x) = \frac{\rho_0(x,\sigma)}{\int \rho_0(x,\sigma)dx} \tag{7.4}$$

Before we initialized with $\Psi_\sigma(x)$ uniform, but in the biological context we define specific probability functions to represent the non-equilibrium distribution of the motors:

(i) $\Psi_+(x)$: For the active state, we sample positions from an exponential decay function $\Psi_+(x) \propto \exp(-x/\lambda_{decay})$. This represents a free-floating population of motors concentrated near a the nucleus.

(ii) $\Psi_-(x)$: For the state, we combine a small uniform baseline probability with localized Gaussian peaks. These peaks, centered at anchor positions a_j with width w and mass M, represent localized binding sites on the MT as will be discussed in more detail in Section 7.3

$$\Psi_-(x) \propto 0.05 + \sum_j M_j \exp\left(-\frac{(x-a_j)^2}{2w_j^2}\right) \tag{7.5}$$

This probabilistic approach ensures that while each simulation run begins with a discrete, random particle configuration, the ensemble average of these configurations is consistent with the macroscopic densities $\rho_0^\pm$ used in the hydrodynamic limit.

7.2 Elementary events and rate scaling

Similar to the hydrodynamic PDE derived in Section 6.1 the particle-based model includes active drift, diffusion and internal state switching under Curie-Weiss Glauber rates. However these rates in the hydrodynamic PDE must be scaled to be usable in a particle-based model. Mathematically, for a particle i at site x,

(i) *Active drift*: The considers particles with $\sigma_i = -1$ to be inactive particles and particles with $\sigma_i = 1$ to be active particles, i.e.

$$x_i \to x_i + 1 \qquad \text{with rate} \qquad \lambda/\Delta x \tag{7.6}$$

Note that this scaling is similar to scaling between λ and λ_N in Section 3.1.

(ii) *Diffusion*: Particles in both states diffuse according to,

$$x_i \to x_i \pm 1 \qquad \text{with rate} \qquad \gamma/\Delta x^2 \tag{7.7}$$

(iii) *internal state switching*: Each particle switches state according to Curie-Weiss Glauber rates,

$$\sigma_i \to -\sigma_i \qquad \text{with rate } c(m,\sigma) = e^{-\sigma\beta m} \tag{7.8}$$

Define $\rho(x) = n_+(x)+n_-(x)$ and $s(x) = n_+(x)+n_-(x)$. Then the magnetization is computed using

$$m(x) = \frac{(K*s)(x)}{(K*\rho)(x)} \quad \text{where} \quad K_\sigma(x) = \frac{1}{\sqrt{2\pi\sigma^2}} e^{-\frac{x^2}{2\sigma^2}} \tag{7.9}$$

Note that this definition of the magnetization allows for a strictly local, local or global magnetization depending on the choice of σ.

7.3 Exclusion rules

The exclusion constraint is given by Equation (5.1) introduced in Section 5.3. That is, $n(x,t) \le k$, where $k \in \mathbb{N}$ is the maximum site occupancy. Exclusion modifies the generator of the process by truncating the jump rates,

$$\lambda \to \lambda \mathbb{1}_{\{n(x+1,t)\le k\}}, \qquad \gamma \to \gamma \mathbb{1}_{\{n(x\pm1,t)\le k\}} \tag{7.10}$$

Note that for $k = 1$ gives a hard-core exclusion particle system leading to strong spatial correlations and jamming. For $\rho \ll k$ the exclusion constraint rarely applies reducing the system to the mean-field PDE derived in Section 6.1.

7.4 Pseudocode for the Gillespie algorithm

The dynamics introduced in Section 7.1-7.3 define a continuous-time Markov process with state-dependent rates and hard constraints arising from exclusion and boundary conditions. To generate exact paths of this process, we employ a Gillespie simulation algorithm. Since all transition occur at exponentially distributed waiting times, Algorithm 7.1 produces and exact realization of the microscopic dynamics. The exact code, including the details for the storage of the results, visualizations and parameter sweeps can be found in the code [26].

Algorithm 7.1 Calculate $x(t) = \{x_i(t), i \in \{1, \dots, M(t)\}$

Input: Lattice length L, site capacity k, number of particles M; rates $\gamma, \lambda, \beta, k_{on}, k_{off}, k_{exit}$; magnetization kernel K_σ; anchoring regions $\mathcal{A}$; final time T

Initialization:

Set t = 0

Set initial state $\eta(0)$ as explained in the final part of Section 7.2

Main loop:

while $t < T$ **do**

Compute occupancies

$$\rho(x) = \sum_{i=1}^{N(t)} \mathbf{1}_{\{x_i = x\}}, \qquad \rho^{\pm}(x) = \sum_{i=1}^{N(t)} \mathbf{1}_{\{x_i = x,\ \sigma_i = \pm 1\}}$$

Compute magnetization field

$$m(x) = \frac{(K * (\rho^+ - \rho^-))(x)}{(K * (\rho^+ + \rho^-))(x)}$$

for $i = 1, \dots, M(t)$ **do**

Let $x = x_i, \sigma = \sigma_i, b = b_i$. Compute the rates:

Diffusion: $r_i^{\text{left}} = \gamma\, \mathbb{1}_{\{b=0\}}\, \mathbb{1}_{\{x>1\}}\, \mathbb{1}_{\{\rho(x-1)<K\}}, \qquad r_i^{\text{right}} = \gamma\, \mathbb{1}_{\{b=0\}}\, \mathbb{1}_{\{x<L\}}\, \mathbb{1}_{\{\rho(x+1)<K\}}$

Active: $r_i^{\text{act}} = \lambda\, \mathbb{1}_{\{b=0\}}\, \mathbb{1}_{\{\sigma=+1\}}\, \mathbb{1}_{\{x<L\}}\, \mathbb{1}_{\{\rho(x+1)<K\}}$

Flip: $r_i^{\text{flip}} = \exp\big(-\beta\, \sigma\, m(x)\big)$

Total rate for particle i

$$r_i = r_i^{\text{left}} + r_i^{\text{right}} + r_i^{\text{act}} + r_i^{\text{flip}}$$

end for

Compute total system rate:

$$R = \sum_{i=1}^{M(t)} r_i$$

Draw $\tau \sim \text{Exp}(R)$ then $t \leftarrow t + \tau$

Choose $i \in \{1, \dots, M(t)\}$ with $\mathbb{P}(i) = r_i / R$

Choose event for particle i from the multinational distribution proportional to

$$\big(r_i^{\text{left}}, r_i^{\text{right}}, r_i^{\text{act}}, r_i^{\text{flip}}\big)$$

Execute the selected transition and update (x_i, σ_i, b_i)

Remove particle from $M(t)$ if exit occurs

end while

8 Results of the one-dimensional biological particle model

This section presents the results of the one-dimensional particle model and PDE solver introduced in Section 7 and 6 and links them to the theoretical predictions made in Sections 3-5. Section 8.1 focuses purely on the mathematical setting, where exclusion and other extra biological rules are absent. Here we can assess convergence towards the results from the hydrodynamic limit and can additionally study formation of clusters and other local structures which we were unable to do purely analytically. Subsequently, we incorporate biologically motivated features, such as exclusion and inactive and active particles (instead of left and right moving particles) and analyze how these modify transport properties and the formation of local structures. Finally, Section 8.4 compares the particle model under exclusion to experimental results and shows that our model improves over the baseline model used in the same paper by Kushwaha et al. [10].

8.1 Mathematical validation and emergent structure

We begin by studying the particle model of Section 7 in a minimal setting, without exclusion interactions and with periodic boundary conditions. Additionally, we consider left- and right moving particles instead of inactive and right moving particles. In this regime, the model corresponds directly to the hydrodynamic description derived in Section 3 and the particle model can thus easily be compared to the analytical results derived in Section 4 and to a simple PDE solver that solves the PDE from Section 4 numerically. To show the correspondence between the models and analytical results, we analyze the convergence of global observables and effective parameters, under different values of β and both global and local mean-field interactions. In addition, the models allow us to study spatial fluctuations and local structure, which are hard to capture in analytical derivations.

8.1.1 Convergence of the global magnetization

The first important global observable is the magnetization $m(t)$. We analyze this variable first because it acts as the primary order parameter of the system. It indicates whether we achieved the alignment predicted by the mean-field theory. While analytical results have shown that for any kernel, i.e. local or global interactions, the global magnetization will follow the mean-field Equation 2.20 in the steady state, that is,

$$m = \tanh(\beta m)$$

it is unknown how the kernel influences the speed of the convergence. Simulations show that indeed, for any initial conditions and chosen parameter the system converges to this mean-field equation. However, Figure 8.1 shows that for lower σ, that is more local interactions, the speed of convergence decreases and becomes more irregular. This is easily interpreted as a local magnetization allows for different regions of magnetization to co-exist, slowing done convergence of the global magnetization. Note that this simulation was run for a system with spatially uniform homogeneous initial conditions with small, random pointwise perturbations.

8.1.2 Convergence of the effective velocity

We next consider the effective velocity v_{eff}. In absence of exclusion, the hydrodynamic description predicts a constant effective velocity given by Equation 4.32, that is,

$$v_{eff} = \lambda \tanh(\beta m) \tag{8.1}$$

Figure 8.2 shows the effective velocity extracted for both the particle and PDE model for different values of β. In all cases, the results from the models converge to the analytical expression for v_{eff}. The convergence of $v_{eff}(t)$ as a function of time under different values of σ as illustrated in figure 8.3. After an initial transient, the effective velocity, for different σ, converges to the analytical predictions. We, again, see that for smaller values of σ this convergence takes longer and is more irregular but does not affect the asymptotic value. These results confirm that the models reproduce the effective velocity predicted by the hydrodynamic theory.

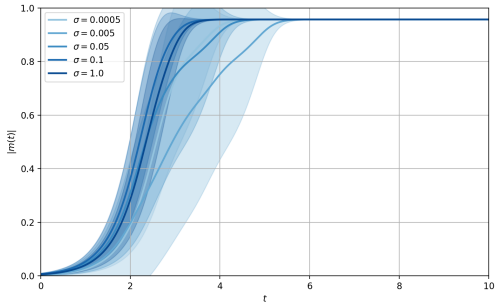

Figure 8.1: Time evolution of the global magnetization $m(t)$ for different values of σ under $\beta = 2$. Solid lines denote the average value of the magnetization while the shaded areas give the standard deviations. Lower σ, i.e., local interactions, result in slower convergence to the steady state magnetization. Any strength of interaction, however, results in convergence to the Curie-Weiss predictions.

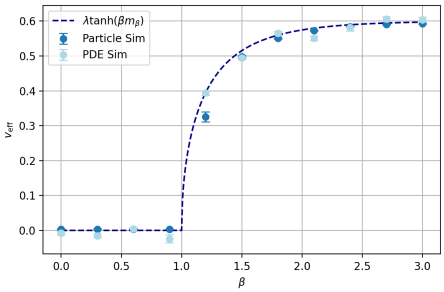

Figure 8.2: Effective velocity as a function of β for $\lambda = 0.6$ for a global magnetization. Results from both the particle and PDE model are shown and converge to the dashed line which gives the theoretical prediction given by Equation (8.1).

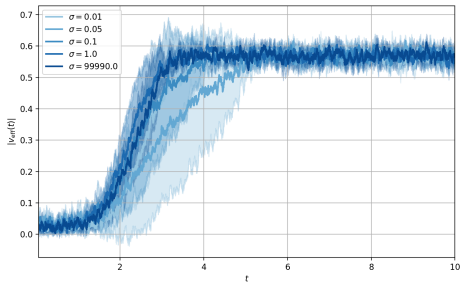

Figure 8.3: Time evolution of the effective velocity for different values of σ under $\beta = 2$ and $\lambda = 0.6$ for a global magnetization. Solid lines denote the average value of the effective velocity while the shaded areas give the standard deviations. Any value of σ results in convergence to the steady state predictions, however, lower σ result in slower convergence.

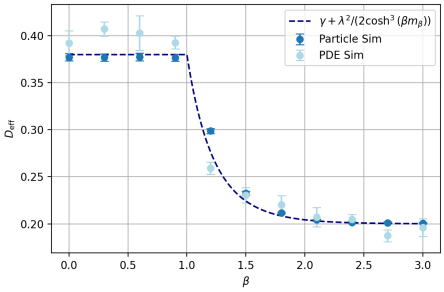

Figure 8.4: Effective diffusion coefficient as a function of β under $\lambda = 0.4$ and $\gamma = 0.2$. Results from both the particle and PDE model are shown and converge to the dashed line which gives the theoretical prediction given by Equation (8.2).

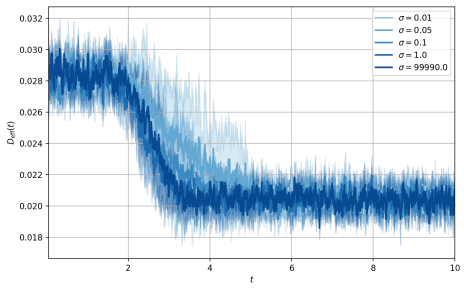

Figure 8.5: Time evolution of the effective diffusion coefficient for different values of σ under $\beta = 2$ and $\lambda = 0.4$ and $\gamma = 0.2$. Solid lines denote the average value of the effective diffusion coefficient while the shaded areas give the stardard deviations. Any value of σ results in convergence to the global steady state predictions, however, lower σ result in slower convergence.

8.1.3 Convergence of the effective diffusion coefficient

We now turn to the effective diffusion coefficient D_{eff}. The hydrodynamic limits predict a constant diffusion coefficient given by Equation 4.32, that is,

$$D_{eff} = \gamma + \frac{\lambda^2}{2\cosh^3(\beta m)} \tag{8.2}$$

Figure 8.4 compares the diffusion coefficient obtained from both the particle and PDE model with theoretical predictions for varying values of β. As for the effective velocity, the numerical results converge to the analytical expression given by Equation (8.2). This agreement holds in both the low-β regime, where fluctuations and little alignment increases D_{eff}, as in the high-β regime, where persistent directional movement does not contribute to D_{eff} but to v_{eff}. The time evolution of the diffusion coefficient is shown in figure 8.5. Similar to both the global magnetization and the effective velocity, it is observed that, while lower values of σ increase the duration of the transient regime, the asymptotic value is still reached. Importantly, Equation 4.79 derived a different diffusion coefficient for the local magnetization, but even for extremely small values of σ this coefficient is not found. This derivation required many assumptions, for example the linearization around the homogeneous state. One of these might be wrong given is an incorrect coefficient, or the particle model is not able to model such a completely local magnetization. Taken together, these results demonstrate that both models reproduce the effective diffusion coefficient predicted by the hydrodynamic theory for the global magnetization. Thus deviations observed in later sections will originate from interaction effects instead of numerical artifacts.

8.1.4 Local structure and spatial fluctuations

While the global transport coefficient are accurately captured by the hydrodynamic theory, the models can additionally reveal spatial fluctuations and local structure, that are much harder to study analytically. These effects are analyzed next. The particle and PDE model allow us directly probe local density variations and emergent spatial structure. In this subsection we analyze these effects starting from a homogeneous initial state with noise. Again, exclusion is not present, allowing us to study structure formation purely by stochastic and internal state switching. To detect the emergence of spatial inhomogeneities, we first calculate the spatial variance of the particle density. In a perfectly homogeneous state system, this variance would vanish. Therefore, any significant growth in variance serves as a signature for clustering,

$$\mathbb{V}\mathrm{ar}[\rho(x,t)] = \langle \rho(x,t)^2 \rangle - \langle \rho(x,t) \rangle^2, \tag{8.3}$$

Figure 8.6 shows the temporal evolution of this variance for different values of σ under $\beta = 2$, $\gamma = 0$ and $\sigma = 0.005$. For lower values of σ, the variance grows during the beginning transient state. However, for any value of σ the variance converges to zero in the long run. Variance growth for lower σ is easily interpreted as initial local fluctuations can cause local interactions and clustering formation, while for large σ only global interactions can occur which do not allows for local clustering effects. Importantly this simulation is done for $\beta \geq 1$, this results in convergence to one state with the state active movement direction. Therefore, it takes longer for local structure to dissipate. For $\beta \leq 1$, we see an immediately decrease in the variance as the particles will remain equally spread over different states which does not allow for local structure to stay. This is also seen in the previous results for the diffusion coefficient, that is Figure 8.4 shows a higher diffusion coefficient for $\beta \leq 1$. Additionally this simulation is done for $\gamma = 0$, for $\gamma > 0$ local structure will vanish faster and a lower σ is required for initial variance growth.

While the variance indicates the presence of inhomogeneities, it does not describe their length scale or coherence. To further quantify the spatial organization of these fluctuations, we analyze the space-time density heatmaps and Fourier spectrum of this simulation. Figures 8.7 and 8.8 show the single run results under $\sigma = 0.005$. In accordance to the variance plot 8.6, we see that the Fourier modes grow for $t \leq 5$, while they converge to 0 for $t \geq 5$. Indeed showing us that the variance converges to zero by Parseval's theorem. The space-time density heatmap in Figure 8.7 visualizes the coherent density bands that persist over intermediate time scales before dissolving

over a longer time scale. Figures 8.9 and 8.10 show the same system but run for $\sigma = 1$. As interactions are not local one indeed sees that the Fourier amplitudes immediately converge to zero and that in the space-time plot no local clustering is present. In summary, the models confirm convergence to the hydrodynamic predictions for global transport coefficient, while revealing how spatial fluctuations strongly depend on σ which is hard to predict analytically. The results provide a baseline against the interaction-driven effect that are studied in the next section.

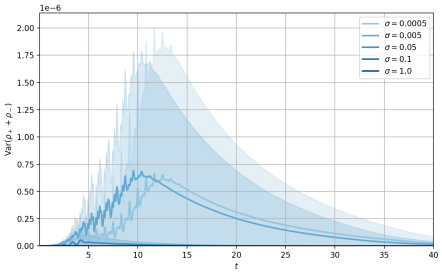

Figure 8.6: Time evolution of the variance for different values of σ under $\beta = 2$ and $\gamma = 0$ using the PDE model. Solid lines denote the average value of the variance while the shaded areas give the standard deviations. It is immediately clear that, for homogeneous initial conditions with noise, local structure can grow for small values of σ but will disappear in the long run.

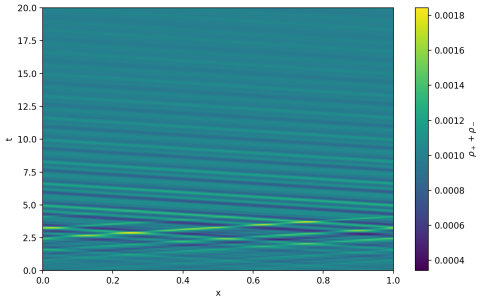

Figure 8.7: Space-time density plot of a single run simulation in the PDE model under $\beta = 2$, $\gamma = 0$ and $\sigma = 0.005$. The results show the spatial fluctuations and clustering increasing for $t \leq 5$ while slowly fading for $t \geq 5$.

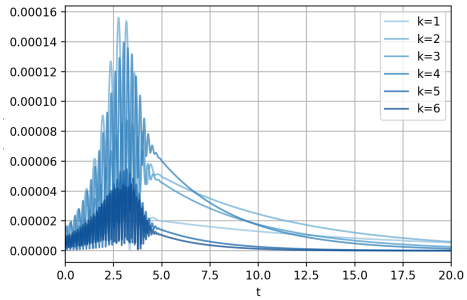

Figure 8.8: Time evolution of the first 6 Fourier amplitudes for a single run simulation in the PDE model under $\beta = 2$, $\gamma = 0$ and $\sigma = 0.005$. The results show growing amplitudes, however they converge to zero over a longer time. Thus local structure forms but fades away.

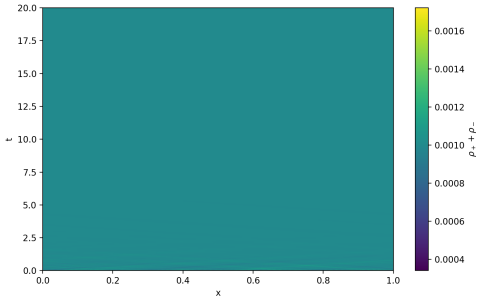

Figure 8.9: Space-time density plot of a single run simulation in the PDE model under $\beta = 2$, $\gamma = 0$ and $\sigma = 1$. The results show the initial spatial fluctuations immediately fade away and reach the homogeneous steady state.

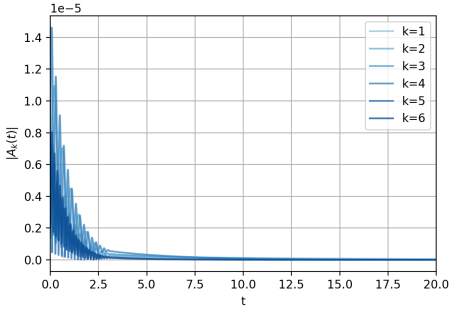

Figure 8.10: Time evolution of the first 6 Fourier amplitudes for a single run simulation in the PDE model under $\beta = 2$, $\gamma = 0$ and $\sigma = 1$. The results show amplitudes converging to zero.

8.2 Effects of exclusion and crowding

In the following two sections we adjust the model to be more biologically motivated. In contrast to Section 8.1 particles are no longer allowed to overlap as exclusion rules, defined in Section 5.3 and 7.3, are present. Moreover, the internal state space is restricted to inactive particles and right-moving active particles, rather than left-right movers. Additionally, Neumann boundary conditions are used instead of periodic BCs. This setting corresponds to the biologically relevant scenario introduced in Section 5 and 7. All simulations in this section can only be performed using the particle-based Gillespie algorithm. A direct comparison to the PDE derived in Section 3 is no longer possible, as interactions by exclusion are neglected. However, we try to make the comparison between the model and the PDE adjusted to the exclusion rules given in Section 6.2, and explain why this derivation does not hold for this biological model.

This section has two main goals. First, in Section 8.2, we quantify how exclusion modifies the global transport properties, i.e. effective velocity and diffusion, for different average densities and different values of beta and compare them to original PDE analyzed in Section 4.3 and the adjusted PDE analyzed in Section 6.2. Second, in Section 8.3, we demonstrate that exclusion rules fundamentally alter the formation of local structure.

8.2.1 Qualitative effects of exclusion for different σ

Before analyzing global transport coefficients, we first illustrate the qualitative impact of exclusion on the system dynamics. Visualizing the full space-time density field allows us to directly observe the formation of clusters and the coexistence of different magnetization domains, phenomena that are often averaged out in global statistics. Figure 8.11 and 8.12 show space-time density plots for a simulation with $\bar{\rho}/K = 0.75/3$ with homogeneous initial conditions with noise for respectively $\sigma = 0.02$ and $\sigma = 0.002$ under $\beta = 2$. Both plots show that exclusion leads to visible heterogeneous density profiles where for low σ regions of positive and negative magnetization can co-exist. Especially for lower values of σ, such as 0.002, many different magnetization regions form leading to more congestion and increasing spacial inhomogeneity. This occurs without the presence of additional outside forces or initial spatial inhomogeneity being present in the system. Note that this only occurs for $\beta > 1$ as particles then prefer to be in a similar internal state as particles close to them. Simulations for $\beta < 1$ show that such inactive regions are not present and are actually broken down.

These congestion effects are a direct consequence of the rejection of hopping effects into occupied sites. Active particles accumulate behind inactive particles, producing extended high-density regions. These active particles, for $\beta > 1$ will either switch to being inactive particle due to the high density of inactive particles stabilizing the inactive region or accumulate with many other active particles to outnumber the number of inactive particles and break down this inactive region. This is just a qualitative analysis, but the next section will focus on understand the effects of these phenomena on global transport coefficients and the formation of local structures.

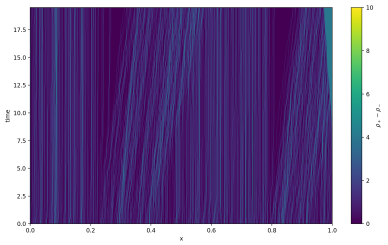

Figure 8.11: Space-time density plot of a single run simulation using the particle model under $\beta = 2$ and $\sigma = 0.02$. The results show different magnetization regions can co-exist and cause slight congestion.

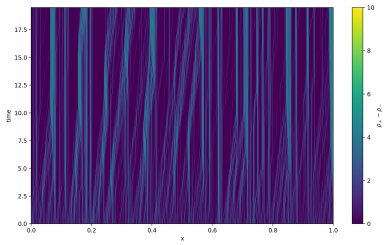

Figure 8.12: Space-time density plot of a single run simulation using the particle model under $\beta = 2$ and $\sigma = 0.002$. The results show many different magnetization regions can co-exist and cause heavy congestion.

8.2.2 Breakdown of the mean-field predictions for the effective velocity

In the absence of exclusion, the effective velocity is given by $v = \lambda \frac{1+m(\beta)}{2}$, with m determined by the solution of the mean-field equation. However, exclusion violates the assumptions made in the mean-field equation by introducing strong spatial correlations between the particles. After showing this breakdown we make an attempt to approximate the effective velocity under these exclusion rules for the global magnetization in the following section. Figure 8.13 show the effective velocity extracted from the particle simulations as a function of β under $\bar{\rho} = 0.5$, together with the corresponding mean-field predictions for both system without exclusion and the PDE adjusted to exclusion and the current system of inactive and active particles. For the latter the effective velocity is given by,

$$v_{eff} = \lambda \frac{1 + m(\beta)}{2}(1 - \bar{\rho}) \tag{8.4}$$

The prediction without exclusion is systematically wrong here as the particle movements are blocked decreasing the effective velocity. However, also the prediction from the model with exclusion seems to be wrong. Additionally, the effective velocity differs for different values of σ for $\beta > 1$. This was not the case in the model without exclusion. We will now discuss, why, first of all, the effective velocity differs for different values of σ, specifically for $\beta > 1$ and secondly why the prediction for the PDE with exclusion is wrong.

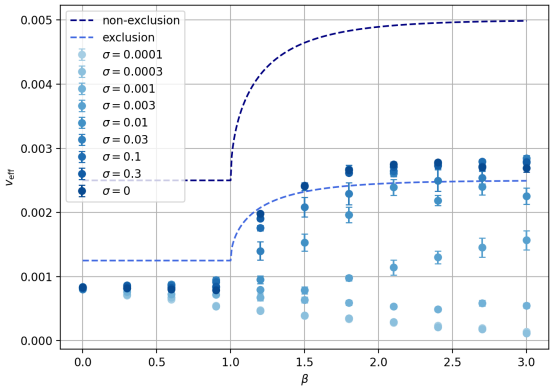

Figure 8.13: Effective velocity as a function of β for $\lambda = 0.005$ for different values of σ under $\bar{\rho} = 0.5$. Steady state predictions from both the PDE model with and without exclusion are also shown. Note that $\sigma = 0$, is the system under a global magnetization. The effective velocity does not follow the theoretical predictions even for a global magnetization and that, for $\beta > 1$, v_{eff} is σ-dependent and.

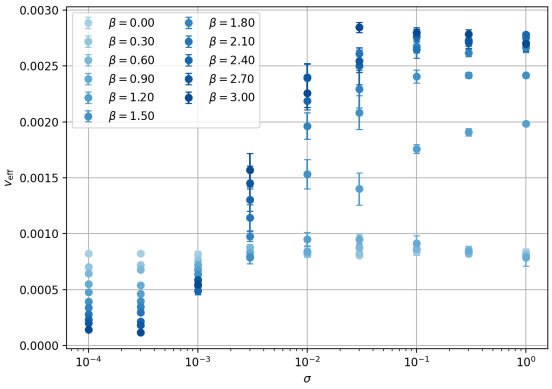

Figure 8.14: Effective velocity as a function of σ for $\lambda = 0.005$ for different values of β under $\bar{\rho} = 0.5$. One sees that for $\beta < 1$ the effective velocity is independent of σ. However, for $\beta > 1$ as σ increases the effective velocity also increases.

Different values of σ cause a different formation of inactive regions for $\beta > 1$, as can be seen in Figure 8.11 and 8.12, leading to different values of the effective velocity. More specifically, for $\beta < 1$, particles prefer to be in different states than the particles with which they interact. Therefore no inactive regions will form, consequently the system will have a similar structure for every value of σ and the effective velocity will thus not depend on σ. This can also be seen in Figure 8.14 that depicts the relation between the effective velocity and σ for different values of β. No dependence on σ is observed for $\beta < 1$, while for $\beta > 1$ the effective velocity increases with σ. This is explained by the fact that for smaller values of σ more inactive regions will form, as seen in Figure 8.11 and 8.12, therefore increasing the chance of an active particles to be blocked. This explains why we see a decrease in the effective velocity as σ decreases.

From Figure 8.15 and 8.14 it also follows that the results deviate from the theoretical derivation given in Section 6.2 even for the global magnetization. For the local magnetization is clear that formation of local structures and local micro-environments of a different magnetization as seen in Figure 8.11 and 8.12 can cause different effective velocities breaking the hydrodynamic assumptions and therefore the results. However, for the global magnetization the results also differ from the theory. We now aim to explain this difference and where the theoretical derivation failed.

The systematic difference between the simulation results and the PDE prediction in Section 6.2 (based on Kourbane-Houssene et al. [4]) arise from the breakdown of the mean-field assumptions. That is, Section 6.2 relies on an one-point closure approximation, where the evolution of the local density depends solely on the single-site expectations. that is let n the number of particles at a site, then

$$\langle n_i n_{i+1} \rangle \approx \langle n_i \rangle \langle n_{i+1} \rangle = \rho(x,t)^2 \tag{8.5}$$

this effectively factorizes higher-order terms, but assumes that the occupancy of site $i+1$ is independent of site i. However, intuitively and from the results of the simulations we see that this assumption does not hold. Mathematically the true hopping rate for a particle at site i is proportional to $\mathbb{P}(n_i = 1 \ \cap \ n_{i+1} = 0)$. Under the mean-field assumptions this is approximated as $\mathbb{P}(n_i = 1)\mathbb{P}(n_{i+1} = 0) = \rho(1-\rho)$. However, in the presence of active motion and exclusion, particles accumulate in queues or cluster increasing this blocking probability and results in a reduced effective velocity as can be seen in the low β regime in Figure 8.15. For high β, however, particles prefer to be in similar internal states reducing the blocking probability and thus increasing the effective velocity. In different words one can say that the derivation in Section 6.2 (and thus [4]) assumes scaling limits where the timescale of the cluster relaxation is sufficiently separated from the timescale of the active transport. However, in the simulation this is not case preventing the system from engaging in the "local equilibrium" required for the theoretical derivation. To combat this problem the next section focuses attempt of find a better function for the effective velocity by fitting over the results of the simulation.

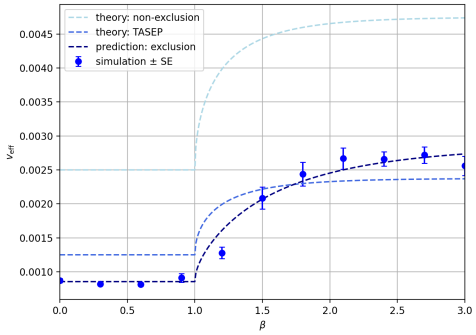

Figure 8.15: Effective velocity as a function of β for $\lambda = 0.005$ under $\bar{\rho} = 0.5$. Steady state predictions from both the PDE with and without exclusion are also given.

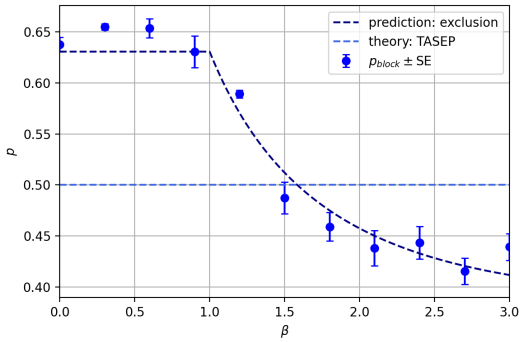

Figure 8.16: Blocking probability as a function of β for $\bar{\rho} = 0.5$. Both the blocking probability by the PDE model with exclusion (i.e. $\bar{\rho}$) and the prediction using Equation (8.7) are also given.

8.2.3 Prediction of the effective velocity under exclusion for the global magnetization

To exam the exact influence of crowding on the effective velocity we make an attempt to find an equation that predict the effective velocity for different β and different $\bar{\rho}$ under a global magnetization. In Section 5.3 we already argued that a potential function for effective velocity will be of the form,

$$v = \lambda \frac{1 + \tanh(\beta m)}{2} \left(1 - \Phi\left(\frac{\bar{\rho}}{k}, \beta\right)\right) \tag{8.6}$$

This section focuses on finding $\Phi\left(\frac{\bar{\rho}}{k}, \beta\right)$, which will, under $k = 1$, be $\Phi\left(\bar{\rho}, \beta\right)$. The goal here is to recover an analytical handle on the effective velocity, as the one-point closure failed and we can thus not use the effective velocity given by Equation 6.19. Since this analysis of the PDE under exclusion in Section 6.2 was unable to capture the right dependence, this attempt to find Φ will be a heuristic approximation. Figure 8.15 shows how the effective velocity depends on β under $\bar{\rho} = 0.5$. We see that it deviates from the prediction given by the TASEP model and also the PDE prediction from Section 6.2. To further understand this difference, we analyze the blocking probabilities given for different values of β in Figure 8.16. For $\beta < 1$ we have constant, but higher, blocking probability. This can be explained by the fact that particles attempt to be in different states as the particles with which they interact which results in a great mix of active and inactive particles resulting increased blocking. However for $\beta > 1$ we see a lower blocking probability than the one given by the PDE and TASEP prediction. Likely explained by the fact that interacting particles want to be in similar states resulting in less blocking. In practice, we see that we can approximate this behavior by the following function,

$$\Phi\left(\bar{\rho}, \beta\right) = \bar{\rho}\left(f\left(\bar{\rho}\right) + g\left(\bar{\rho}\right)\frac{1}{\cosh(\beta m)}\right) \tag{8.7}$$

as can be seen in Figure 8.16. The starting $\bar{\rho}$ is the same as the TASEP and PDE predictions however the f and g term are what differentiates it. Running the simulation for different values of $\bar{\rho}$ allows to find how f and g depend on $\bar{\rho}$ which can be see Figure 8.17. it is observed that f depends linearly on $\bar{\rho}$ and g for $\bar{\rho} > 0.2$ with $\bar{\rho}^{-3/2}$. More specifically,

$$f(\bar{\rho}) = C_0 - C_1\bar{\rho} \qquad \text{with} \quad C_0 = 1.25529..., \; C_1 = 0.60230... \tag{8.8}$$

$$g(\bar{\rho}) = C_2\bar{\rho}^{-3/2} \qquad \text{with} \quad C_2 = 0.15327... \tag{8.9}$$

As this prediction is not backed by any mathematics (yet) it is hard to put clear mathematical and biological conclusions on this results. However having this function that easily approximates the effective velocity under global magnetization and exclusion does allow us to easily match the model to experimental results for the effective velocity of Kinesin-II transport which will be done in Section 8.4.

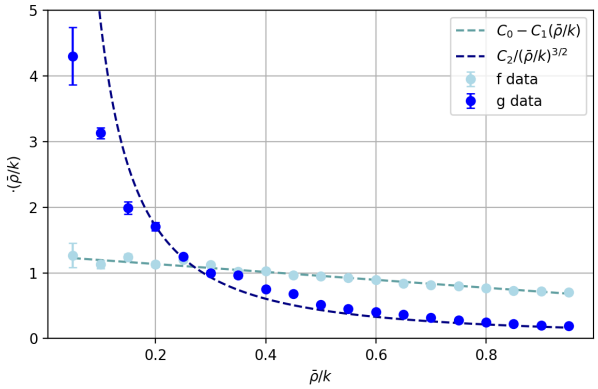

Figure 8.17: Fitted values f and g from Equation (8.7) optimized on the blocking probabilities of simulations under different values of $\bar{\rho}$. Note that this is only done for $k = 1$, which can therefore be neglected in the plot. Additionally potential fits for $f(\bar{\rho})$ and $g(\bar{\rho})$ are plotted in this figure.

8.2.4 Effective diffusion coefficient under exclusion

We next study how exclusion modifies the effective diffusion coefficient. Section 6.2 predicted that the diffusion coefficient was given by

$$\gamma + \frac{\lambda^2(1-\bar{\rho})(1-2\bar{\rho})}{2\cosh(\beta m)}\left(1+m^2\right) \tag{8.10}$$

under a global magnetization. Figure 8.18 shows the effective diffusion coefficient as a function of β for the mean density $\bar{\rho} = 0.5$ and several values of σ. For $\beta < 1$, where the steady state magnetization is zero and switching dominates over persistent motion, the diffusion coefficient is essentially independent of σ. For $\beta > 1$, where alignment and persistent motion becomes dominant, we see different behavior for different values of σ, with maximal values and largest uncertainties for intermediate values of σ, Small and large values of σ have smaller diffusion coefficient with lower uncertainties that stay closer to the values approximated by the PDE under a global magnetization. This PDE approximation systematically overestimates the true diffusion of large and small values of σ over the entire range of β, while being similar in shape. This indicates that the spatial correlations and exclusion rules reduce the effective diffusion coefficient beyond what is captured by a one-point closure. Something that was already explained in Section 8.2.2.

These results are reinforced by Figure 8.19 which displays the effective diffusion coefficient as a function of σ for several fixed values of β. Both in the strongly local and almost global regimes the diffusion coefficient approaches the theoretical curves, while for intermediate σ the system develops long-lived density inhomogeneities that increase fluctuations and slow down relaxation, leading to larger diffusion coefficients. These deviations signal the breakdown of the hydrodynamic limit and therefore we will study the formation of local structures and spatial correlation the following subsection.

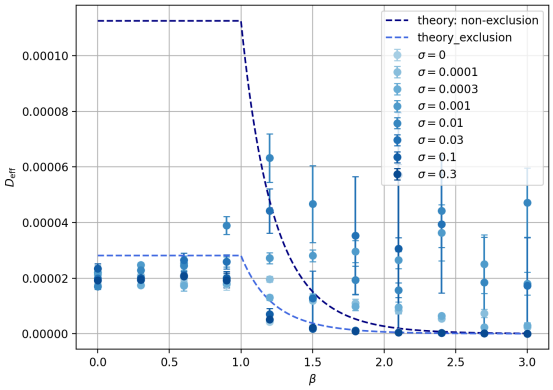

Figure 8.18: Effective diffusion coefficient as a function of β under $\bar{\rho} = 0.5$ for different values of σ. Additionally the PDE predictions for both non-exclusion and non-exclusion are also plotted. Note that $\sigma = 0$, shows the system under a global magnetization. For $\beta < 1$ the diffusion coefficient is σ-independent. For $\beta > 1$ the diffusion coefficient is larger with a larger standard deviation for intermediate σ. The PDE prediction under exclusion for the global magnetization slightly overshoots the actual values.

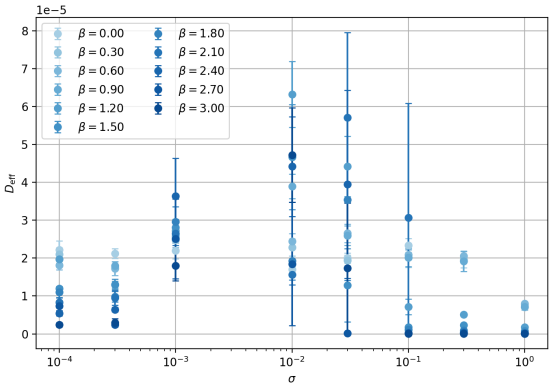

Figure 8.19: Effective diffusion coefficient as a function of σ for different values of β under $\bar{\rho} = 0.5$. This figure shows that for small and large values of σ the effective diffusion coefficient is small and is closer to the theoretical predictions while for intermediate values of σ one has a higher standard deviation and a larger diffusion coefficient.

8.3 Local structures and spatial fluctuations under exclusion

To go beyond global transport coefficient and assess how exclusion reshapes the system locally, that is we now analyze the emergence of spatial correlations and local structure. While the effective velocity and diffusion coefficient already reveal deviations from both the mean-field PDE without exclusion and with exclusion, these deviations originate from local effects such a queuing and jamming that cannot be diagnosed from one-point observables alone. We therefore study the full spatial-temporal density field and its spectral decomposition. We first consider the case of a local magnetization, where local interactions and exclusion leads to pronounced clustering persistent density bands and long-lived low-wavenumber modes. We then turn to the global magnetization, for which long-ranged and weak spatial inhomogeneities develop. These fluctuations are subtle, similar to the small differences observed between the global transport coefficient and their theoretically predicted values. As the formation of local structure is much harder to observe here, it is discussed last. This separation allows us to accurately, but qualitatively, pinpoint the differences observed between global transport coefficient and the ones predicted by the PDE model with exclusion (Equation 6.19) for both weak, global interaction simulations and strong, local interaction simulation.

Note that in this section we work under similar starting conditions as Section 8.2, the only difference is that we start from a homogeneous initial state with random noise. We do this because it makes it much easier to analyze the growth of the variance and study the Fourier amplitudes.

8.3.1 Local structures and spatial fluctuations under exclusion for a local magnetization

To quantify the spatial structure for the local magnetization (i.e. $\sigma = 0.005$) we start by analyzing the Fourier spectrum. Figure 8.20 and 8.21 show a heatmap of the amplitudes of the Fourier modes for different values of β for respectively $\bar{\rho} = 0.3$ and $\bar{\rho} = 0.9$ for the final time of the simulations. For both average densities we see that for high β we have low-wavenumber modes with a big amplitude, telling us that local structure forms for high values of β. For $\beta < 1$ we see that low-wavenumber modes have a smaller amplitude than the high-wavenumber modes. This is the case because particles prefer to be in different states as the particles with which they interact leading to no local clusters. This behavior is seen for $\beta > 1$ as particles prefer to be in similar states. Figure 8.20 and 8.21 tell us that for higher densities higher-wavenumber modes have a bigger amplitude. Due to exclusion particles cannot be at the same position, this results in less local structure and a spread of the clusters and therefore higher-wavenumber modes have a bigger amplitude.

Apart from the final time Fourier-modes, studying their time-evolution tells us something about how these modes grow over time. For this we study the low-wavenumber variance,

$$P_{<k_c}(t) = \sum_{|k|\leq k_c} |\hat{\rho}_k(t)|^2 \tag{8.11}$$

where k_c is the cut-off wavenumber, here set to 25. We introduce this cut-off to distinguish between meaningful macroscopic clusters and irrelevant microscopic noise. High wavenumbers correspond to fluctuations at the scale of single lattice site, whereas the low-wavenumber variance ($P_{<k_c}$) captures the formation of large-scale, coherent clusters relevant to biological transport. $k_c = 25$ marks a good line between this when looking at Figures as 8.20 and 8.21.

Figure 8.22 shows the evolution of the low-wavenumber variance over time for $\bar{\rho} = 0.5$. In contrast to the non-exclusion model the variance does not converge to zero but rather to a non-zero constant value. For small β the variance increases little from the starting variance. However, for high β the variance grows considerably. Something that is in line with what we saw in figure 8.20 and 8.21 and the reasoning given there. To better understand how the low-wavenumber variance depends on the average density we next study the final time low-wavenumber variance for different values of $\bar{\rho}$.

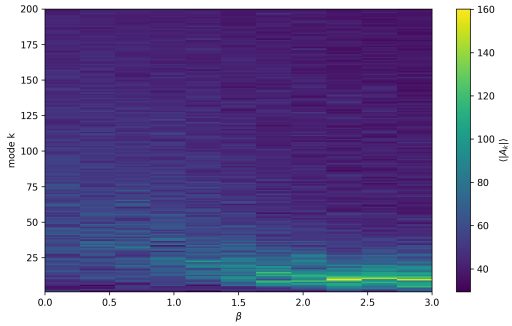

Figure 8.20: Heatmap showing the Fourier modes of the density field for different values of β for $\bar{\rho} = 0.3$. For high β formation of local structure is visible in the large amplitude of low-wavenumber modes.

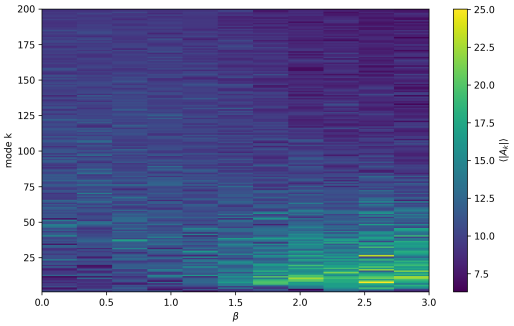

Figure 8.21: Heatmap showing the Fourier modes of the density field for different values of β for $\bar{\rho} = 0.9$. For high β formation of local structure is visible in the large amplitude of low-wavenumber modes, albeit less pronounced than in simulations for lower $\bar{\rho}$.

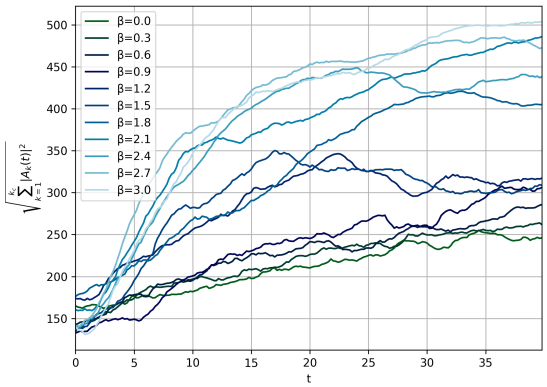

Figure 8.22: Average time evolution of the low-wavenumber variance $P_{k_c}(t)$ for $\bar{\rho} = 0.5$ and $\sigma = 0.005$, The non-zero values for every β show that exclusion prevents (fast) homogenization of the density field. For high β local structure increases seen by a growth in the low-wavenumber variance.

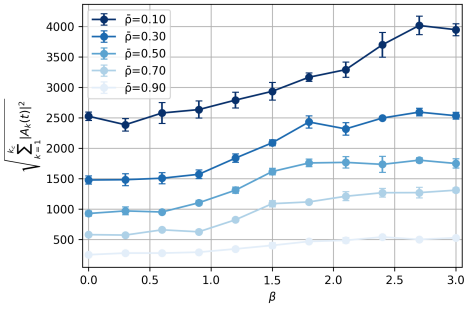

Figure 8.23: Final time low-wavenumber variance $P_{k_c}(t)$ as a function of β for several constant values of $\bar{\rho}$. Low average density leads to higher variance, showing that exclusion for high $\bar{\rho}$ prevents large spatial structure.

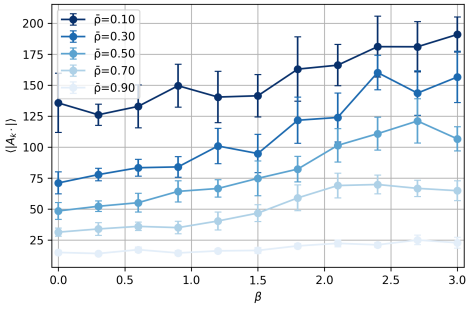

Figure 8.24: Final time maximum average Fourier amplitude $\langle |A_k| \rangle$ as a function of β for several constant values of $\bar{\rho}$. Low average density leads to higher maximum amplitudes. Additionally, higher β also leads to higher maximum amplitudes.

Figure 8.23 shows the final time low-wavenumber variance $P_{k_c}(t)$ as a function of β for several constant values of $\bar{\rho}$. From this figure it follows that for each value of $\bar{\rho}$ the variance increases starting from $\beta > 1$, Additionally, lower average densities results in higher variance as particles are less restricted by exclusion and clustering can therefore occur more easily. The same behavior can be seen when looking at Figure 8.24 which shows the maximum Fourier amplitude $\langle |A_k| \rangle$ as a function of β for several constant values of $\bar{\rho}$. Here we also see that the lower average densities lead to higher amplitudes of the biggest mode and thus more clustering and that higher β leads to higher maximum amplitudes. In conclusion, we see that under higher β and lower $\bar{\rho}$ the tendency of particles to form coherently moving densely packed clusters increases.

To further characterize the emerging patterns and even quantify it, we study the spectral entropy H and the mode-competition ratio R and their dependence on both β and $\bar{\rho}$. We start with the spectral entropy H. While the Fourier amplitude tells us the strength of the fluctuations, it does not quantify their complexity. The spectral entropy allows us to distinguish between a system dominated by a single coherent structure versus a system with disordered, multi-scale fragmentation. It is defined by,

$$H = -\sum_k p_k \log p_k, \qquad p_k = \frac{|\hat{\rho}_k|^2}{\sum_j |\hat{\rho}_j|^2} \tag{8.12}$$

The spectral entropy H measures the degree of collective order vs. disordered motion for respectively low and high values of H. This values can tell us if many different modes exist within the results of the simulation or if there is one coherent structure. Figure 8.25 shows the final time spectral entropy H as a function of β for several constant values of $\bar{\rho}$. This plot shows us that for intermediate values of $\bar{\rho}$ for $\beta > 1$ the spatial entropy decreases. That is, there is more coherent clustering. We have already seen this behavior in the heatplots of Figure 8.20 and 8.21 where for $\bar{\rho} = 0.3$ certain low modes dominate while for $\bar{\rho} = 0.9$ may modes have a higher amplitude not bringing the spatial entropy down compared to $\beta < 1$. A different measure is the mode-competition ratio R. which is defined by,

$$R = \frac{\max_k |\hat{\rho}_k|^2}{\sum_j |\hat{\rho}_j|^2} \tag{8.13}$$

To explicitly check for the emergence of a single dominant wavelength, such as a periodic traffic jam spacing, we calculate the mode competition ratio R. This ratio quantifies how strongly one mode dominates over other alternative modes. For large values of R one mode overwhelms all others, whereas for small values of R several modes have comparable strength. Figure 8.26 shows the final time mode-competition ratio R as a function of β for several constant values of $\bar{\rho}$. Similar to Figure 8.25 this shows us that for intermediate values of $\bar{\rho}$ for $\beta > 1$ low-wavenumber modes grow and dominate more over others.

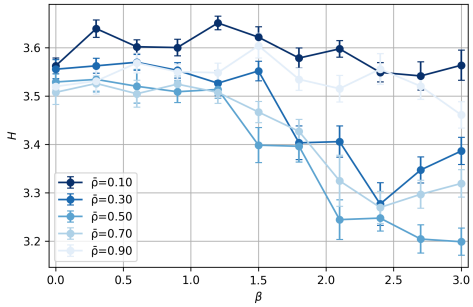

Figure 8.25: Final time spectral entropy H as a function of β for several constant values of $\bar{\rho}$. For intermediate values of $\bar{\rho}$ under high β we see that the energy is concentrated in a smaller number of modes, hinting at one coherent structure.

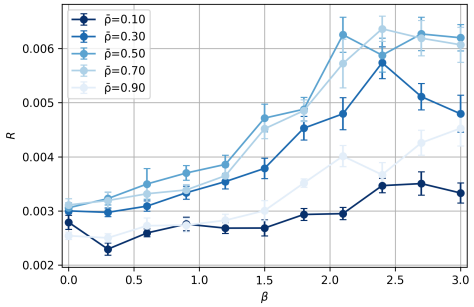

Figure 8.26: Final time mode-competition ratio R as a function of β for several constant values of $\bar{\rho}$. For higher values of β more dominant modes exist, especially for intermediate values of $\bar{\rho}$.

8.3.2 Local structures and spatial fluctuations under exclusion for the global magnetization

For a local magnetization the formation of local structure is quite expected. For the global magnetization however you do not immediately expect this, as was the case for the non-exclusion model discussed in Section 8.1. However, under exclusion weak and long-ranged spatial inhomogeneities do seem to arise occasionally. This section aims to show that indeed weak spatial inhomogeneities develop for a global magnetization, but fade away over a longer time.

Figure 8.27 shows amplitude of the Fourier-modes of the density field for different values of β for $\bar{\rho} = 0.5$. Similar to local magnetization simulations we see that for $\beta < 1$ no local structure forms as no low-wavenumber modes are dominant. For $\beta > 1$, however, we see lower modes with a bigger amplitude leading us to believe that local clustering does take place because of the additional (local) exclusion. Importantly, this is very case dependent as for example the final simulation, i.e. for $\beta = 3$, does not show this. The amplitudes of the lower modes are also significantly lower than what we saw in heatmaps such as 8.20 and 8.21 showing us the clustering is less robust.

This occasional clustering is observed in Figure 8.28 which shows the average time evolution of the low-wavenumber variance $P_{k_c}(t)$ for different values of β. While the $\beta < 1$ simulations grow similar to the model that uses the local magnetization, for $\beta > 1$ we see that certain simulations grow from their initial conditions while others stay constant. Note that for the same average density the variance of is significantly lower than the model that uses the local magnetization. In conclusion, the clustering is less and occurs only sporadically for $\beta > 1$. A deeper analysis exploring coefficient and results such a figures 8.23-8.26 requires different and harder techniques as this clustering is only sporadic and goes beyond the scope of this thesis.

In conclusion, all the figures and results show that for a local magnetization, and a less pronounced manner for the global magnetization, we see formation of persistent local structure. These structures confirm the breakdown of the factorization assumption $\langle n_i n_{i+1} \rangle \approx \rho^2$ made to derive v_{eff} and D_{eff} and thus shows us that the global transport coefficient following from the simulation will indeed differ from the ones derived in Section 6.2.

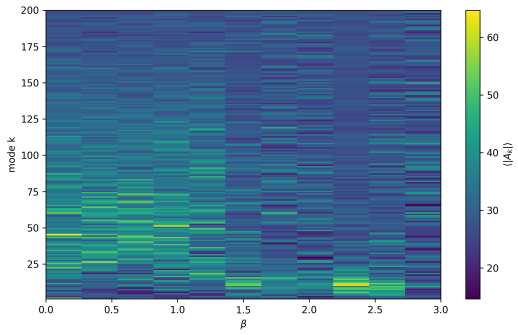

Figure 8.27: Heatmap showing the Fourier-modes of the density field for different values of β for $\bar{\rho} = 0.5$. Formation of local structure is less pronounced than under a local magnetization and very case dependent.

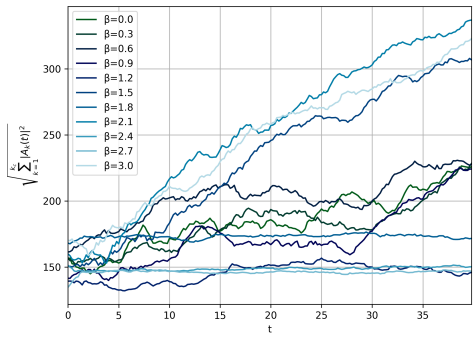

Figure 8.28: Average time evolution of the low-wavenumber variance $P_{k_c}(t)$ for $\bar{\rho} = 0.5$, The non-zero values for every β show that exclusion prevents (fast) homogenization of the density field. For certain β local structure increases slightly seen by a growth in the low-wavenumber variance. However, this is not strictly the case for every $\beta > 1$.

8.4 Kinesin-II transport: an application to experimental velocity-density data

In the previous sections, we established that our active particle model under exclusion exhibits distinct collective transport properties and were able to capture this in a formula in the case of the effective velocity under the global magnetization, given by Equation (6.19). In this final section, we validate the applicability of these theoretical results by fitting it to experimental data. We focus on the effective velocity of Kinesin-II motor proteins, for which its relation with the density has been experimentally found by Kushwaha et al. [10]. We demonstrate that our mean-field model with exclusion under a global magnetization provides a statistically more accurate description of the velocity-density relationship compared to the standard TASEP-LK model used in the original study.

Kinesin-II is, unlike Kinesin-I or OSM-3, remarkably resilient to crowding and responsible for intraflagellar transport (IFT). In their 2020 study, Kushwaha et al. measured the velocity of Kinesin-II at varying motor densities using total internal reflection fluorescence (TIRF) microscopy [10]. They observed that while velocity decreases as the density of the motors on the MT increases, this reduction is far less pronounced than in other motor proteins. To model this behavior, Kushwaha et al. employed the totally asymmetric simple exclusion process with Langmuir kinetics (TASEP-LK). This standard model assumes particles hop unidirectionally with hard-core exclusion and can attach/detach from the lattice. We use this as our benchmark because it represents the standard 'null hypothesis' for molecular motor transport: particles interact only through exclusion without communication. Deviations from this model, therefore, provide evidence for the cooperative mechanisms we propose. While this model captured the qualitative trend of the velocity reduction due to crowding, the fit showed noticeable deviations. The best fit obtained in [10] suggested a lattice of 13 protofilaments to account for the high speeds at these high densities. Additionally the TASEP-LK model requires two other parameters to be able to fit it to the experimental data.

We propose that the crowding dynamics of Kinesin-II can be better described by our mean-field global exclusion model. As Kinesin-II maintains a higher velocity in crowded environment it likely exhibits cooperative behavior which our model is able to capture, as can be seen by lower blocking probabilities and a higher effective velocity than the original TASEP prediction for high β in Figure 8.16 and 8.15. This would reduce the three parameters used in the TASEP-LK to just one parameter β. To fit the experimental data, we use the approximation for the effective velocity under global magnetization and exclusion derived in Section 8.2.3. That is, the effective velocity is approximated by

$$v = \lambda \frac{1 + \tanh(\beta m)}{2} \left(1 - \Phi\left(\bar{\rho}, \beta\right)\right)$$

where $\Phi\left(\bar{\rho}, \beta\right)$ represents the blocking probability function derived in Equation (8.7). We assume $k = 1$, consistent with the physical reality of the protofilament. We fit this function to the experimental data points extracted from Figure 4B of Kushwaha et al. [10] optimizing for the parameters λ and β. By fitting Equation (8.7) to the experimental data, we aim to demonstrate that the resilience of Kinesin-II to crowding is best explained not by geometric complexity, but by the internal cooperative switching captured by our β parameter. The results of the fitting procedure are presented in Figure 8.29. The figure compares the experimental Kinesin-II data with the best fit from the TASEP-LK model and our global magnetization mean-field exclusion model. The fitting yields the following parameters,

$$\beta = 23.708, \qquad \lambda = 0.289 \tag{8.14}$$

Visually, our model captures the profile of the velocity drop-off more accurately especially in the intermediate regime. The high value of $\beta \approx 23.708$ in our model suggests a strong cooperative alignment, allowing the effective velocity to remain stable closer to the saturation point before dropping. To quantify the improvement in goodness-of-fit, we calculate the Chi-squared statistic for both models, that is,

$$\chi^2_{TASEP-LK} = 38.129, \qquad \chi^2_{Mean-field} = 22.588 \tag{8.15}$$

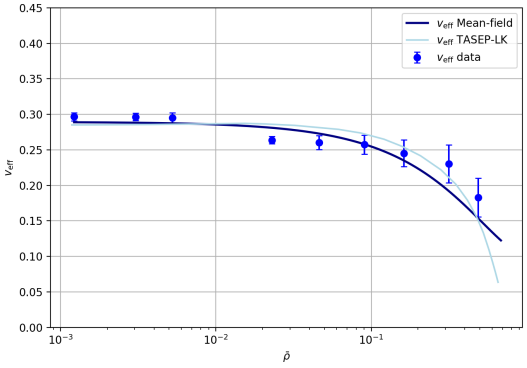

Figure 8.29: Velocity-density relation for Kinesin-II transport. Experimental data from [10] are compared with the best TASEP-LK fit from [10] and with our global magnetization mean-field exclusion model fitted to $k = 1, \beta = 23.708$ and $\lambda = 0.289$. The latter provides an improved description of the data, which can also be seen in Chi-squared statistic in Equation 8.15.

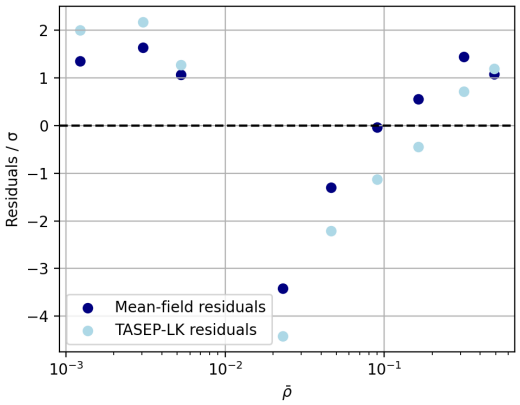

Figure 8.30: Residuals of the velocity-density fit for both TASEP-LK and mean-field model from Figure 8.29. It indicates that the mean-field model provides a better description of the data, which can also be seen in Chi-squared statistic in Equation 8.15.

The lower χ^2 for our mean-field model indicates a closer agreement with the experimental data. Furthermore, the residuals of the fit, shown in Figure 8.30, show that the mean-field model has lower residuals with less systematic structural difference from the data than the TASEP-LK model which required two more fit parameters.

While the fit supports the evidence for the utility of our model, several limitations must be noted. First, application of the global magnetization along a MT is a simplification. Biologically, interactions will likely be local, however, as seen in Figure 8.13, the effective velocity stays close to the effective velocity under global magnetization for $\sigma > 0.01$. Secondly, the fitting parameter β is high. This would indicate very strong cooperativity. While this aligns with the hypothesis that Kinesin-II is resilient to crowding, our analysis was limited to $\beta \leq 3$. This thus requires further investigation. Most importantly, to match the experimental results the TASEP-LK model required the assumption of 13-protofilament MTs. This allowed for the distribution of the particles and thereby a reduction of the effects of exclusion. Our model achieves a more accurate fit using only a single-channel approximation. This again aligns with the hypothesis of Kinesin-II but is a very different approach to the original TASEP model. Despite these simplifications and potential errors, the ability of our model to outperform the TASEP-LK model using a simpler geometry and only two free parameters reinforces the validity of the active particle mean-field approach in biological transport.

9 Conclusion

In this thesis, we have bridged the gap between mathematical analysis of a mean-field interacting particle system and the biological reality of intracellular transport via kinesin. By constructing a minimal active-diffusion model with internal state switching, we investigated how interactions, mediated by local or global mean-field forces, regulate global transport coefficient and crowding. Our work yields contributions to both the mathematical theory on such models, their hydrodynamic limits and transport coefficients and the physical modeling of Kinesin-II motor proteins.

From a mathematical perspective, we derived the hydrodynamic limit for an active mean-field interaction model under both global and local magnetization and thus proved that the microscopic dynamics converge to a the macroscopic PDE. A key result of the analysis of this PDE was the derivation of the exact analytical expression for the global transport coefficient, the effective velocity v_{eff} and the effective diffusion coefficient D_{eff} for the Curie-Weiss Glauber rates.

These derivations provide a new insight into active mean-field models. Specifically, we showed that under global interactions the effective diffusion coefficient is composed of a passive Brownian component and an active enhanced term that depends on the magnetization of the system. We further showed that under local interactions, the diffusion coefficient can diverge as the system approaches criticality, signaling to potential pattern formation and clustering. These theoretical results provide a framework for understanding how microscopic switching rules translate to macroscopic transport phenomena.

On the physical side, we developed an accurate particle-based model for Kinesin-II movement along a microtubule that incorporates exclusion and interactions over different lenghts. Our simulations showed complex behavior that extended beyond the standard mean-field predictions.

First, we observed that the global transport coefficients under exclusion deviates from the predictions derived from out PDE model and our PDE model adjusted to exclusion. However, these differences are intuitively explainable: to derive the PDE and preform the analysis higher-order terms are factorized, neglecting the formation of local queues and jams that obstruct transport. We found that for $\beta > 1$, where particles align cooperative, the blocking probability is reduced compared to standard TASEP predictions for high interaction ranges, while being increased for very small interaction ranges. The results for the global interactions are a first explanation for the resilience of Kinesin-II to crowding.

Second, we found that for the interaction range σ, small σ exhibits larger relaxation times. In this regime, distinct regions of opposing magnetization can coexist longer, leading to congestion and spatial heterogeneity that is absent in the global case. While we could accurately predict the exact values for v_{eff} and D_{eff} for local interaction ranges, the simulations confirm that local interactions fundamentally alter transport by allowing the formation of local structures.

Finally, we validated our model against experimental data for Kinesin-II transport. Our mean-field exclusion model provided a statistically more accurate description of the velocity-density relation compared to the previously used TASEP-LK model. By capturing the cooperative nature of motor transport, our model achieved a better fit to experimental data using a simpler single-lane geometry, demonstrating that internal state switching could be an important mechanism to explain the efficient transport in crowded biological environments.

While this thesis creates a solid foundation, several areas of future research remain. The current analytical derivation for the effective velocity under exclusion relies on a semi-empirical fitting function $\Phi(\bar{\rho}, \beta)$. A rigorous mathematical derivation of this function would be a valuable next step. Furthermore, our fitting yielded a high cooperative parameter β, suggesting very strong alignment forces. Future studies could investigate, whether this reflects true biological cooperativity or is an effective parameter compensating for other geometrical simplifications.

References

[1] Thomas M. Liggett. *Interacting Particle Systems*. Springer, 1985.

[2] Frank Redig. Basic techniques in interacting particle systems. Lecture notes, TU Delft, 2014.

[3] Clément Erignoux. On the hydrodynamics of active matter models on a lattice. *Mémoires de la Société Mathématique de France*, 2021. URL https://arxiv.org/abs/2108.04003.

[4] Mourtaza Kourbane-Houssene, Clément Erignoux, Thierry Bodineau, and Julien Tailleur. Exact hydrodynamic description of active lattice gases. *Physical Review E*, 97(1), 2018. doi: 10.1103/PhysRevE.97.012607. URL https://arxiv.org/abs/1801.08952.

[5] Nobutaka Hirokawa, Yasuko Noda, Yosuke Tanaka, and Shinsuke Niwa. Kinesin superfamily motor proteins and intracellular transport. *Nature Reviews Molecular Cell Biology*, 10(10), 2009. doi: 10.1038/nrm2774. URL https://doi.org/10.1038/nrm2774.

[6] Daniel St Johnston. Moving messages: the intracellular localization of mRNAs. *Nature Reviews Molecular Cell Biology*, 6(5), 2005. doi: 10.1038/nrm1643. URL https://doi.org/10.1038/nrm1643.

[7] Bernard Derrida. An exactly soluble non-equilibrium system: The asymmetric simple exclusion process. *Physics Reports*, 301(1-3), 1998. doi: 10.1016/S0370-1573(98)00006-4. URL https://doi.org/10.1016/S0370-1573(98)00006-4.

[8] Cécile Leduc et al. Molecular crowding creates traffic jams of kinesin motors on microtubules. *Proceedings of the National Academy of Sciences*, 109(16), 2012. doi: 10.1073/pnas.1107281109. URL https://doi.org/10.1073/pnas.1107281109.

[9] Aafke A. van den Berg. *The interplay between polymerase organization and nucleosome occupancy along DNA*. PhD thesis, Delft University of Technology, 2017. URL https://doi.org/10.4233/uuid:993e98ca-3c91-4591-9fbf-26bd6eea2354.

[10] Vandana S. Kushwaha, Seyda Acar, Daniël M. Miedema, Dmitry V. Denisov, Peter Schall, and Erwin J. G. Peterman. The crowding dynamics of the motor protein kinesin-ii. *PLOS ONE*, 15(2), 2020. doi: 10.1371/journal.pone.0228930. URL https://doi.org/10.1371/journal.pone.0228930.

[11] Sacha Friedli and Yvan Velenik. *Statistical Mechanics of Lattice Systems: A Concrete Mathematical Introduction*. Cambridge University Press, 2017. URL https://www.unige.ch/math/folks/velenik/smbook/.

[12] Robbert Fokkink. Notes on WI4430 martingales and Brownian motion. Lecture notes, TU Delft, 2016.

[13] Amir Dembo and Ofer Zeitouni. *Large Deviations Techniques and Applications*. Springer, 2010.

[14] Paul Griffiths and Dominic Welsh. *Probability: An Introduction*. Oxford University Press, 2nd edition, 2019.

[15] Cor Kraaikamp. PROBSTAT-IIii. Lecture Notes, TU Delft, 2011.

[16] Hidde van Wiechen. Ergodic theory and hydrodynamic limit for run-and-tumble particle processes. Master's thesis, Delft University of Technology, 2021. URL https://repository.tudelft.nl/.

[17] Marthe Meskers. Active particles in one dimension: Asymptotic behaviour and collective dynamics, 2021.

[18] Frank den Hollander. *Large Deviations*. American Mathematical Society, 2000.

[19] Fraydoun Rezakhanlou. Lectures on the large deviation principle, 2017.

[20] Hugo Touchette. A basic introduction to large deviations: Theory, applications, simulations, 2024. URL https://arxiv.org/abs/1106.4146.

[21] Frank Redig and Hidde van Wiechen. Equilibrium fluctuations of run-and-tumble particles, 2024. URL https://arxiv.org/abs/2307.02967.

[22] Claude Kipnis and Claudio Landim. *Scaling Limits of Interacting Particle Systems*. Springer-Verlag, 1999.

[23] Katherine Luby-Phelps. Cytoarchitecture and physical properties of cytoplasm: volume, viscosity, diffusion, intracellular surface area. *International Review of Cytology*, 192, 2000. doi: 10.1016/S0074-7696(08)60527-6. URL https://doi.org/10.1016/S0074-7696(08)60527-6.

[24] R. John Ellis. Macromolecular crowding: obvious but underappreciated. *Trends in Biochemical Sciences*, 26(10), 2001. doi: 10.1016/S0968-0004(01)01938-7. URL https://doi.org/10.1016/S0968-0004(01)01938-7.

[25] Jonathon Howard. *Mechanics of Motor Proteins and the Cytoskeleton*. Sinauer Associates, 2001.

[26] StandeHaas. Hydrodynamic-Limits-of-Active-Particle-Systems-with-Mean-Field-Interactions. https://github.com/StandeHaas/Hydrodynamic-Limits-of-Active-Particle-Systems-with-Mean-Field-Interactions, 2026.